UNIVERSITY OF CALIFORNIA
SANTA CRUZ

SIGNATURE OF NON-STANDARD COSMOLOGIES: FROM DARK MATTER TO PRIMORDIAL BLACK HOLES

A dissertation submitted in partial satisfaction of the
requirements for the degree of

DOCTOR OF PHILOSOPHY

in

PHYSICS

by

Nicolas Fernandez Gonzalez

June 2019

The Dissertation of Nicolas Fernandez Gonzalez
is approved:

Stefano Profumo, Chair

Michael Dine

Anthony Aguirre

Lori Kletzer
Vice Provost and Dean of Graduate Studies

Table of Contents

List of Figures

List of Tables

Abstract

Signature of non-standard cosmologies: from dark matter to primordial black holes

by

Nicolas Fernandez Gonzalez

If the dark matter is produced in the early universe prior to Big Bang nucleosynthesis, a modified cosmological history can drastically affect the abundance of relic dark matter particles. Here, we assume that an additional species to radiation dominates at early times, whose energy density red-shifts faster than radiation like $\rho_\phi \propto a^{-(4+n)}$, causing the expansion rate at a given temperature to be larger than in the standard radiation-dominated case. We consider the cases of dark matter production via freeze-out and freeze-in in theses non-standard cosmologies.

For the first case, dark matter freeze-out occurs at higher temperatures compared to the standard case, implying that reproducing the observed abundance requires significantly larger annihilation rates. Here, we point out a completely new phenomenon, which we refer to as relentless dark matter: for large enough n, unlike the standard case where annihilation ends shortly after the departure from thermal equilibrium, dark matter particles keep annihilating long after leaving chemical equilibrium, with a significant depletion of the final relic abundance. For the case of dark matter production via freeze-in (a scenario when dark matter interacts very weakly, and is dumped in the early universe out of equilibrium by decay or scattering processes involving particles in the thermal bath) the abundance is dramatically suppressed. We quantitatively and analytically study this phenomenon for three different paradigmatic classes of freeze-in scenarios. For the frozen-in dark matter abundance to be as large as observations, couplings

between the dark matter and visible sector particles must be enhanced by several orders of magnitude. This sheds some optimistic prospects for the otherwise dire experimental and observational outlook of detecting dark matter produced by freeze-in.

Finally, the recent discovery of gravitational waves from binary black hole mergers has given us a new way to study our universe, but the origin of the black holes binaries remains unclear. We investigate how to use information on the effective spin parameter of binary black hole mergers from the LIGO-Virgo gravitational wave detections to discriminate the origin of the merging black holes. We calculate the expected probability distribution function for the effective spin parameter for primordial black holes. Using LIGO-Virgo observations, we then calculate odds ratios for different models for the distribution of black holes' spin magnitude and alignment. We evaluate the posterior probability density for a possible mixture of astrophysical and primordial black holes as emerging from current data, and calculate the number of future merger events needed to discriminate different spin and alignment models at a given level of statistical significance.

To My Family

Acknowledgments

First and most importantly, I would like to thank my advisor Stefano Profumo for his guidance and constant support over my graduate career despite my (sometimes) crazy ideas. I am thankful to Michael Dine for his motivation, enthusiasm, and immense knowledge. And I am indebted to Anthony Aguirre for his crucial remarks about cosmology.

I am profoundly grateful with all the postdocs that I encountered during my academic career, I cannot begin to express my thanks for their honest advice and kind encouragement: Akshay Ghalsasi, Bibhushan Shakya, Hiren Patel, Djuna Croon and Graham White.

I have been fortunate throughout the years of sharing the friendship of amazing graduate students: Adam Coogan, Di Xu, Douglas Tuckler, Brian Maddock , John Tamanas, Benjamin Lehmann, Laurel Haskin-Stephenson, Ross Greenwood, Amita Kuttner, Joseph Schindler, Cesar Rojas, Bruno Villasenor.

Most of all, I want to thank my parents, Oscar Fernandez and Adriana Gonzalez, and my sister, Laura Fernandez for their unconditional love and support. Also my beloved abuelita who is not here with us today but that believed more in me than myself. And last but not least, with the utmost enthusiasm, I want to thank my partner Maho Morimoto for all her love and support. She has always encouraged me throughout all my days in graduate school.

The text of this dissertation includes reprints of the following previously published material: *"When the Universe Expands Too Fast: Relentless Dark Matter"*. F. D'Eramo, N. Fernandez, S. Profumo, JCAP **1705** (2017) 012, arXiv:1703.04793 [hep-ph]; *"Dark Matter Freeze-in Production in Fast-Expanding Universes"*. F. D'Eramo, N. Fernandez, S. Profumo, JCAP **1802** (2018) 046, arXiv:1712.07453 [hep-ph]; *"Unraveling the origin of Black Holes from effective spin measurements with LIGO-Virgo"*. N. Fernandez, S. Profumo, arXiv:11905.13019 [astro-ph].

Chapter 1

Introduction

We are at an exciting juncture in physics where we have consensus models for both particle physics, the Standard Model (SM), and cosmology. However, despite success, several puzzles remain. Notable among these is the question of what the particle physics description of dark matter (DM) and its cosmological origin. The evidence for DM is a very robust expanding over several order of magnitude in the universe, from dwarf galaxies to the cosmic microwave background (CMB). furthermore, each particle candidate has to satisfy the relic density constraint, namely the computed relic density has to match the one inferred from astronomical and cosmological observations.

Thermal freeze-out is an attractive mechanism for DM genesis [8, 9, 10, 11]. Within this paradigm, DM particles are in thermal equilibrium at high temperatures; as the plasma temperature eventually drops below the DM mass, the Hubble expansion rate becomes larger than the rate for processes that keep the DM species in thermal equilibrium; DM particles thus *freeze-out*, with an approximately fixed comoving number density. Remarkably, such a relic density depends only on masses and couplings that can be, in principle, independently measured in a laboratory, and it therefore does not depend on the uncertain cosmological

history of the universe. The jargon used to express this fact is to say that DM freeze-out is "*IR-dominated*".

The above statement has, however, a well-known caveat: it is true only for a standard thermal history (i.e. an energy density dominated by radiation at early times, $T \gg 1\,\mathrm{MeV}$) all the way up to the freeze-out temperature, approximately a factor of 20 below the DM mass. Although this has to be the case at temperatures below Big Bang Nucleosynthesis (BBN), $T_{\mathrm{BBN}} \simeq$ few MeV [12, 13], we have no direct information for the expansion rate and energy density make-up of the universe at higher temperatures.

In chapter 2, we consider a modification to the standard cosmological history consisting of introducing a new species ϕ whose energy density red-shifts with the scale factor a like $\rho_\phi \propto a^{-(4+n)}$. For $n > 0$, such a red-shift is faster than radiation, hence the new species dominates the energy budget of the universe at early times while it is completely negligible at late times. If equality with the radiation energy density is achieved at low enough temperatures, dark matter can be produced as a thermal relic during the new cosmological phase. Dark matter freeze-out then occurs at higher temperatures compared to the standard case, implying that reproducing the observed abundance requires significantly larger annihilation rates. Here, we point out a completely new phenomenon, which we refer to as *relentless* dark matter: for large enough n, unlike the standard case where annihilation ends shortly after the departure from thermal equilibrium, dark matter particles keep annihilating long after leaving chemical equilibrium, with a significant depletion of the final relic abundance. Relentless annihilation occurs for $n \geq 2$ and $n \geq 4$ for s-wave and p-wave annihilation, respectively, and it thus occurs in well motivated scenarios such as a quintessence with a kination phase. We discuss a few microscopic realizations for the new cosmological component and

highlight the phenomenological consequences of our calculations for dark matter searches.

Furthermore in chapter 3, we demonstrate that, if this is the case, dark matter production via freeze-in (a scenario when dark matter interacts very weakly, and is dumped in the early universe out of equilibrium by decay or scattering processes involving particles in the thermal bath) is dramatically suppressed. We illustrate and quantitatively and analytically study this phenomenon for three different paradigmatic classes of freeze-in scenarios. For the frozen-in dark matter abundance to be as large as observations, couplings between the dark matter and visible-sector particles must be enhanced by several orders of magnitude. This sheds some optimistic prospects for the otherwise dire experimental and observational outlook of detecting dark matter produced by freeze-in.

Finally, the recent discovery of gravitational waves from ten binary black hole mergers has given us a new way to study our universe. The origin of the black hole binaries remains unclear. In chapter 4, we investigate how to use information on the effective spin parameter of binary black hole mergers from the LIGO-Virgo gravitational wave detections to discriminate the origin of the merging black holes. We calculate the expected probability distribution function for the effective spin parameter for primordial black holes. Using LIGO-Virgo observations, we then calculate odds ratios for different models for the distribution of black holes' spin magnitude and alignment. We evaluate the posterior probability density for a possible mixture of astrophysical and primordial black holes as emerging from current data, and calculate the number of future merger events needed to discriminate different spin and alignment models at a given level of statistical significance.

Chapter 2

Freeze-out in Modified Cosmologies

2.1 Introduction

Decades after the first observational evidences, the origin and composition of the DM is still among the most urgent open questions in particle physics [5, 6, 7]. Weakly Interacting Massive Particles (WIMPs) are motivated particle candidates for DM, with a thermal relic abundance naturally close to the observed cosmological abundance of DM. A standard calculation [8, 9, 10] shows that this thermal relic WIMP abundance scales as the inverse annihilation cross section, and is mildly dependent on the particle mass. The observed DM abundance is reproduced for

$$\langle \sigma_{\rm th} v_{\rm rel} \rangle \simeq 3 \times 10^{-26}\,{\rm cm}^3\,{\rm sec}^{-1}\ , \tag{2.1}$$

where the brackets denote a thermal average and $v_{\rm rel}$ is the Møller velocity (for details see Ref. [11]). The cross section needed for a thermal relic is thus that typical of weak interactions. This phenomenal coincidence, combined with the

expectation of new degrees of freedom at the weak scale for independent reasons such as the hierarchy problem, is referred to as the "WIMP miracle".

The numerical value in Eq. (2.1) has been an important benchmark for WIMP searches. It is worth keeping in mind that it relies on a crucial assumption: at the time of DM genesis, the energy budget of the universe was dominated by its radiation content. We know from Big Bang Nucleosynthesis (BBN) that this is definitely the case at temperatures around and below $T_{\rm BBN} \simeq$ few MeV [12, 13]. However, we have no direct information about the energy budget of the universe at higher temperatures. The WIMP DM thermal relic abundance may differ by orders of magnitude if deviations from a standard cosmological history are considered [14, 15, 16, 17, 18, 19, 20, 21, 22, 23, 24, 25, 26].

In this chapter we consider DM genesis for a broad class of alternative cosmological histories. We assume the presence of another species ϕ, whose energy density red-shifts with the scale factor a as follows

$$\rho_\phi \propto a^{-(4+n)} \ , \qquad\qquad n > 0 \ . \tag{2.2}$$

The standard case of radiation follows the behavior above for $n = 0$. Here, we always consider $n > 0$, which implies that the ϕ energy density dominates over radiation at early enough times. The equality between the energy density of ϕ and radiation must happen at a temperature $T_r \gtrsim T_{\rm BBN}$ (we will be more quantitative about this point in Sec. 2.3). If such an equality is achieved after the time of DM production, the standard relic calculation is significantly affected, as is the thermal relic abundance of the DM. We survey the options for DM genesis when the universe is dominated by a fluid red-shifting as in Eq. (2.2) in Sec. 2.4.

The two-dimensional parameter space (T_r, n) fully describes the possible cosmological backgrounds in our setup. The two parameters cannot be arbitrary,

since for low enough T_r we must ensure not to spoil the success of BBN. This set of cosmological backgrounds are described in Sec. 2.2, where we provide an expression for the Hubble parameter as a function of the radiation bath temperature T. For each temperature value $T > T_r$, the Hubble parameter is always larger than what it would be for a standard cosmological history. For this reason, the universe expands *faster* than in the standard case when dominated by ϕ.

A significant energy density of ϕ around the time of BBN mimics the role of additional neutrino species. Light element abundances put bounds on N_ν [27], which can be used to exclude part of the (T_r, n) plane. We discuss these bounds in Sec. 2.3. Interestingly, the energy density of ϕ is completely subdominant at the time of the decoupling of the Cosmic Microwave Background (CMB). The number of effective neutrinos at $T_{\rm CMB} \simeq 1\,\text{eV}$ is also constrained [28], but our framework does not predict any deviation from the SM value.

This work focuses on freeze-out DM production. We assume the DM particles to achieve thermal equilibrium with the primordial plasma at high temperature, and decouple once the temperature drops below its mass. The faster expansion rate raises however an important question: does the DM *ever*= thermalize? This is inspected in App. A.1, where we quantify the conditions we need in order to have the DM in thermal equilibrium at early times. The answer to this question sets the stage for the DM relic density calculations in Sec. 2.4. These calculations are performed by parameterizing the new cosmological phase by (n, T_r), without specifying the microscopic origin of the new species ϕ. At large enough n, we find a very peculiar behavior for the DM number density evolution, that had never been recognized before: The different Hubble scaling with the temperature allows significant DM annihilations long after the decoupling from the thermal bath. For a DM annihilating through an s-(p-)wave process, this happens for

$n \geq 2(4)$. Remarkably, the red-shift with $n = 2$ arises from motivated theories of quintessence attempting to explain the current acceleration of our universe [29, 30]. We call relic particles freezing-out during this phase *relentless* dark matter, due to their obstinate struggle to get back to thermal equilibrium. This behavior, which we find in our numerical results shown in Figs. 2.1 and 2.2, is easily understood with the semi-analytical results given in App. A.3. Notably, the phenomenon of relentless dark matter leads to *significant numerical differences* in the calculation of the thermal relic density for example in the case of kination-domination phases from previous studies (see e.g. [31, 32]).

The faster expansion rate implies an earlier freeze-out. Since we are dealing with cold relic, reproducing the observed DM density requires couplings significantly larger than in the standard case. This opens up the possibility of having cross section substantially larger than the thermal value in Eq. (2.1), in contrast with the case of an early matter-dominated epoch providing dilution where smaller values of the cross section are required [14, 15, 16, 17], and consequently weaker signals in DM searches. We quantify how much annihilation cross sections can be enhanced in Figs. 2.3 and 2.4.

Finally, we address the question of the origin of the new cosmological component ϕ in Sec. 2.5, where we provide one explicit example of a microscopic theory leading to the behavior in Eq. (2.2). We summarize our results in Sec. 2.6, where we also discuss future work addressing the implications of our analysis for dark matter searches.

2.2 A faster expansion

The expansion rate of the universe, quantified by the Hubble parameter H, is controlled by its energy density through Friedmann's equations. We consider

cosmological histories where two different species populate the early universe, radiation and ϕ, with a total energy density $\rho = \rho_{\rm rad} + \rho_\phi$.

The contribution from radiation, the only one present for a standard cosmological history, can be expressed in terms of its temperature as follows

$$\rho_{\rm rad}(T) = \frac{\pi^2}{30} g_*(T) T^4 \ , \tag{2.3}$$

where $g_*(T)$ is the number of effective relativistic degrees of freedom. We find it useful to express ρ_ϕ as a function of the radiation temperature T. All we know is its red-shift behavior given in Eq. (2.2), hence we need to connect a with T. This is achieved by assuming and imposing entropy conservation in a comoving volume $S = sa^3 = \text{const}$, where the entropy density reads

$$s(T) = \frac{2\pi^2}{45} g_{*s}(T) T^3 \ . \tag{2.4}$$

Here, g_{*s} is the effective relativistic degrees of freedom contributing to the entropy density. Entropy conservation ensures $g_{*s}(T)^{1/3} T a = \text{const}$, and the scaling in Eq. (2.2) can be re-expressed as follows

$$\rho_\phi(T) = \rho_\phi(T_r) \left(\frac{g_{*s}(T)}{g_{*s}(T_r)} \right)^{(4+n)/3} \left(\frac{T}{T_r} \right)^{(4+n)} \ . \tag{2.5}$$

Here, T_r is some reference temperature set by the boundary conditions. We choose T_r as the temperature where the two fluids have equal energy densities. The full energy density at any temperature reads

$$\begin{aligned} &\rho(T) = \rho_{\rm rad}(T) + \rho_\phi(T) = \\ &\rho_{\rm rad}(T) \left[1 + \frac{g_*(T_r)}{g_*(T)} \left(\frac{g_{*s}(T)}{g_{*s}(T_r)} \right)^{(4+n)/3} \left(\frac{T}{T_r} \right)^n \right] \ , \end{aligned} \tag{2.6}$$

where we find it convenient to factor out the energy density of the radiation bath as given in Eq. (2.3). From this expression it is manifest that the energy budget of the universe is dominated by ϕ for temperatures $T \gtrsim T_r$.

With Eq. (2.6) in hand, we can evaluate the Hubble parameter as a function of the temperature

$$H = \frac{\sqrt{\rho}}{\sqrt{3}\, M_{\rm Pl}} \ , \tag{2.7}$$

where the reduced Planck mass is $M_{\rm Pl} = (8\pi G)^{-1/2} = 2.4 \times 10^{18}\,\text{GeV}$. At temperatures larger than T_r, and setting for simplicity $g_*(T) = \overline{g}_* = \text{const}$, the Hubble rate approximately is

$$H(T) \simeq \frac{\pi\, \overline{g}_*^{1/2}}{3\sqrt{10}} \frac{T^2}{M_{\rm Pl}} \left(\frac{T}{T_r}\right)^{n/2} \ , \qquad (T \gg T_r) \ , \tag{2.8}$$

The full standard model (SM) degrees of freedom would lead $\overline{g}_* = g_{*\rm SM} = 106.75$. The expression in Eq. (2.8) is the Hubble rate at the time of DM genesis for the cosmological histories considered in this work. This result manifestly shows how the expansion rate at a given temperature T is always larger than the correspondent value for a standard cosmological history. In our numerical analysis we use the complete expression for H, including the full temperature dependence of $g_*(T)$.

2.3 BBN Constraints

The successful predictions of light element abundances give us a quantitative test of the energy content of the universe when it was few seconds old. Before we consider freeze-out in the cosmological background described in Sec. 2.2, we have to ensure that we do not spoil this remarkable agreement between theoretical predictions and observations.

A potential issue with BBN arises if T_r is not too far away from the MeV scale, where light elements begin to form. If this is the case, the universe expands faster than the usual case around the BBN time, and the theoretical prediction for BBN abundances may be altered.

We parameterize the effect of the field ϕ by an effective number of relativistic degrees of freedom

$$\rho(T) = \frac{\pi^2}{30} g_*^{\rm eff}(T) T^4 \ , \tag{2.9}$$

where we define

$$g_*^{\rm eff}(T) = g_*(T) + \Delta g_*^{\phi}(T) \ . \tag{2.10}$$

Here, $g_*(T)$ is the standard contribution from radiation, whereas $\Delta g_*^{\phi}(T)$ accounts for the energy density of ϕ. The expression for the total energy density in Eq. (2.6) define unambiguously the latter. A historical and widely used way to parameterize this effect is to describe the presence of ϕ as the the number of effective neutrinos. Within this convention, the total number of relativistic degrees of freedom appearing in Eq. (2.9) reads

$$g_*^{\rm eff}(T) = 2 + \frac{7}{8} \times 4 + \frac{7}{8} \times 2 \times N_\nu \ . \tag{2.11}$$

Here, we account for photons and positrons as well as neutrinos. In the absence of physics beyond the SM, the number of neutrino flavors at temperatures $T > 1\,\text{MeV}$ is $N_\nu^{(\rm SM)} = 3$. [1] By a comparison between the last two expressions, we compute

[1] At lower temperatures, neutrinos decouple from the thermal bath, and after e^+e^- pair annihilations their temperature is lower than the photons, $T_\nu = (4/11)^{1/3} T_\gamma$. Furthermore, corrections due to non-instantaneous neutrino decoupling lead to a SM effective number of neutrino light flavors $N_{\rm eff}^{(\rm SM)} = 3.04$ [33].

$\Delta N_\nu \equiv N_\nu - N_\nu^{(\mathrm{SM})} = 4\Delta g_*^\phi/7$. We find

$$\Delta N_\nu = \frac{4}{7} g_*(T_r) \left(\frac{g_{*s}(T)}{g_{*s}(T_r)}\right)^{(4+n)/3} \left(\frac{T}{T_r}\right)^n \ . \tag{2.12}$$

This is the general expression for the temperature dependent contribution to the number of additional neutrinos. The temperature T_r cannot be much lower than $T_{\mathrm{BBN}} \simeq 1\,\mathrm{MeV}$, therefore this contribution is vanishing at the time of CMB formation. If we consider T_r around the BBN time, the expression takes the simpler form

$$\Delta N_\nu \simeq \frac{4}{7}\frac{43}{4} \left(\frac{T}{T_r}\right)^n \simeq 6.14 \left(\frac{T}{T_r}\right)^n \ . \tag{2.13}$$

We impose the recent bound on ΔN_ν from Ref. [27], where the authors considered an effective number of relativistic species as in Eq. (2.11), with N_ν constant over the different temperature range probed by BBN. Our case is different, since we have a temperature dependent ΔN_ν. As manifestly shown in Eq. (2.13), such a correction to the number of SM neutrinos increases with the temperature. In order to put the most conservative limits, we evaluate ΔN_ν at a time slightly before neutron freeze-out for temperature $T \simeq 1\,\mathrm{MeV}$. At such a temperature, neutrons and protons are still in chemical equilibrium in the entire range for the parameters (T_r, n) under consideration, as explicitly computed in App. A.2. In this regard, our bounds are very conservative. Ref. [27] found the range $2.3 \leq N_\nu \leq 3.4$ at 95% CL (2σ). The contribution in Eq. (2.13) is always positive, so the BBN bounds only allow the region in the (T_r, n) where

$$T_r \gtrsim (15.4)^{1/n}\ \mathrm{MeV} \ . \tag{2.14}$$

2.4 Dark Matter Freeze-Out

In this section we analyze dark matter freeze-out in the cosmological background introduced in Sec. 2.2. The underlying assumption here is that DM particles achieve thermal equilibrium in the early universe. The conditions needed to satisfy these requirement are given in App. A.1. A DM particle interacting through a light mediator (i.e. lighter than the TeV scale) and with coupling strength at least as big as weak gauge interactions thermalizes at temperatures above the TeV scale. In this regime, DM is produced through freeze-out. We first present the Boltzmann equation describing the DM number density evolution. All the results presented in this Section are obtained by numerically solving this equation. In order to understand the qualitative features of the solutions we found, the semi-analytical solution presented in App. A.3 is very useful. In particular, this solution allows us to estimate the freeze-out temperature and understand the relentless behavior of relics. This regime where DM particles keep annihilating until $T \simeq T_r$ is entered for $n \geq 2$ ($n \geq 4$) if DM annihilations are s-(p-)wave processes. We present explicit solutions for the number density as a function of the temperature, and we quantify the enhancement in the cross section we need with respect to the standard calculation.

Finally, we investigate the relic density dependence on the DM mass. As is well known, the thermal relic density for WIMPs in a standard cosmology depends on the DM mass very weakly (logarithmic, see App. A.3). The quantity that sets the final abundance is the annihilation cross section. We find that this is not the case anymore for a fast expanding universe, since there is a new scale, the temperature T_r. The relative hierarchy between the DM mass and T_r determines whether freeze-out happens before or after the epoch of ϕ domination. The final relic density differ enormously in the two cases, as we discuss extensively in this

Section.

2.4.1 Boltzmann Equation

From now on, we denote χ the DM particle, and we assume it to be a Majorana fermion. The DM number density is governed by

$$\frac{dn_\chi}{dt} + 3Hn_\chi = -\langle\sigma v_{\rm rel}\rangle \left(n_\chi^2 - n_\chi^{\rm eq\,2}\right) \ . \tag{2.15}$$

Here, $n_\chi^{\rm eq}$ and $\langle\sigma v\rangle$ are the equilibrium number density distribution and the thermally averaged cross section, respectively. This is the same as the standard case [8, 9, 10, 11], with one important difference: the Hubble parameter H is different. Assuming $m_\chi \gg T_r$, the energy density at the freeze-out epoch is dominated by ϕ and the Hubble parameters in this regime is given in Eq. (2.8).

As usual, it is convenient to write the Eq. (2.15) in terms of the comoving number density, $Y_\chi = n_\chi/s$, and to use $x = m_\chi/T$ as the "time variable"

$$\frac{dY_\chi}{dx} = -\frac{s\,\langle\sigma v_{\rm rel}\rangle}{H\,x}\left(1 - \frac{1}{3}\frac{\partial\log g_{*s}}{\partial\log x}\right)\left(Y_\chi^2 - Y_\chi^{\rm eq\,2}\right) \ . \tag{2.16}$$

The expression for the comoving equilibrium number density for a Maxwell-Boltzmann distribution is

$$Y_\chi^{\rm eq}(x) = \frac{45\,g_\chi}{4\pi^4 g_{*s}} x^2 K_2(x) \ , \tag{2.17}$$

where $g_\chi = 2$ for a Majorana fermion and $K_2(x)$ is the modified Bessel function. At late times the comoving $Y_\chi(x)$ reaches a constant value $Y_\chi(\infty)$, since the actual number density only changes because of the expansion. The present DM density is $\rho_\chi(T_0) = m_\chi\, Y_\chi(\infty)\, s(T_0)$, where T_0 is the current temperature of the Cosmic

Microwave Background (CMB) photons.

We expand the annihilation cross section times the relative velocity in partial waves

$$\langle \sigma v_{\rm rel} \rangle = \sigma_s + \sigma_p \, x^{-1} + \mathcal{O}(x^{-2}) \ , \tag{2.18}$$

keeping only the leading s- and p-wave contributions. We present numerical results for both cases.

2.4.2 An Earlier Freeze-Out

Before looking at the explicit numerical solution, we examine the qualitative features we expect to find in the solutions. First, and not surprisingly, freeze-out happens earlier than for the case of a radiation background. This is due to the Hubble parameter during the phase of ϕ domination, which for a given temperature is always larger than the associated value in a radiation background. A faster Hubble rate makes it harder for the DM to stay in thermal equilibrium, and freeze-out happens at higher temperatures.

We provide semi-analytical expressions for the freeze-out temperature in Eqs. (A.23) and (A.33) for the case of radiation and modified cosmology, respectively. Keeping the DM mass and the annihilation cross section fixed, and focusing for the purpose of this illustration on s-wave processes, the freeze-out temperatures are related by

$$T_{f\,\rm rad}^{1/2} e^{-m_\chi/T_{f\,\rm rad}} = T_f^{1/2} e^{-m_\chi/T_f} \left(\frac{T_f}{T_r} \right)^{n/2} \ . \tag{2.19}$$

Here, T_r and $T_{f\,\rm rad}$ are the freeze-out temperature in a generic (T_r, n) and the radiation background, respectively. For freeze-out happening during the ϕ dominated epoch, $T_f > T_r$, the freeze-out temperature is larger than the one for the case of a radiation background, $T_f > T_{f\,\rm rad}$. Even if the numerical difference be-

tween the two temperatures is a factor of a few, the consequent modification of the relic density are significant, since freeze-out happens on the exponential tail of the Maxwell-Boltzmann distribution.

2.4.3 Relentless Relics

We point out here a very peculiar and previously unrecognized behavior of the number density evolution once n gets large. In order to understand the physics underlying this feature, it is useful to start the discussion by reviewing what happens right after freeze-out for a standard radiation background. DM particles depart from thermal equilibrium when the interaction rate, $\Gamma \simeq n_\chi \langle \sigma v_{\rm rel} \rangle$ is of the order of the Hubble rate, $H_{\rm rad} \simeq T^2/M_{\rm Pl}$. Immediately after freeze-out, DM particles can still annihilate occasionally, just not enough to stay in thermal equilibrium. The post freeze-out annihilation rate scales as $\Gamma \propto T^3 (T^4)$ for s-wave (p-wave) annihilations, due to the dilution of the DM particles from the expansion of the universe. This is not enough for the annihilation rate to compete with the Hubble rate, and post freeze-out annihilations do not change the density significantly. This can be observed in our numerical solutions, and it can also be understood analytically (see Eq. (A.20)).

We can repeat the same analysis for the set of modified cosmologies considered here. The argument goes along the same lines, with one important difference: the Hubble parameter now scales as $H \propto T^{2+n/2}$. Thus there is a critical value of n above which the post freeze-out annihilation rate scales with a power of temperature lower than the one for the Hubble rate. For s-wave annihilation, this happens for $n \geq 2$. Interestingly, the case $n = 2$ corresponds to motivated theories of quintessence [29, 30]. For p-wave annihilation, the condition for this to be the case is $n \geq 4$.

What are the consequences of this relative scaling? For s-wave annihilating DM and $n \geq 2$ cosmologies, the annihilation rate red-shifts slower than the Hubble rate. The effects of post freeze-out annihilations is then substantial: DM particles keep annihilating, *relentlessly* trying to get to the equilibrium thermal distribution; thermal equilibrium, however, is always unaccessible due to the temperature being low enough for the equilibrium number density to be deeply in the exponential tail. The older the age of the universe, the lower the temperature, and the harder it is for DM particles to get to the equilibrium distribution. The process of depletion goes on until temperatures of the order T_r, when the expansion is driven by the radiation bath, and the usual scaling applies.

2.4.4 Number Density Evolution

We now show results for the full numerical solutions to the Boltzmann equation in Fig. 2.1 and 2.2 for the case of s- and p-wave annihilation, respectively. We take a DM mass $m_\chi = 100\,\mathrm{GeV}$ (we discuss the very important dependence on mass below) and we fix the annihilation cross section in such a way that we reproduce the observed DM abundance for the case of a standard cosmology (red lines). The solutions for the other cosmological histories are obtained by fixing $T_r = 20\,\mathrm{MeV}$ and n as described in the figure caption.

The comoving number density Y in Fig. 2.1 do not change significantly after freeze-out for the radiation (red line) and $n = 1$ (green line) cases. This is expected and consistent with the qualitative analysis above. However, an important difference is already clearly visible: freeze-out happens *earlier* for $n = 1$, than for the $n = 0$ standard case, and as a consequence the asymptotic comoving density is higher.

The phenomenon of *relentless* annihilation is visible in Fig. 2.1 already for the

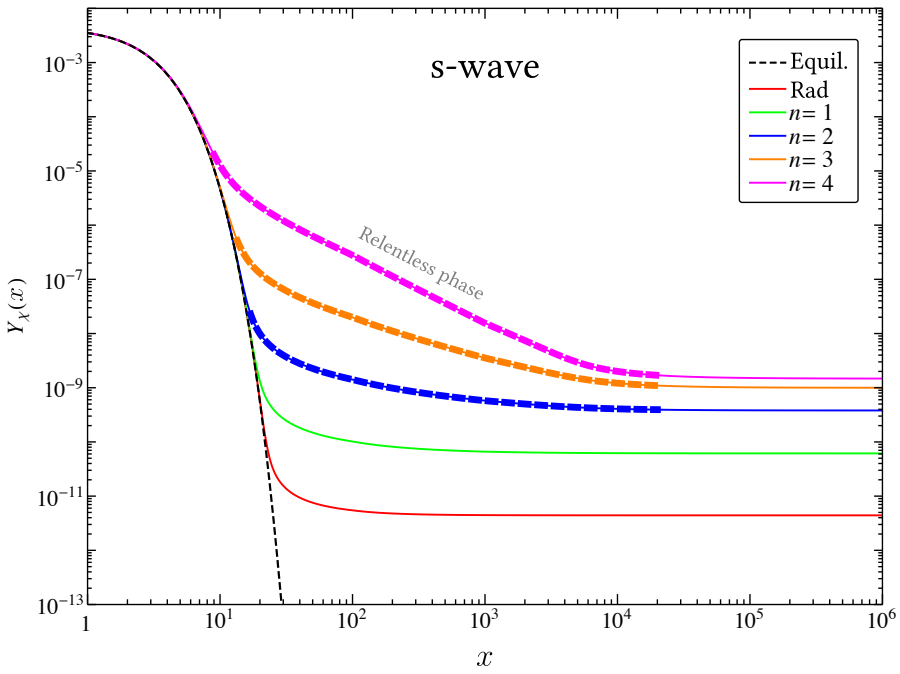

Figure 2.1: Numerical solution of the Boltzmann equation for $m_\chi = 100\,\text{GeV}$ and $\langle\sigma v_{\text{rel}}\rangle = \sigma_s$. The s-wave cross section is fixed to $\sigma_s = 1.7 \times 10^{-9}\,\text{GeV}^{-2}$, which reproduces the observed DM density for a standard cosmology (red line). We set $T_r = 20\,\text{MeV}$ for all n. We highlight the relentless annihilation phase with thicker dashed lines.

$n = 2$ (thick dashed blue line), as also expected from the discussion above: DM particles continue to find each other to annihilate much later than freeze-out, since the Hubble rate and the red-shifting annihilation rate feature the same scaling with temperature, until the universe becomes radiation dominated and eventually $H \gg \Gamma$. The number density evolution in this regime can be understood analytically (see Eqs. (A.27) and (A.29)), and it is closely approximated by the expression

$$Y_\chi(x) \simeq \frac{x_r}{m_\chi\, M_{\text{Pl}}\, \sigma_s} \left[\frac{2}{x_f} + \log(x/x_f)\right]^{-1} . \tag{2.20}$$

Here, x_f and x_r are the freeze-out temperature and T_r expressed in terms of the dimensionless variable $x = m_\chi/T$, respectively. The slow logarithmic decrease of the number density is the result of the *relentless* attempt of the DM to go back to thermal equilibrium. This behavior persists until $T \simeq T_r$, after which the DM comoving number density reaches a constant value.

This post freeze-out annihilation are even more pronounced for $n > 2$, as we can see from the orange and the magenta lines in Fig. 2.1. In this regime for n, the comoving number density is approximated by the following expression

$$Y_\chi(x) \simeq \frac{x_r^{n/2}}{2\, m_\chi\, M_{\rm Pl}\, \sigma_s} \left[x_f^{n/2-2} + \frac{x^{n/2-1}}{n-2} \right]^{-1} \quad . \tag{2.21}$$

The decrease of Y_χ is even faster, with a power law instead of the logarithmic dependence appearing for the marginal case of $n = 2$. As before, the number density keeps decreasing with the behavior described above, until radiation takes over.

The discussion for the p-wave solutions in Fig. 2.2 is analogous: Freeze-out happens earlier and earlier for higher and higher n, and the resulting number density is correspondingly larger. The only difference is that the transition to *relentless* relics sets in at $n = 4$, as correctly estimated above.

2.4.5 Enhancement in the Relic Density

One of the central results of the number density evolution analysis is that freeze-out abundances are in general larger than in the standard case: The red lines is below all the other ones in Figs. 2.1 and 2.2, for fixed values of the annihilation cross section. One can turn the argument around, and state that *larger cross sections* are therefore needed, with the cosmological setup we consider here, to reproduce the observed DM density. This is quite remarkable, as large cross

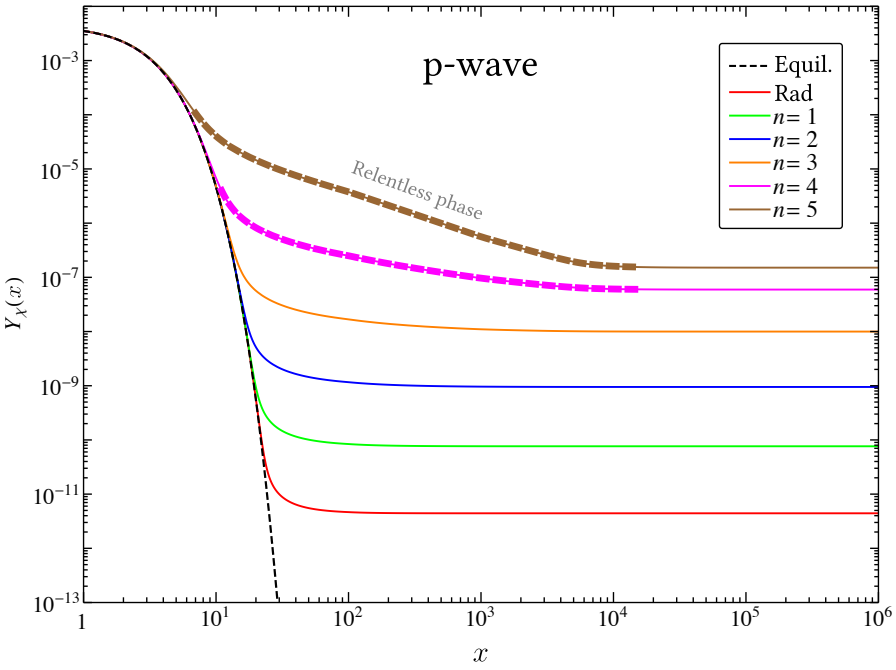

Figure 2.2: Same as Fig. 2.1 but for p-wave annihilation $\langle\sigma v_{\rm rel}\rangle = \sigma_p\, x^{-1}$. The cross section is chosen to reproduce the observed abundance for the standard case, $\sigma_p = 7.56 \times 10^{-8}\,\text{GeV}^{-2}$.

sections translate into larger couplings and therefore larger signals in DM searches, especially in the context of indirect detection. This thus begs the question: How large can the annihilation cross section be, consistently with BBN bounds?

The two dimensional parameter space (T_r, n) entirely fixes the cosmological background in the present setup. At large values of T_r, larger than the DM mass, the standard freeze-out calculation holds, and there is no enhancement to the cross section. The lower T_r, the larger the enhancement; However, we cannot take T_r arbitrarily small, as we have to satisfy the BBN bounds in Eq. (2.14).

The results for s-wave annihilation are shown in Fig. 2.3, where we fix the DM mass to $m_\chi = 100\,\text{GeV}$ and we calculate for each point in the (T_r, n) the cross

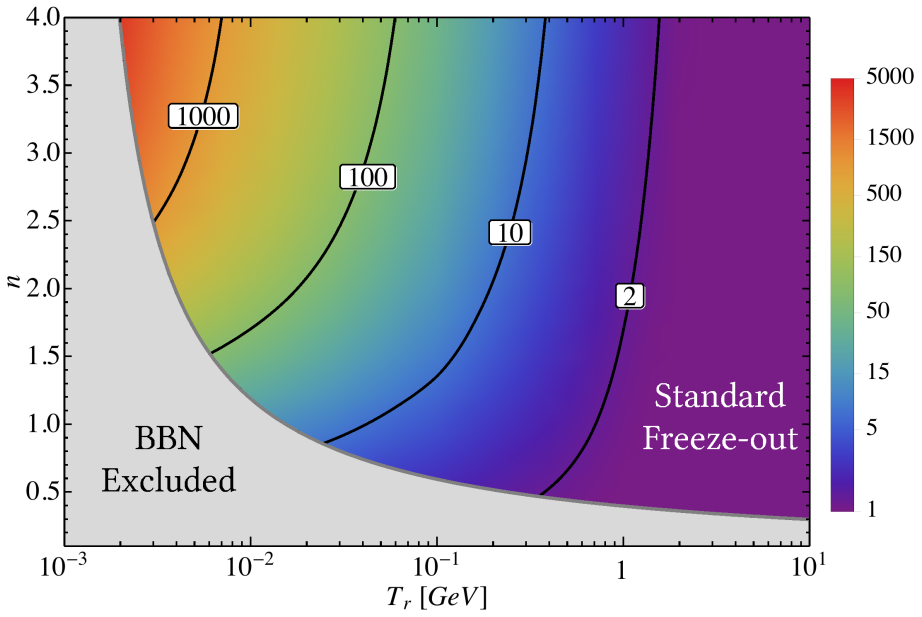

Figure 2.3: Enhancement to the annihilation cross section needed to reproduce the observed DM density due to a cosmological background with a given T_r and n. We fix $m_\chi = 100\,\text{GeV}$, and we provide the result in units of the s-wave cross section $\sigma_s = 1.7 \times 10^{-9}\ \text{GeV}^{-2}$ relative to the standard ($n = 0$) radiation-dominated case. The grey region to the bottom left is excluded by BBN.

section needed to produce the right amount of thermal relic DM, normalized to $\sigma_s = 1.7 \times 10^{-9}\ \text{GeV}^{-2}$, the value producing the "correct" thermal relic density for a radiation background. We checked numerically that within better than 20% accuracy, *the contour lines also correspond to the enhancement to the thermal relic abundance* for a *fixed* value of the pair-annihilation cross section, in Fig. 2.3 $\sigma_s = 1.7 \times 10^{-9}\ \text{GeV}^{-2}$. In the bottom left corner of the figure we shade in grey the region excluded by BBN.

The figure importantly also indicates the *"boost factors"* expected in indirect detection signals, compared to a standard cosmological setup. The key message

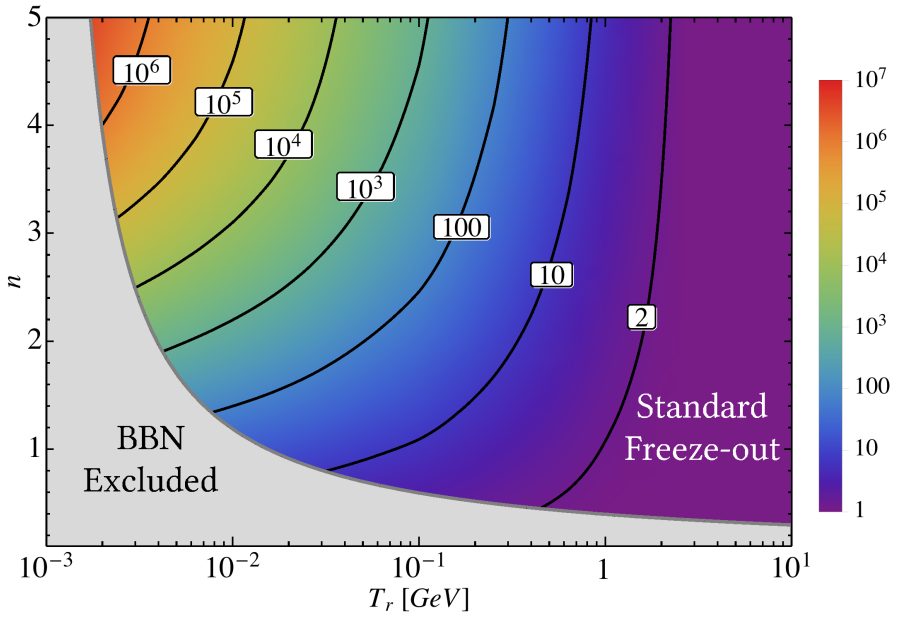

Figure 2.4: As in Fig. 2.3 but for a p-wave annihilation cross section that reproduces the observed abundance for the standard case, $\sigma_p = 7.56 \times 10^{-8}\,\mathrm{GeV}^{-2}$.

is that for the s-wave case enhancements beyond $\sim 10^3$ are possible.

The analogous analysis for p-wave annihilation is presented in Fig. 2.4. As a result of the temperature dependence of the cross section, *larger enhancement factors are possible*, up to $\sim 10^6$ and above. In the case of p-wave annihilation, however, indirect signals are suppressed by the DM velocity in the late universe, thus the enhancement to indirect signals is both smaller than the enhancement factors to the relic density, and dependent on environment.

As a side note, we point out that the effect of relentless annihilation produces significantly *smaller enhancements than what previously calculated in the literature* (see e.g. [31, 32]). This is presumably traced back to the previous calculations having assumed a constant value for the comoving number density after a cer-

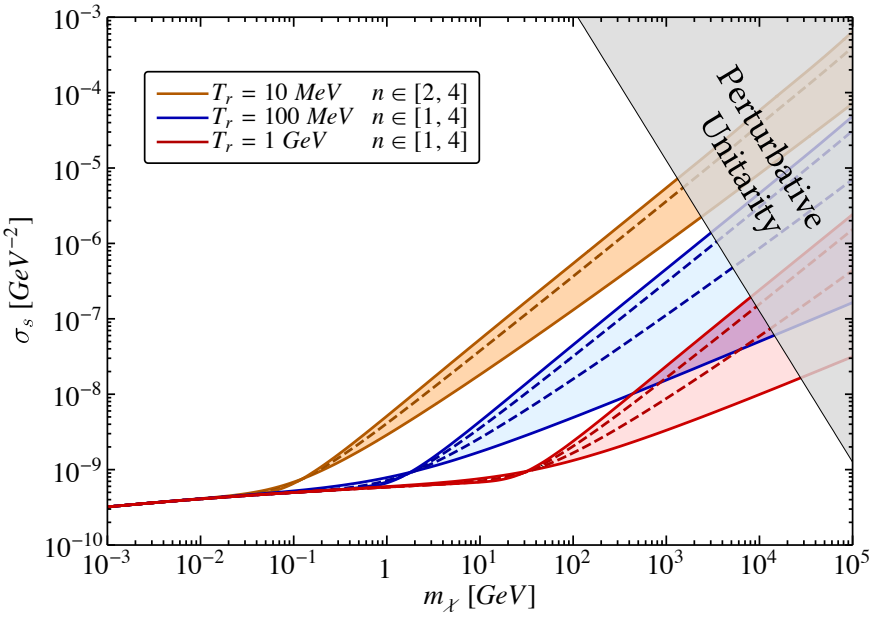

Figure 2.5: Contours of fixed thermal relic density on the (m_χ, σ_s) plane, for given choices of n and T_r, for s-wave annihilation cross section (the dashed red and blue lines correspond to, from bottom to top, $n = 2$ and 3, while the dashed orange line to $n = 3$) . The top right corner is in conflict with limits from perturbative unitarity [1].

tain effective freeze-out temperature, thus neglecting the *relentless* annihilation potentially affecting the relic density over several decades in temperature.

2.4.6 Dependence on the DM mass

All the results presented so far assumed the fixed DM mass benchmark value $m_\chi = 100\,\text{GeV}$. For a cold relic in a standard cosmology, the value of the DM mass has a weak impact on the final abundance, which is controlled by the annihilation cross section. We conclude this Section by pointing out one more interesting feature than the framework discussed in this work: the relic density has a strong

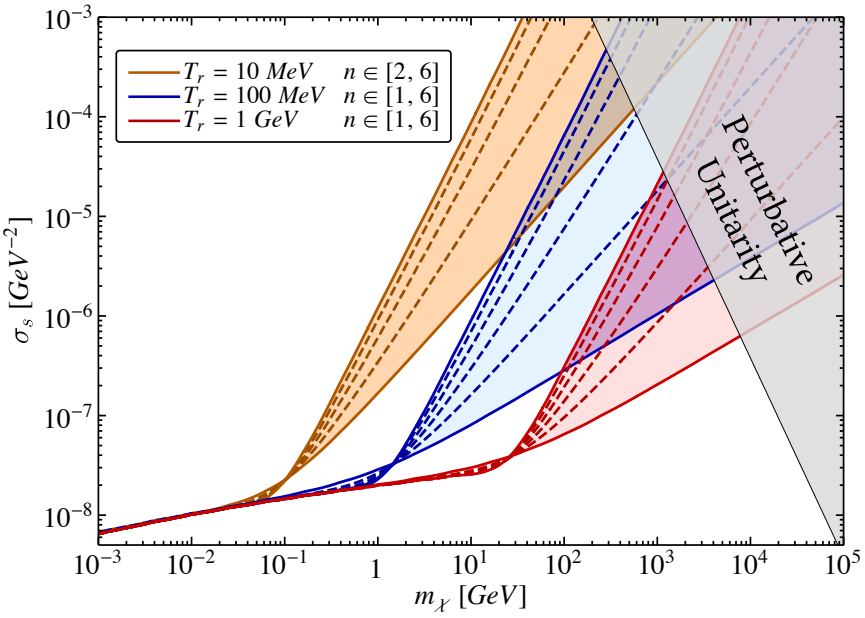

Figure 2.6: As in Fig. 2.5, but for p-wave annihilation cross sections. The intermediate dashed lines, from bottom to top within each shaded region, correspond to increasing integer values of n.

dependence on the DM mass.

The reason why this is the case is the presence of the critical temperature T_r. If the freeze-out temperature is below T_r, there is no change with respect to the standard story. In the opposite case, the precise value of the DM mass is important. Freeze-out happens at temperatures $T_f \simeq m_\chi/10$, thus the larger the DM mass, the longer the DM particle *relentlessly* reduce its comoving number density through residual annihilations. Again, this means that compared to previous calculations the larger the ratio of m_χ/T_r, the larger the effect and the larger the suppression of the calculated enhancement to the thermal relic density.

To quantitatively study this effect, we fix a few benchmark cosmologies and show contours of fixed relic density in the $(m_\chi, \sigma_{s,p})$ plane. The results are shown

in Figs. 2.5 and 2.6 for s-wave and p-wave annihilation cross sections, respectively. At low values of the DM mass, corresponding to a freeze-out temperature below T_r, these lines are close to horizontal: This is expected, as in the standard case the relic density depends only on the cross section. The mild dependence on the mass comes from two factors: (i) the logarithmic mass dependence of the freeze-out temperature, and (ii) the different value of g_* at the freeze-out. However, for larger DM mass we see that the relic density strongly depends on the mass, since the larger the DM mass, the longer the phase of *relentless* annihilation, and the ensuing suppression of the relic density. In the figure we also indicate, in the top-right corners, regions in conflict with perturbative unitarity [1]. Comparing Figs. 2.5 and 2.6 one can also appreciate the steeper dependence on mass in the p-wave case. This arises because of the steeper dependence of Γ on temperature in the p-wave case, and is already reflected in the larger enhancements we find, e.g., in Fig. 2.4 compared to Fig. 2.3.

2.5 Ultra Stiff Fluids

A virtue of the freeze-out analysis performed in the previous Section is its generality and model independence. Any DM particle thermalized in the cosmological background of Eq. (2.6) is produced through freeze out as described in Sec. 2.4. The analysis only assumes our knowledge of the two parameters (T_r, n), without the need of specifying any further property of the new species ϕ. In this last part of this chapter, we provide explicit microscopic realizations for ϕ, reproducing the red-shift behavior in Eq. (2.2).

All the examples we consider are theories of a single real scalar field ϕ mini-

mally coupled to gravity

$$S = \int d^4x \sqrt{-g} \left(-\frac{1}{2} g^{\mu\nu} \partial_\mu \phi \partial_\nu \phi - V(\phi) \right) \ . \tag{2.22}$$

For the remaining of this Section, we set $M_{\rm Pl} = 1$. The energy density and pressure for this fluid read

$$\begin{aligned} p_\phi = & \ \frac{1}{2} \left(\frac{d\phi}{dt} \right)^2 - V(\phi) \ , \\ \rho_\phi = & \ \frac{1}{2} \left(\frac{d\phi}{dt} \right)^2 + V(\phi) \ , \end{aligned} \tag{2.23}$$

leading to the equation of state

$$w_\phi = \frac{p_\phi}{\rho_\phi} = \frac{\frac{1}{2} \left(\frac{d\phi}{dt} \right)^2 - V(\phi)}{\frac{1}{2} \left(\frac{d\phi}{dt} \right)^2 + V(\phi)} \ . \tag{2.24}$$

For such an equation of state, the energy density red-shifts as $\rho_\phi \propto a^{-3(1+w_\phi)}$, which allows us to connect

$$n = 3 w_\phi - 1 \ , \tag{2.25}$$

where n is the index defined through the red-shift behavior in Eq. (2.2). For a positive scalar potential, the allowed values of w_ϕ are in the range $(-1, +1)$. Equivalently, the range for n is between -4 and $+2$. The highest n is achieved during a kination phase, where the energy density of ϕ is mostly kinetic. In order to get values larger than $n = 2$, we need to consider negative scalar potentials. In what follows, we first describe examples of fluids with $n = 2$ and then we show how the $n > 2$ domain can be accessed.

2.5.1 Quintessence ($n = 2$)

Examples of theories with $n = 2$ are quintessence fluids motivated by the discover of the accelerated expansion of the universe [29, 30]. The energy density of this type of fluid red-shifts as $\rho_\phi \propto a^{-6}$ in the kination regime, i.e. when the kinetic energy density dominates over the potential energy . One possible scalar potential leading to this behavior is the exponential form [34, 35]

$$V(\phi) = \exp\left[-\lambda\phi\right] \ . \tag{2.26}$$

The role of quintessence for neutralino dark matter freeze-out was studied in Refs. [31, 32]. Alternatives to quintessence, still with the same red-shift behavior, are Chaplygin gas [36] or a perfect fluid described by a polytropic equation of state [37].

2.5.2 Faster than Quintessence ($n > 2$)

We provide here example theories where $n > 2$. We assume the energy density of the universe to be entirely dominated by ϕ, with red-shift as in Eq. (2.2). The scale factor vs time relation can be derived from the Friedmann equation

$$a(t) = a_i \left(\frac{t}{t_i}\right)^{2/(n+4)} \ , \tag{2.27}$$

where we define a_i to be the value of the scale factor at $t = t_i$. The time derivative of the Hubble parameter reads

$$\frac{dH}{dt} = -\frac{1}{2}(\rho_\phi + p_\phi) = -\frac{1}{2}\left(\frac{d\phi}{dt}\right)^2 \ . \tag{2.28}$$

By comparing this expression with the one resulting from direct calculation, $dH/dt = -2/[(n+4)t^2]$, we find the time evolution of the field

$$\phi(t) = \phi_i + \frac{2}{\sqrt{n+4}} \ln\left(\frac{t}{t_i}\right) \ . \tag{2.29}$$

We go back to Eq. (2.24), and if we assume that $w_\phi = \text{const}$ we can solve for the scalar potential

$$V(\phi) = -\frac{1}{2}\left(\frac{n-2}{n+4}\right)\left(\frac{d\phi}{dt}\right)^2 \ , \tag{2.30}$$

where we have traded w_ϕ with n by using Eq. (2.25). The time derivative of the field ϕ is related to the one of the Hubble parameter, as shown in Eq. (2.28). We know how the Hubble parameter scales with time in this background with $w_\phi = \text{const}$, therefore we can find an expression for the potential as a function of time. Once this is done, we use Eq. (2.29) to trade the time variable with ϕ. The output of this procedure is the scalar potential as a function of the field

$$V(\phi) = V_i \, e^{-\sqrt{n+4}\,\phi} \ . \tag{2.31}$$

The overall constant reads

$$V_i = -\frac{2(n-2)}{(n+4)^2 \, t_i^2} \, e^{\phi_i \sqrt{n+4}} \ , \tag{2.32}$$

and it is negative for $n > 2$. It is straightforward to check that the solution in Eq. (2.29) with the potential above satisfies the equation of motion $\ddot{\phi} + 3H\dot{\phi} + dV(\phi)/d\phi = 0$, as it should. This class of potentials have been used in the context of ekpyrotic scenario [38]. A dynamical $w_\phi > 1$ can be obtained also with periodic potentials [39, 40].

2.5.3 No superluminal propagation

We conclude this Section with one important comment. The regime $w_\phi > 1$ implies $p_\phi > \rho_\phi$, and there may be concerns about superluminal propagation. However, the speed of sound for a canonical scalar field with action as in Eq. (2.22) is always $c_s^2 = 1$ [41, 42]. Consequently, causality is not violated.

2.6 Discussion and Conclusions

We analyzed DM freeze-out for non-standard cosmological histories which include a faster-than-usual expansion at early times, driven by a new cosmological species ϕ. We gave a full description of the cosmological backgrounds in Sec. 2.2. We then parameterized the possible cosmological histories by the values of n and T_r, i.e., respectively, the index appearing in Eq. (2.2) and the temperature when the energy densities of ϕ and radiation are equal. Light element abundances exclude part of this two-dimensional parameter space, and this BBN bound is summarized by Eq. (2.14) of Sec. 2.3.

In calculating the DM density evolution we identified two distinct possibilities: For n not too large, the behavior is quite similar to the one for standard freeze-out, where shortly after chemical decoupling the comoving number density approaches its asymptotic value. For large n, however, we found a new domain where post freeze-out annihilation substantially dilute the DM density. This is explained by the different scaling of the Hubble parameter with temperature, $H \propto T^{2+n/2}$; we called this possibility *relentless* dark matter. The critical values of n dividing the two regimes are $n = 2$ and $n = 4$ for s-wave and p-wave annihilation, respectively.

A central result of our analysis is that DM particles which freeze out in the cosmological era dominated by the new species ϕ must have cross sections way

larger than the thermal value in Eq. (2.1) if DM is to be a thermal relic. We plan to study in the future the implications for dark matter searches of such a large annihilation cross section, such as CMB spectral distortion [43] and bounds from gamma rays [44].

The underlying assumption of our study of DM genesis was an early time thermalization. As discussed in App. A.1, this is not necessarily the case, and the faster expansion makes things even harder. If our assumption is not satisfied, DM production would be non-thermal. Assuming production from a decay and/or scattering of particles in the thermal bath, the comoving density produced at a given temperature T approximately reads

$$Y_\chi(T) \simeq \Gamma(T) H(T)^{-1} \simeq \Gamma(T)\, M_{\rm Pl}\, T^{-2-n/2} \,. \tag{2.33}$$

If the rate is mediated by a higher dimensional operator of mass dimension d, it would scale as $\Gamma(T) \propto T^{2d-7}$. Thus the comoving density at a given temperature scales as $Y_\chi(T) \propto T^{2d-n/2-9}$. We see that the relative size of d and n establishes where most of DM particles are produced. If the dimension is not too large, $d < n/4 + 4.5$, the production is dominated at lower temperature, of the size of the decaying/scattering bath particles. This type of "IR production" is known as freeze-in [45]. In the opposite case, $d > n/4 + 4.5$, the production is dominated by scattering at high temperatures, similarly to the UV production of axinos or gravitinos [46, 47]. This latter case is especially interesting, because it requires the knowledge of how the universe entered the ϕ domination phase after inflation. We will study both possibilities in a forthcoming analysis.

Chapter 3

Freeze-in in Modified Cosmologies

3.1 Introduction

The subject of this chapter is DM freeze-in, another motivated mechanism for DM genesis where the relic density, in a standard cosmological setting can be calculated directly from the DM particle physics properties [45, 51]. The same caveat as above applies to this case: a modified, non-standard thermal history will affect the predicted final density of DM from freeze-in. Our goal here is to perform a general analysis of DM freeze-in in a fast expanding universe, similarly to what we performed for freeze-out in Ref. [49], and to draw the critical phenomenological consequences of such scenario. DM particles produced through freeze-in are very weakly coupled with the primordial plasma and never attain thermal equilibrium in the early universe. Although very weak, the interactions with bath particles B_i are enough to create DM particles χ through reactions $B_i \to \chi$. After χ is produced, it simply red-shifts away and it is still present today contributing to

the observed DM energy density.

The set of cosmological histories considered in this work is phenomenologically described by the two-dimensional parameter space (T_r, n). Here, T_r is the temperature where the energy density of ϕ equals the one of the radiation bath, whereas $n > 0$ is the index describing how the fluid red-shifts through the relation $\rho_\phi \propto a^{-(4+n)}$. These two parameters cannot take arbitrary values, since they are bound by BBN constraints [49] which constrains the Hubble expansion rate, and hence the energy density of the universe at temperatures around when BBN operates to be close to pure radiation-domination.

In the spirit of a very general analysis, we consider the following freeze-in scenarios to produce DM particles χ through reactions involving bath particles B_i:

1. **Decay $B_1 \to B_2\chi$:** a bath particle B_1, heavier than χ, decays to a final state involving one DM particle and other bath particles (which we indicate generically with the symbol B_2). While we consider a two-body decay for illustration, our results are valid for general n-body decays. The discussion for decay channels involving more than one DM particle (e.g. $B_1 \to \chi\chi$) in the final state is analogous.

2. **Single Production $B_1B_2 \to B_3\chi$:** Collisions between two bath particles lead to *one* DM particle in the final state. This reaction happens, for example, when one initial state bath particle shares the same discrete quantum number with χ, e.g. when both B_1 and χ are odd under a $\mathbb{Z}_2$ symmetry.

3. **Pair Production $B_1B_2 \to \chi\chi$:** Collisions between two bath particles lead to *two* DM particles in the final state. We separate this case from the one above since it happens in different theories. As an example, χ can be the *only* particle odd under a $\mathbb{Z}_2$ symmetry, and it thus needs to be pair produced.

g/g_{standard}	early MD era	fast-expanding universe
DM freeze-out	smaller	larger
DM freeze-in	larger	larger

Table 3.1: Comparison between couplings needed to produce the observed DM abundance in a standard versus modified cosmological setting, for the two cases an early MD era and of a fast expanding universe. We consider both DM freeze-out and freeze-in, and for each case we identify whether the required coupling to the plasma is smaller or larger than the standard case.

A consistent picture emerges from our analysis of different cosmological histories and of various freeze-in scenarios: the observed DM abundance is reproduced for *larger* couplings between DM and plasma particles compared to standard cosmological histories. This conclusion was also reached for freeze-in in an early MD epoch [22, 26, 52]. A comparison among different cases is provided in Tab. 3.1. The general, key conclusion of our study is that *DM genesis in a fast expanding universe, be it via freeze-out or via freeze-in, always requires larger couplings, with the inescapable prediction of enhanced signals for DM detection*.

We note that freeze-in through pair production of DM particles (case 3 above) but limited to the specific case $n = 2$ (kination domination) was studied in Refs. [53, 54]. The goal of this chapter is to present, instead, a *general* analysis for different cosmological histories and freeze-in scenarios. For the particular case of $n = 2$ our results are consistent with those presented in Refs. [53, 54].

The reminder of this study has the following outline: After reviewing the Boltzmann equation for freeze-in with the modified cosmological background in Sec. 3.2, we consider freeze-in production of DM in the early universe. As explicitly stated, we only focus on IR production (*i.e.* production dominated by processes occurring at low temperatures, close to the bath particle masses). While this is always the case for decays, we identify under which circumstances IR production occurs from scattering as well. By focusing on IR production, we avoid issues

related to the uncertain history of the universe *before* the time of ϕ-domination. We then divide the following discussion into two parts: we deal with decay in Sec. 3.3 and with scattering in Sec. 3.4. Wherever relevant, we highlight the most prominent possible experimental signals associated with freeze-in within a non-standard cosmological history with faster-than-usual expansion rates at early times. We summarize our results in Sec. 3.5.

3.2 Boltzmann Equation for Freeze-In

The number density of DM particles χ evolves in an isotropic and homogeneous early universe according to the Boltzmann equation

$$\frac{dn_\chi}{dt} + 3Hn_\chi = \mathcal{C}_\alpha \ . \tag{3.1}$$

The second term on the left-hand side accounts for the Hubble expansion, whereas number-changing reactions which, here, produce DM particles are accounted for by the collision operator on right-hand side. This collision operator $\mathcal{C}_\alpha$ depends on the specific reaction under consideration (e.g. $\alpha = B_1 \to B_2\chi$). It also generically depends on time, or, equivalently, on the temperature of the radiation bath.

The boundary condition we assume for the Boltzmann equation (3.1) is a vanishing DM number density at very early times. In other words, we are assuming here that physics at high scale (e.g. inflation) produces a negligible number of χ particles, which are then exclusively produced in the later universe by the freeze-in reactions listed in the Introduction.

It is convenient to re-cast the Boltzmann equation factoring out the effect of expansion. To this end, as customary, we define the *comoving number density* $Y_\chi = n_\chi/s$, where s is the entropy density. Using the definition of the comoving density,

together with the assumed conservation of entropy, $sa^3 = \text{const}$, we rewrite the Boltzmann equation as

$$\frac{dY_\chi}{d\log T} = -\left(1 + \frac{1}{3}\frac{\partial \log g_{*s}}{\partial \log T}\right)\frac{\mathcal{C}_\alpha}{H\,s}\ . \tag{3.2}$$

Finally, we introduce the dimensionless "time variable" $x = m_B/T$, where m_B is typically the mass scale of some bath particles that we will specify for each case. Upon using the general relation $df/d\log T = -df/d\log x$, we find the final form of the Boltzmann equation

$$\frac{dY_\chi}{d\log x} = \left(1 - \frac{1}{3}\frac{\partial \log g_{*s}}{\partial \log x}\right)\frac{\mathcal{C}_\alpha(x)}{H(x)\,s(x)}\ , \tag{3.3}$$

where we make explicit the x-dependence (i.e. time, or inverse temperature) of the Hubble parameter H, the entropy density s and the collision operator $\mathcal{C}_\alpha$.

In the next Sections, we specify each time our choice for x and what reaction α we are considering. Before discussing the freeze-in process, we conclude this Section with a brief review of the cosmological background and a comparison between IR and UV production.

3.2.1 The cosmological background

We are interested in DM production for cosmological histories where the universe is dominated by a new species ϕ, whose red-shift behavior is $\rho_\phi \propto a^{-(4+n)}$. Since entropy is conserved, during the time of ϕ-domination the energy density scales as $\rho_\phi \propto T^{-(4+n)}$, where T is the temperature of the radiation bath. The Friedmann equation allows us to identify the relation $H \propto T^{-(2+n/2)}$.

Motivated theories leading to this faster Hubble expansion can be found in models for dark energy and/or inflation (see e.g. Refs. [55, 34, 35, 29, 30, 39,

36, 38, 40, 37, 56, 50]. Famously, quintessence theories explaining the current acceleration feature an early phase where the universe is dominated by the kinetic energy of a new scalar field (kination regime), which is equivalent to the case $n = 2$ in our parameterization. An even faster expansion can be achieved in the context of ekpyrotic scenarios, since larger values $n > 2$ are needed to smooth the universe out in the contracting phase. An explicit example of a microscopic theory leading to the $n > 2$ expansion was provided in Ref. [49].

Regardless of the microscopic theory, the Hubble parameter at a fixed temperature is always larger than its associated value for a standard history at the same temperature when the universe is dominated by ϕ. This is why the cosmological histories considered in this work are the ones for a *fast expanding universe*. A complete description of these histories and how BBN bounds the parameter space can be found in Ref. [49]. Here, we summarize the key results.

When the universe is dominated by ϕ, the Hubble parameter at a fixed temperature is always larger than its associated value for a standard history at the same temperature. This is why the cosmological histories considered in this work are the ones for a *fast expanding universe*. A complete description of these histories and how BBN bounds the parameter space can be found in Ref. [49]. Here, we summarize the key results.

The cosmological background is identified by two parameters: (T_r, n). The temperature T_r is set by some boundary condition, and we choose it to be the temperature where the energy density of ϕ and radiation are the same. The index n described the red-shift behavior. The energy density of ϕ as a function of the radiation bath temperature is given by

$$\rho_\phi(T) = \rho_\phi(T_r) \left(\frac{g_{*s}(T)}{g_{*s}(T_r)} \right)^{(4+n)/3} \left(\frac{T}{T_r} \right)^{(4+n)} . \tag{3.4}$$

The total energy density at any temperature reads

$$\rho(T) = \rho_{\rm rad}(T) + \rho_\phi(T) = \\ \rho_{\rm rad}(T)\left[1 + \frac{g_*(T_r)}{g_*(T)}\left(\frac{g_{*s}(T)}{g_{*s}(T_r)}\right)^{(4+n)/3}\left(\frac{T}{T_r}\right)^n\right] \ , \tag{3.5}$$

where we factor out the energy density of the radiation bath. The Hubble parameter as a function of the temperature can be computed using Friedmann's equation

$$H = \frac{\sqrt{\rho}}{\sqrt{3}\, M_{\rm Pl}} \ , \tag{3.6}$$

where the reduced Planck mass is $M_{\rm Pl} = (8\pi G)^{-1/2} = 2.4 \times 10^{18}\,\text{GeV}$. This is the expression for the Hubble parameter, with the energy density ρ as given in Eq. (3.5). The Hubble parameter $H(T)$ enters the Boltzmann equation (3.3), which we use to compute the DM relic density. All results in this chapter are obtained via a numerical calculation with this complete expression for the Hubble parameter. However, in order to perform simple analytical estimate, it is useful to give an approximate expression for the Hubble rate at temperatures larger than T_r

$$H(T) \simeq \frac{\pi\, \overline{g}_*^{1/2}}{3\sqrt{10}}\frac{T^2}{M_{\rm Pl}}\left(\frac{T}{T_r}\right)^{n/2} \ , \qquad (T \gg T_r) \ , \tag{3.7}$$

where we take $g_{*s}(T) = g_*(T) = \overline{g}_* = \text{const}$. The full matter content of the Standard Model gives $\overline{g}_* = g_{*\rm SM} = 106.75$. Finally, as found in Ref. [49], BBN bounds the cosmological parameters to be

$$T_r \gtrsim (15.4)^{1/n}\ \text{MeV} \ . \tag{3.8}$$

The cosmological history introduce here and parameterized by (T_r, n) cannot be extrapolated arbitrarily back in time. As we consider a younger universe, or

equivalently as we go to higher temperature, the energy density of ϕ gets larger. We identify the temperature when we reach the value $\rho_\phi \sim M_{\rm Pl}^4$, and we set this as a limit above which we cannot use our framework anymore. This in turns imply a constraint on $T_{\rm RH}$, the reheating temperature after inflation. We find the bound

$$T_{\rm RH} \lesssim M_{\rm Pl} \left(T_r/M_{\rm Pl}\right)^{n/(n+4)} \ . \tag{3.9}$$

In Fig. 3.1, we visualize this upper bound on the reheating temperature in the (T_r, n) plane. We consider the region of this plane correspondent to the set of cosmological histories analyzed in the following study, and we also shade away the region excluded by the BBN bound in Eq. (3.8). In all the parameter space of interest, this bound is several orders of magnitude above the masses of the particles considered in this work. As explained in the following sub-section, we will only consider IR production, namely freeze-in processes mostly active at temperatures around the typical masses of the particles involved in the reactions. Thus we can safely assume that $T_{\rm RH}$ is well above the masses under consideration, but still well below the upper bound given in Fig. 3.1.

3.2.2 IR vs. UV production

A remarkable feature of freeze-in is that DM production, with a standard cosmological history, is always IR dominated [45]. In this section we show that this is always the case for freeze-in from decays, even in the case of a modified cosmological history with a fast-expanding universe at early times. If DM particles are produced via scattering processes, instead, the production with a standard cosmological history is IR dominated as long as the interactions between DM and the bath particles are renormalizable. We conclude this Section with a comparison between IR and UV production for the cosmological histories considered in this

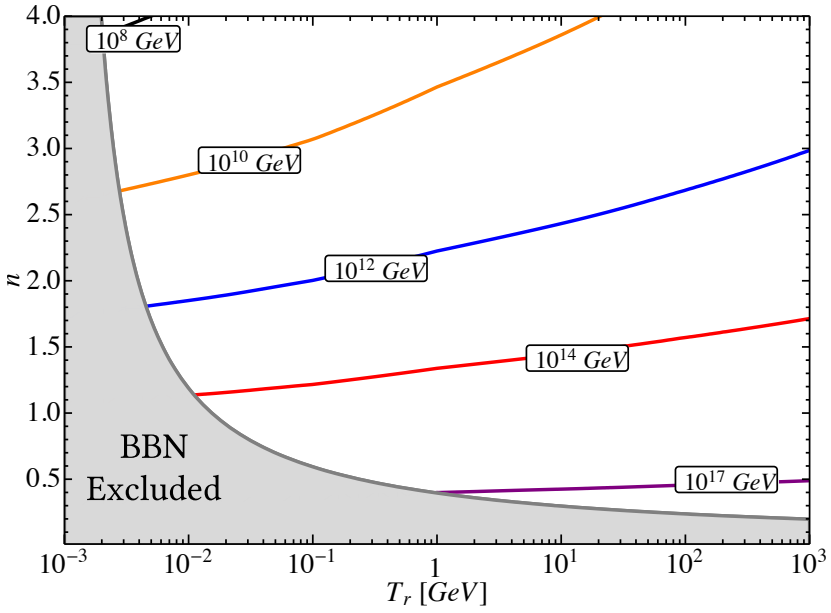

Figure 3.1: Upper bound on the reheat temperature after inflation $T_{\rm RH}$ in the (T_r, n) plane. The gray region is excluded by BBN.

work.

Our assumption through this work is that at very high temperatures the abundance of χ is negligible. As the temperature drops down, DM particles are created via processes involving the plasma particles. At a given temperature T, much higher than the DM and the bath particles masses, the comoving abundance of χ particles approximately reads

$$Y_\chi(T) \simeq \gamma(T)\, H(T)^{-1} \ . \tag{3.10}$$

Here, $\gamma(T)$ is the (temperature dependent) rate for the process under consideration, whereas the inverse Hubble parameter is about the age of the universe. This simple relation allows to establish whether the production is IR or UV dominated.

We start from the case of decays, $B_1 \to B_2\chi$, where the rate scales as $\gamma_{B_1\to B_2\chi}(T) \simeq \Gamma_{B_1\to B_2\chi}\, m_{B_1}/T$. The partial width computed in the rest frame of B_1 is corrected by the Lorentz time dilatation factor. Upon using the approximate Hubble parameter in Eq. (3.8), and neglecting numerical factors, we find for decays

$$Y_\chi(T)|_{B_1\to B_2\chi} \simeq \Gamma_{B_1\to B_2\chi}\, \frac{m_{B_1} M_{\rm Pl}\, T_r^{n/2}}{T^{3+n/2}}\ . \tag{3.11}$$

Thus freeze-in from decays is always dominated at low (IR) temperatures.

For the case of scattering, the temperature dependence of the rate stems from the type of interaction under consideration. If we take an operator of mass dimension d as responsible for the scattering process, the rate scales $\gamma_{B_1\to B_2\chi}(T) \propto T^{2d-7}/M_*^{2d-8}$, where M_* is the mass scale appearing in the operator. The comoving density scales with the temperature as

$$Y_\chi(T)|_{B_1B_2\to B_3\chi} \propto \frac{T^{2d-9-n/2}}{M_*^{2d-8}}\frac{M_{\rm Pl}}{T_r^{n/2}}\ . \tag{3.12}$$

The scaling for the case $B_1B_2 \to \chi\chi$ is identical. Thus for freeze-in via scattering the production is IR dominated only for operators whose mass dimension satisfies

$$d < 4.5 + \frac{n}{4}\ . \tag{3.13}$$

The case $n = 0$ corresponds to a standard history, and for this case freeze-in is IR dominated only for renormalizable interactions, as correctly identified in Ref. [45].

We always consider IR production in this work. And in doing so we avoid the complication of specifying how the cosmological phase of ϕ domination arises at very high temperatures. All we assume here is that at temperatures above the plasma particle masses ϕ domination sets in, and DM particles are produced at

around the mass scale of the bath particles. As discussed above, this is automatic for decays, whereas for scattering IR production only applies for interactions satisfying Eq. (3.13). The comoving number density at any "time" x can be computed from Eq. (3.14) by solving a numerical integral

$$Y_\chi(x) = \int_0^x \frac{dx'}{x'} \left(1 - \frac{1}{3}\frac{\partial \log g_{*s}}{\partial \log x'}\right) \frac{\mathcal{C}_\alpha(x')}{H(x')\, s(x')} \ . \tag{3.14}$$

Here, the lower integration extreme ($x' = 0$) is justified by IR production. The final DM density is given by taking $x \to \infty$ in the above equation.

3.3 Freeze-In from Decays

We start with the case where DM particles are produced through the decay process

$$B_1 \to B_2 \chi \ . \tag{3.15}$$

We provide a complete derivation of the collision operator for this process in Eq. (B.7) of App B.1. Here, we only quote the final result,

$$\mathcal{C}_{B_1 \to B_2 \chi} = n_{B_1}^{\rm eq}\, \Gamma_{B_1 \to B_2 \chi}\, \frac{K_1[m_{B_1}/T]}{K_2[m_{B_1}/T]} \ . \tag{3.16}$$

For the case of decays, it is convenient to choose $x = m_{B_1}/T$. Furthermore, we take the equilibrium distribution from Eq. (B.3), and we rewrite the collision operator for decays as a function of the variable x

$$\mathcal{C}_{B_1 \to B_2 \chi} = \frac{g_{B_1}\, m_{B_1}^3}{2\pi^2}\, \frac{K_1[x]}{x}\, \Gamma_{B_1 \to B_2 \chi} \ . \tag{3.17}$$

The comoving density at any temperature can be computed by applying the

general result in Eq. (3.14). After plugging the explicit expression for the entropy density, the freeze-in comoving density reads

$$Y_\chi(x) = g_{B_1}\,\frac{45}{4\pi^4}\,\Gamma_{B_1\to B_2\chi}\times \int_0^x dx'\left(1-\frac{1}{3}\frac{\partial\log g_{*s}}{\partial\log x'}\right)\frac{K_1[x']\,x'}{g_{*s}(x')\,H(x')}\ . \tag{3.18}$$

This is our master equation to compute freeze-in production via decays. The only assumption so far is that entropy is conserved, thus this equation is also valid for the case of a standard thermal history. The details of the thermal history under consideration enter through the Hubble parameter $H(x')$ in the denominator of the integrand.

3.3.1 Number Density Evolution

We parameterize the partial decay width with the expression

$$\Gamma_{B_1\to B_2\chi} = \frac{\lambda_d^2}{8\pi} m_{B_1}\ . \tag{3.19}$$

Here, $\lambda_d \ll 1$ is a very small coupling mediating the decay process, whereas the factor of 8π in the denominator accounts for the phase space of the two-body final state.

The freeze-in number density of χ particles is determined by Eq. (3.18) once we specify the mass of the decaying particle and the coupling λ_d. The asymptotic value for the number density is found by taking the $x \to \infty$ limit, whereas the energy density is obtained by just multiplying the previous result by the mass of χ. As an illustrative example, we fix $(m_{B_1}, m_\chi) = (1000, 10)$ GeV, and we also fix $g_{B_1} = 2$. The observed DM abundance for a standard cosmological history is achieved if we choose $\lambda_d^{\rm rad} = 1.22\times 10^{-11}$. In Fig. 3.2 we keep these particle

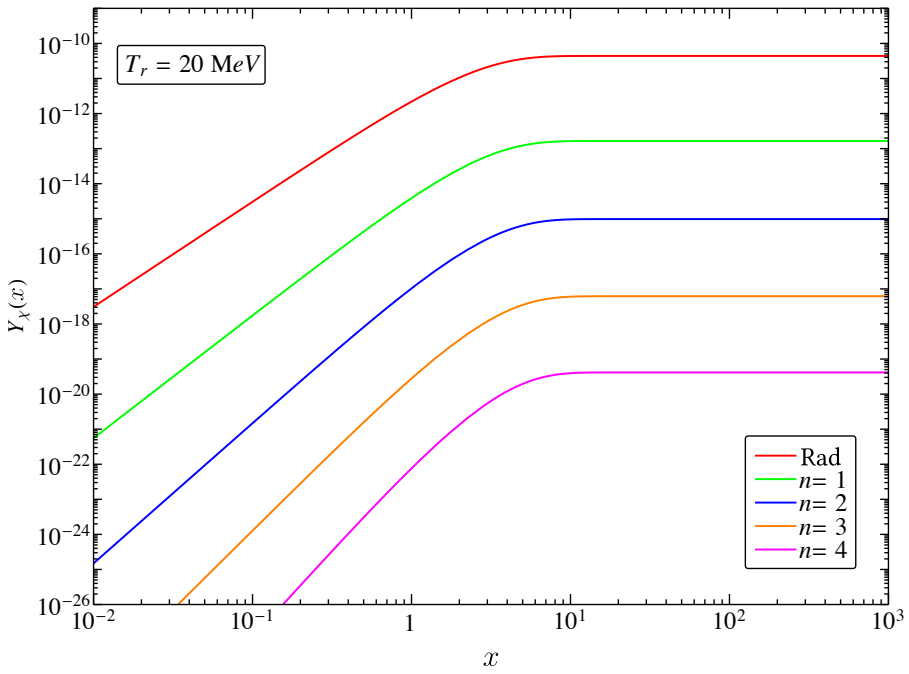

Figure 3.2: Numerical solutions for the comoving number density Y_χ for the case of freeze-in from decays. We choose $g_{B_1} = 2$, $m_\chi = 10\,\text{GeV}$, $m_{B_1} = 1\,\text{TeV}$, and $\lambda_d = \lambda_d^{\text{rad}} = 1.22 \times 10^{-11}$. We always set $T_r = 20\,\text{MeV}$.

physics parameters constant, and we show numerical solutions for different modified cosmological histories. We always take $T_r = 20\,\text{MeV}$, consistently with BBN bounds, and we show solutions for different values of n.

Fig. 3.2 illustrates well our findings: the asymptotic comoving density consistently decreases as we increase the value of the index n. In a fast expanding universe, the freeze-in production from bath particle decays is less effective than in the case of a standard cosmological history (red line). As a result, larger couplings are required to reproduce the observed DM density. Moreover, for each given temperature the comoving density is always lower as we consider larger values of n. Correspondingly, the same freeze-in yield is achieved at lower temperatures.

The results in Fig. 3.2 are readily explained by an approximate solution to the Boltzmann equation. (We remind the Reader that what shown in the plot was obtained by numerically solving the integral in Eq. (3.18)). It is helpful to recall the asymptotic behavior for the Bessel function appearing in the integrand

$$K_1[x'] \simeq \begin{cases} \frac{1}{x'} & x' \ll 1 \\ \sqrt{\frac{\pi}{2x'}} e^{-x'} & x' \gg 1 \end{cases} \tag{3.20}$$

The physics behind the suppression at large x', namely at temperature much lower than the decaying particle mass, is clear: decaying particles are exponentially rare at temperatures below their mass, thus freeze-in production in this range of temperatures is negligible. As a result, in Fig. 3.2 the comoving yields are just horizontal lines at $x' \gg 1$: the integral in Eq. (3.18) is saturated around $x' \simeq 1$.

For all cases in Fig. 3.2 we also have $T_r \ll m_{B_1}$, thus freeze-in production happens entirely during the phase of ϕ-domination. If we additionally neglect the temperature variation for the number of relativistic degrees of freedom, namely we set $g_{*s}(x) = g_*(x) = \overline{g}_*$, we can rewrite Eq. (3.18) as follows

$$\begin{aligned} Y_\chi(x) \simeq \frac{g_{B_1}}{\overline{g}_*^{3/2}} \frac{135\sqrt{10}}{4\pi^5} \frac{\Gamma_{B_1 \to B_2 \chi} M_{\rm Pl}}{m_{B_1}^2 x_r^{n/2}} \times \\ \int_0^x dx' K_1[x'] \, x'^{\,(3+n/2)} \, , \end{aligned} \tag{3.21}$$

where we introduce $x_r = m_{B_1}/T_r$. The asymptotic value for the comoving density can be computed analytically. We write it as follows:

$$Y_\chi^\infty = Y_\chi^\infty \Big|_{\rm rad} \times \mathcal{F}_{\rm decay}(T_r, n) \, , \tag{3.22}$$

where we calculate the suppression factor $\mathcal{F}_{\rm decay}$ with respect to the result in a

pure radiation dominated early universe [45]

$$Y_\chi^\infty\Big|_{\rm rad} = \frac{g_{B_1}}{\bar{g}_*^{3/2}}\,\frac{405\sqrt{10}}{8\pi^4}\,\frac{\Gamma_{B_1\to B_2\chi}\,M_{\rm Pl}}{m_{B_1}^2}\ , \tag{3.23}$$

and we define the function accounting for the correction

$$\mathcal{F}_{\rm decay}(T_r,n) \equiv \frac{8}{3\pi}\left(\frac{2}{x_r}\right)^{n/2} \Gamma\left[\frac{6+n}{4}\right]\Gamma\left[\frac{10+n}{4}\right]\ . \tag{3.24}$$

Here, $\Gamma[x]$ is the Euler gamma function. This result is valid only for $n > 0$. Notice that we do not recover the radiation case result for $n = 0$: this is consistent with the expression for the energy density in Eq. (3.5) where setting $n = 0$ does not get rid of ϕ, but, rather, it adds a new species that red-shifts like radiation. From the explicit expression for $\mathcal{F}(n)$ we immediately see that the main source for the difference among the horizontal lines location in Fig. 3.2 is the factor $x_r^{n/2}$ in the denominator, since for the case we consider we have $x_r = 5 \times 10^4$.

The slope of the numerical solutions at $x \lesssim 1$ can also be derived analytically by taking the appropriate limit for the Bessel function (see Eq. (3.20)). We consider Eq. (3.21) in the $x \ll 1$ regime, where the integral is straightforward and we find

$$Y_\chi(x) \propto x^{(3+n/2)} \qquad\qquad (x \ll 1)\ . \tag{3.25}$$

The freeze-in solutions are steeper for larger n. The predicted asymptotic behavior is indeed what we find with our full numerical treatment in Fig. 3.3, where we take the same mass values for B_1 and X but this time we choose the coupling λ_d to reproduce the observed DM density. The steepness of the lines with larger n allows freeze-in process to start later and to be dominated at slightly lower temperatures.

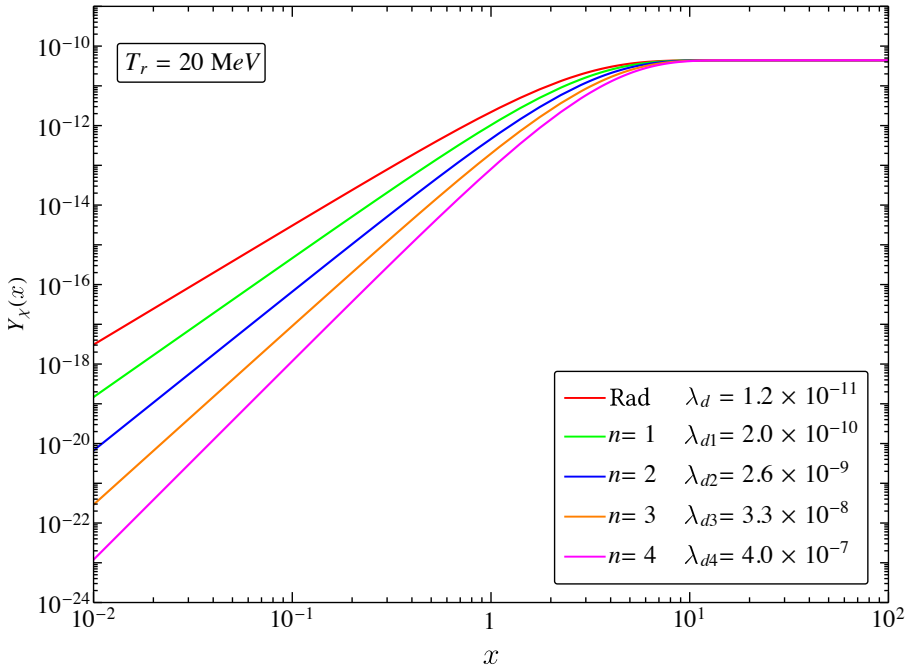

Figure 3.3: Numerical solution for the comoving number density Y_χ with $m_\chi = 10\,\text{GeV}$, $m_{B_1} = 1\,\text{TeV}$. Now λ_d is changed in order to reproduce the observed abundance ($\lambda_{d1} = 2.0 \times 10^{-10}$, $\lambda_{d2} = 2.6 \times 10^{-9}$, $\lambda_{d3} = 3.3 \times 10^{-8}$, $\lambda_{d4} = 4.0 \times 10^{-7}$). We set $T_r = 20\,\text{MeV}$ for all n.

3.3.2 Relic Density Suppression

Within the modified cosmological setup we consider in this work, DM is always under-produced with respect to the case of a standard history. We quantify by how much the relic density is suppressed in Fig. 3.4, where we keep the particle physics parameters fixed to the same values we used in the previous section. We calculate the DM relic density for each point in the (T_r, n) plane, and we take the ratio between the observed DM relic density in the radiation case and the relic density in our modified cosmological setup. In other words, we show iso-countours

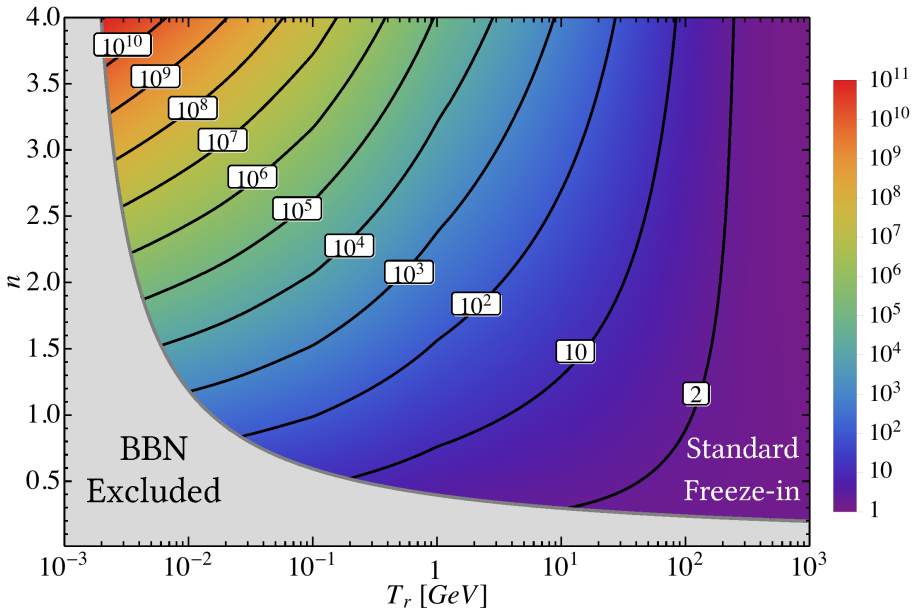

Figure 3.4: Contour plots of the reduction in the relic density in the case of Freeze-in by decay.

for the function

$$r_{\rm decay}(T_r, n) \equiv \frac{\Omega_\chi h^2|_{\rm rad}}{\Omega_\chi h^2} \ . \tag{3.26}$$

For T_r as large as m_{B_1}, the effect of the fast expanding universe phase is less important and we are back to a "standard" freeze-in scenario. For lower values of T_r, but still consistent with the BBN bound in Eq. (3.8), the factor can be as large as 10^{10}. For these low values of T_r we can approximate the result by using the semi-analytical solution found above

$$r_{\rm decay}(T_r, n) \simeq \mathcal{F}_{\rm decay}(T_r, n)^{-1} \qquad (T_r \ll m_{B_1}) \ . \tag{3.27}$$

One could turn the argument around, and state that stronger interactions are

needed to reproduce the observed DM density. The enhancement of the dimensionless coupling λ_d defined in Eq. (3.19) is easily obtained from Fig. 3.4, since the final relic density is always proportional to the decay width. We find the relation

$$\lambda_d(T_r, n) = r_{\rm decay}(T_r, n)^{1/2}\, \lambda_d^{\rm rad}\,, \tag{3.28}$$

with $\lambda_d^{\rm rad}$ the coupling for the case of a standard history. This enhancement to the couplings required to produce the right DM density today can thus be as large as 10^5 with modified fast-expanding thermal histories.

3.3.3 Displaced Events at Colliders

We conclude this Section by commenting on the consequences of the coupling constant enhancement required for successful freeze-in DM production in modified cosmological settings. Once we fix the mass of the particles, the requirement of reproducing the observed relic density fixes the decay width for each point in the (T_r, n) plane. The inverse decay width gives the scale for the decay length $\tau_{B_1} = \Gamma_{B_1}^{-1}$ if B_1 particles are produced at colliders. As we will see shortly, a typical prediction in the (T_r, n) plane is the observation of displaced B_1 decay vertices at particle colliders. This is opposed to the case of a standard cosmology, where the decay width is too large and for collider purposes B_1 is a stable particle [45]. Displaced events at collider are also typical is DM is produced via freeze-in during an early matter dominated era [23].

A convenient variable to express the observed DM density is the comoving energy density

$$\xi_\chi^{\rm obs} = \frac{m_\chi n_\chi}{s_0} = m_\chi Y_\chi = 0.44\,{\rm eV}\ , \tag{3.29}$$

with s_0 the current entropy density. We can find an approximate expression for

the expected decay length by taking the solution in Eq. (3.22) and compare it with the value above

$$\tau_{B_1} \simeq 3.4 \times 10^7 \, \mathcal{F}(T_r, n) \left(\frac{m_\chi}{10\,\mathrm{GeV}} \right) \left(\frac{1\,\mathrm{TeV}}{m_{B_1}} \right)^2 \mathrm{cm} \ , \tag{3.30}$$

where we also fixed $\overline{g}_* = 106.75$ (accounting for the full SM degrees of freedom). The scale 10^7 cm, way above the size of any detector, is typical for freeze-in during a radiation dominated era. However, as observed above, for the cosmologies we consider in this work we typically have $\mathcal{F}(T_r, n) \ll 1$, thus we can potentially get back to the detector size. We actually know how much we can reduce this decay length, since the inverse of $\mathcal{F}(T_r, n)$ is what is shown in Fig. 3.4. This suppression can be as large as 10^{10} and the decay length can get as small as 10^{-3} cm.

The parameter space for displaced decays is explored in Figs. 3.5 and 3.6. We start from Fig. 3.5, where we analyze the behavior of τ_{B_1} as we change the particle physics properties. The cosmological parameters (T_r, n) are fixed for each panel, and we show the contours for τ_{B_1} on the (m_χ, m_{B_1}) plane. The blue region corresponds to 10^2 cm $\leq \tau_{B_1} \leq 10^4$ cm, whereas the dark blue region corresponds to 10^{-2} cm $\leq \tau_{B_1} \leq 10^2$ cm. There are benchmarks for displaced signatures at colliders. The gray region in the bottom right corner is excluded by kinematics. We observe that isocontours follow the lines where $m_\chi \propto m_{B_1}^{2+n/2}$, consistently with the approximate solution given in Eq. (3.30).[1] Moreover, we see that the decay length is reduced by a factor of $\sim (T_r/m_{B_1})^{n/2}$ with respect to the radiation case. For example, if we take $m_\chi = 10\,\mathrm{GeV}$ and $m_{B_1} = 3\,\mathrm{TeV}$, the expected decay length for radiation case $\tau_{B_1} \sim 3 \times 10^6$cm. In our modified cosmological histories, the decay length expands into a range where its values vary from 10^{-2} cm to

[1] It is important to remember that there is a power of m_{B_1} in $\mathcal{F}(T_r, n)$ through x_r, since for each panel this time T_r is the fixed quantity, see the definition in Eq. (3.24).

10^4 cm. This range is accessible to present or future colliders.

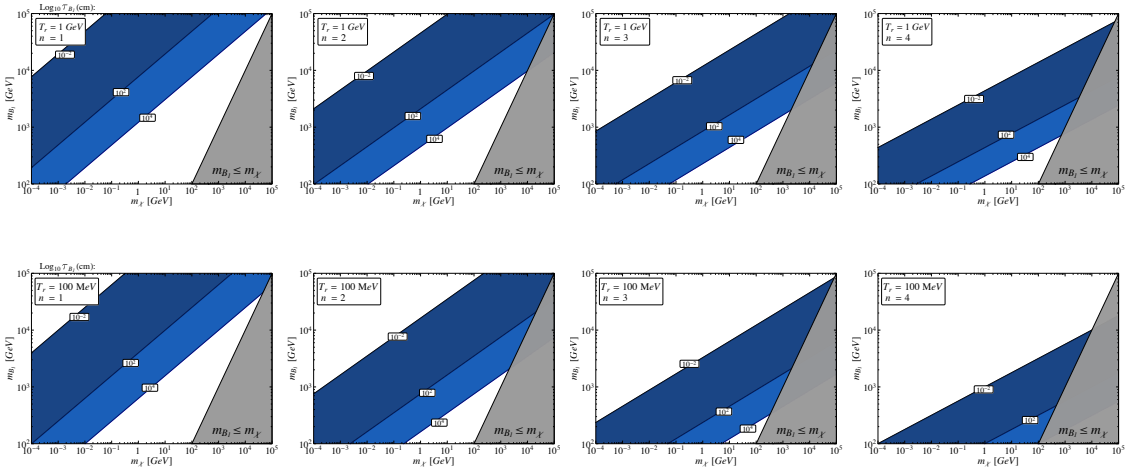

Figure 3.5: Contours of the B_1 decay length (in cm) on the (m_χ, m_{B_1}) plane corresponding to coupling values which produce the observed DM abundance, for different values of n and T_r. The blue region corresponds to $10^2\text{cm} \leq \tau_{B_1} \leq 10^4\text{cm}$ and the dark blue region corresponds to $10^{-2}\text{cm} \leq \tau_{B_1} \leq 10^2\text{cm}$. The first (second) row corresponds to $T_r = 1\,\text{GeV}$ ($T_r = 100\,\text{MeV}$) and the first (second, third and fourth) column corresponds to $n = 1$ ($n = 2$, 3 and 4).

In Fig. 3.6 we study the decay length τ_{B_1} as we change the cosmological parameters, offering a complementary view of our results. The value of m_{B_1} and m_χ are fixed now for each panel, and we show iso-contours for τ_{B_1} in the (n, T_r) plane. The bottom left corner grey area is the region excluded by BBN.

3.4 Freeze-In from Scattering

We now focus on models where DM is produced out of equilibrium via $2 \to 2$ scattering processes. As already explained in the Introduction, we divide the discussion into two classes of models, according to the number of DM particles produced for each reaction. We study the DM number density evolution for both scenarios, and we then discuss the implications for experimental searches.

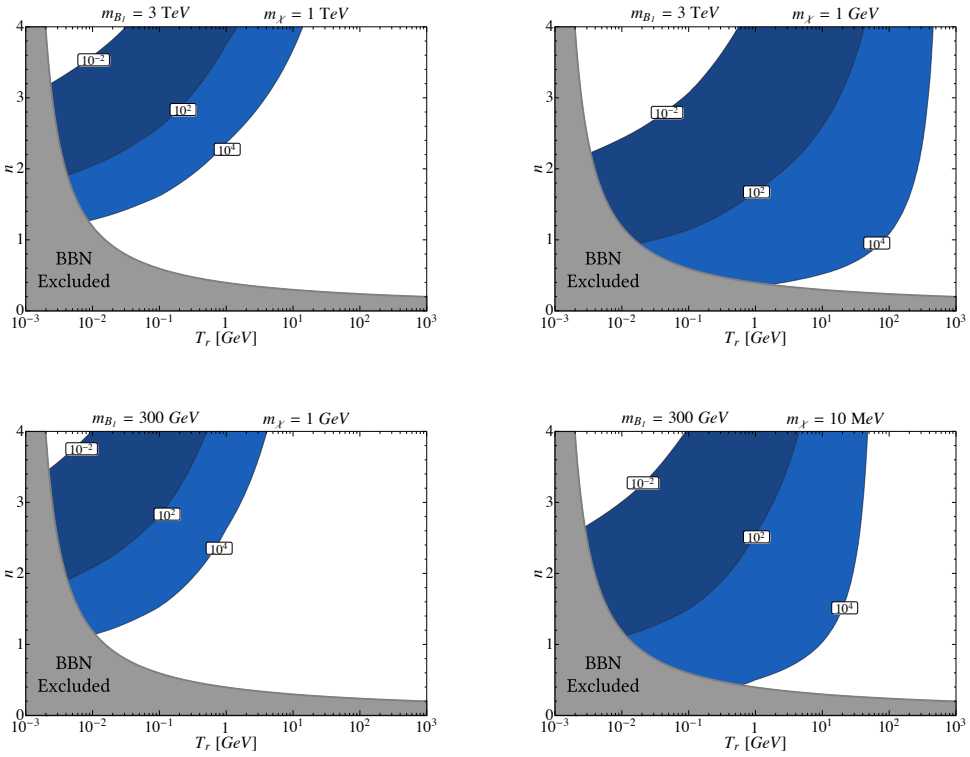

Figure 3.6: Contours of the B_1 decay length (in cm) on the (T_r, n) plane that reproduces the observed DM abundance for different values of m_{B_1} and m_χ. The blue region corresponds to $10^2\text{cm} \leq \tau_{B_1} \leq 10^4\text{cm}$ and the dark blue region corresponds to $10^{-2}\text{cm} \leq \tau_B \leq 10^2\text{cm}$. We fix $m_{B_1} = 3\,\text{TeV}$ and $m_{B_1} = 300\,\text{GeV}$ for the first and second row respectively and change m_χ accordingly.

3.4.1 DM Single Production

We start our analysis from models where DM particles are produced in the early universe via bath particle scattering of the form

$$B_1 B_2 \to B_3 \chi \ . \tag{3.31}$$

This is the leading production mechanism for several DM models. For example, the supersymmetric partner to the axion, the *axino*, in supersymmetric Peccei-Quinn theories, is a motivated DM candidate [57, 58, 59, 60, 61, 62] produced

via scattering as in Eq. (3.31). The bath particles producing the *axino* depend on the specific implementation of the PQ symmetry. For KSVZ theories [63, 64], the axino is produced via scattering of gluons and gluinos, whereas for DFSZ theories [65, 66] the processes can also be initiated by Higgs bosons and higgsinos.

The general collision operator for this class of models is derived in App B.1, where we find the two equivalent expressions in Eqs. (B.27) and (B.28). In our numerical analysis, we choose each time the most convenient one according to the mass spectrum of the theory (see the Appendix for details).

We observe that the process in Eq. (3.31) is not the only channel for DM production. The two reactions obtained by taking a permutation of the bath particles are allowed by crossing symmetry, and we must account for them as well. The way crossing symmetry is implemented depends on the specific model. Here, we study benchmark models where the matrix element is left unchanged under crossing symmetry. Moreover, we assume that the matrix element for this process is independent on the kinematics. We parameterize the squared matrix elements as follows [2]

$$\begin{aligned} \lambda_{B\chi}^2 = |\mathcal{M}_{B_1 B_2 \to B_3 \chi}|^2 = \\ |\mathcal{M}_{B_2 B_3 \to B_1 \chi}|^2 = |\mathcal{M}_{B_1 B_3 \to B_2 \chi}|^2 \ . \end{aligned} \tag{3.32}$$

For models satisfying these assumptions, the collision operator takes the simple form in Eq. (B.42), which we report here in the final form

$$\begin{aligned} \mathcal{C}_{B_i B_j \to B_k \chi} = \frac{\lambda_{B\chi}^2 T}{512\pi^5} \int_{s_{\rm single}^{\rm min}}^{\infty} \frac{ds}{s^{3/2}} K_1[\sqrt{s}/T] \times \\ \lambda^{1/2}(s, m_{B_i}, m_{B_j}) \, \lambda^{1/2}(s, m_{B_k}, m_\chi) \ , \end{aligned} \tag{3.33}$$

[2]Notice that this happens exactly, for example, when the particles involved in the reaction are scalar fields and the interaction is of the type $\mathcal{L} = \lambda_{B\chi} B_1 B_2 B_3 \chi$.

where the function $\lambda(x, y, z)$ is defined in Eq. (B.14) and the lower integration limit is set by the kinematical threshold for the reaction

$$s_{\rm single}^{\rm min} = \max\left\{(m_{B_i} + m_{B_j})^2, (m_{B_k} + m_\chi)^2\right\} \ . \tag{3.34}$$

We analyze the number density evolution for the class of models introduced above. We fix the masses to be $(m_{B_3}, m_\chi) = (1000, 10)\,\text{GeV}$, whereas bath particles B_1 and B_2 have negligible masses. As an example, this is the case where χ is the axino, B_3 is the gluino and $B_{1,2}$ are gluons. For this choice of the parameters, the observed DM abundance is reproduced for the standard cosmology if we choose $\lambda_{B\chi}^{rad} = 1.5 \times 10^{10}$.

Numerical results for the number density evolution are shown in Fig. 3.7, where we set $T_r = 20\,\text{MeV}$ and we consider a few different values of n as indicated in the caption. We plot the solution as a function of the "time variable" $x = m_{B_3}/T$. The behavior is similar to the one already seen for freeze-in via decays: the asymptotic comoving density decreases as we increase the value of the index n. The net effect is that DM is underproduced, which in turn requires larger cross sections to reproduce the observed DM abundance. The asymptotic number density is reached for $x \simeq 4$, or equivalently for temperatures $T \simeq m_{B_3}/4$. This is not surprising, since B_3 is the heaviest particle involved in the reaction. In order to produce a DM particle, we either need a B_3 particle in the initial state or enough kinetic energy to produce B_3 in the final state. At the temperature drops below m_{B_3}, these processes become exponentially rare.

As in the decays of freeze-in via decays, the behavior of the numerical solutions can be reproduced analytically. In order to do so, we only keep the finite mass of B_3. This is well justified for the spectrum under consideration: $m_{B_3} = 100 m_\chi$, whereas B_1 and B_2 are massless. Once we make this approximation, the collision

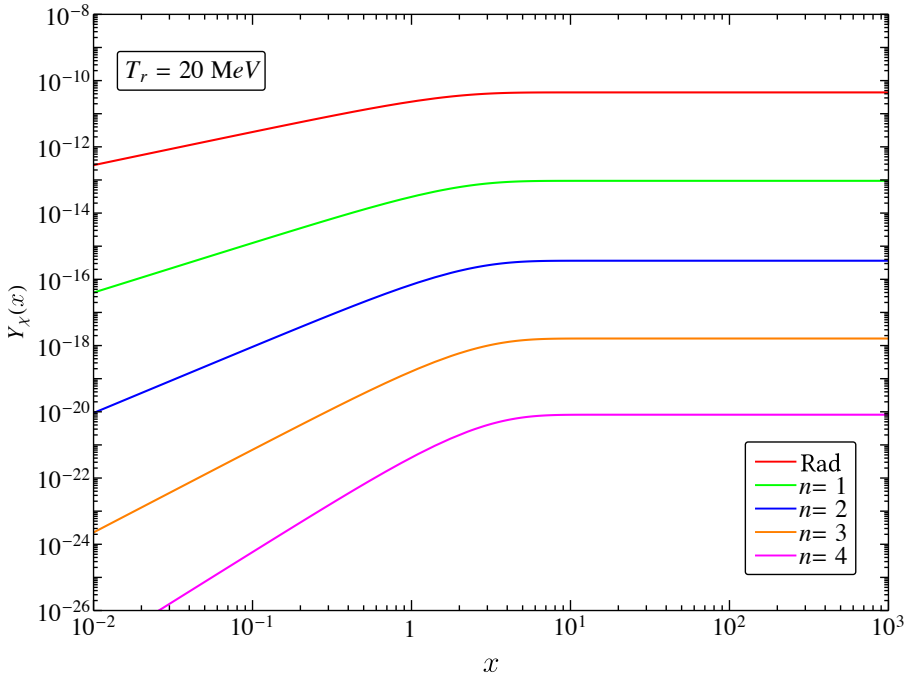

Figure 3.7: Numerical solutions for the comoving number density Y_χ as a function of $x = m_{B_3}/T$. We choose $m_{B_3} = 1$ TeV, $m_\chi = 10$ GeV and $\lambda_{B\chi} = 1.5\times10^{-10}$. We consider different values for n, whereas we always set $T_r = 20\,\text{MeV}$.

operator in Eq. (3.33) simply reads

$$\mathcal{C}_{B_iB_j\to B_k\chi} = \frac{\lambda_{B\chi}^2\, T}{512\pi^5}\int_{m_{B_3}^2}^{\infty} ds\,\frac{s-m_{B_3}^2}{s^{1/2}}K_1[\sqrt{s}/T] = \frac{\lambda_{B\chi}^2\, m_{B_3}^4}{128\pi^5}\,\frac{K_1[x]}{x^3}\,, \tag{3.35}$$

where we remind the Reader that $x = m_{B_3}/T$. This result is valid for any permutation of the bath particles, thus the total collision operator is obtained by multiplying the above result by a factor of three.

The freeze-in yield is obtained from the general result in Eq. (3.14). Upon neglecting as usual the temperature variation of g_*, we find the approximate so-

lution

$$Y_\chi(x) \simeq \frac{\lambda_{B\chi}^2}{\overline{g}_*^{3/2}} \frac{405\sqrt{10}}{256\pi^8} \frac{M_{\rm Pl}}{m_{B_3} x_r^{n/2}} \int_0^x dx' K_1[x']\, x'^{(1+n/2)} \ , \tag{3.36}$$

where, in this case, $x_r \approx m_{B_3}/T_r$. Considering early times, $x \ll 1$, we can Taylor-expand the Bessel function and calculate the slope of the lines in Fig. 3.7

$$Y_\chi(x) \propto x^{(1+n/2)} \qquad\qquad (x \ll 1) \ . \tag{3.37}$$

This scaling is different from the result we found for decays in Eq. (3.25). Consistently, the slopes of the curves in Fig. 3.2 and Fig. 3.7 are different.

The asymptotic value for the yield can be computed by evaluating the approximate solution in Eq. (3.36) for $x \to \infty$. As done before, it is convenient to normalize our solution with respect to the result in a radiation-dominated "standard" early universe

$$Y_\chi^\infty\Big|_{\rm rad} = \frac{\lambda_{B_3\chi}^2}{\overline{g}_*^{3/2}} \frac{405\sqrt{10}}{512\pi^7} \frac{M_{\rm Pl}}{m_{B_3}} \ . \tag{3.38}$$

We express the asymptotic value as it follows

$$Y_\chi^\infty = Y_\chi^\infty\Big|_{\rm rad} \times \mathcal{F}_{\rm scatt}^{B\chi}(T_r, n) \ , \tag{3.39}$$

where we define the function

$$\mathcal{F}_{\rm scatt}^{B\chi} \equiv \frac{2}{\pi} \left(\frac{2}{x_r}\right)^{n/2} \Gamma\left[\frac{2+n}{4}\right] \Gamma\left[\frac{6+n}{4}\right] \ . \tag{3.40}$$

In Fig. 3.8, we use the same mass and T_r values, but we choose this time $\lambda_{B_3\chi}$ to reproduce the observed DM abundance for each n. The enhancement in the matrix element can be as large as $\sim 10^5$. Such enhancements for the couplings translate into a quadratically larger effect in the cross sections for potential DM detection processes, which can be enhanced by a factor of 10^{10}.

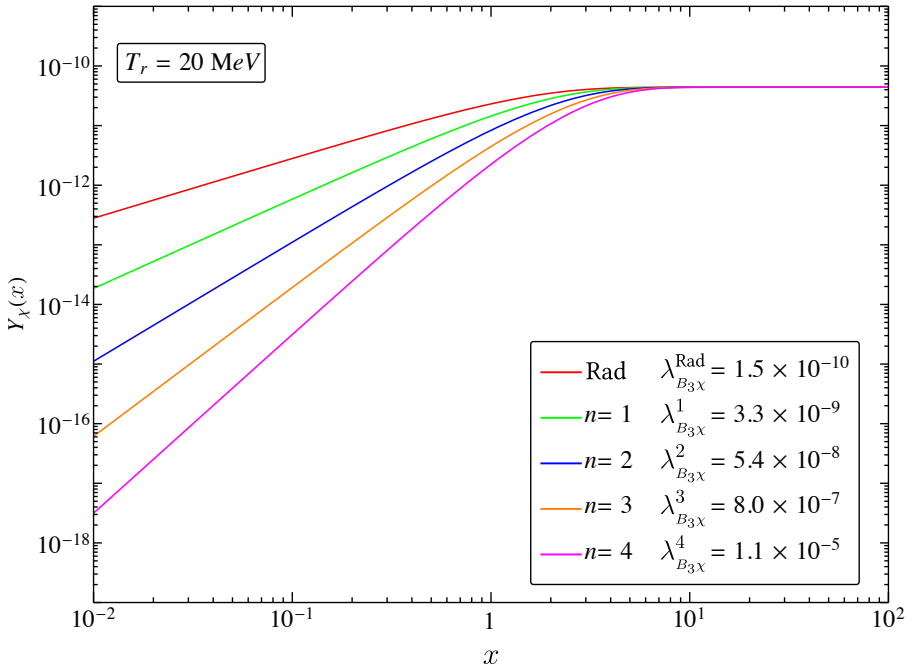

Figure 3.8: Numerical solution for the comoving number density Y_χ with $m_{B_3} = 1\,\text{TeV}$ and $m_\chi = 10\,\text{GeV}$. Now $\lambda_{B_3\chi}$ is changed in order to reproduce the observed abundance ($\lambda^1_{B_3\chi} = 3.3 \times 10^{-9}$, $\lambda^2_{B_3\chi} = 5.4 \times 10^{-8}$, $\lambda^3_{B_3\chi} = 8.0 \times 10^{-7}$, $\lambda^4_{B_3\chi} = 1.1 \times 10^{-5}$). We set $T_r = 20\,\text{MeV}$ for all n.

For freeze-in via scattering $B_1 B_2 \to B_3\chi$, the DM relic abundance is always suppressed in the (T_r, n) plane. We quantify this suppression in Fig. 3.9, where we keep the same mass values for B_3 and χ. More specifically, we show iso-contours of the function

$$r_{B\chi}(T_r, n) \equiv \frac{\Omega_\chi h^2|_{\rm rad}}{\Omega_\chi h^2} \ . \tag{3.41}$$

The suppression factor can be analytically understood by using the equations derived above

$$r_{B\chi}(T_r, n) \simeq \mathcal{F}^{B\chi}_{\rm scatt}(T_r, n)^{-1} \simeq \left(\frac{x_r}{2}\right)^{n/2} \ . \tag{3.42}$$

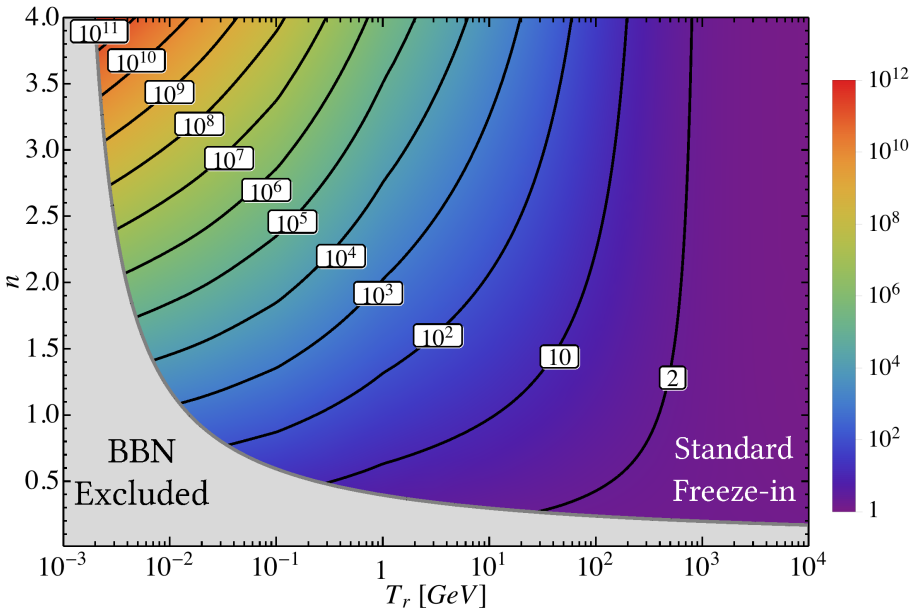

Figure 3.9: Reduction in the relic density in the case of Freeze-in by scattering $B_1 B_2 \to B_3 \chi$ for $m_{B_3} = 1\,\text{TeV}$ and $m_\chi = 10\,\text{GeV}$ compare with the observed DM density in the standard case (radiation)

The associated enhancement in the required matrix element $\lambda_{B_3\chi}$ reads

$$\lambda_{B\chi}(T_r, n) = r_{B\chi}(T_r, n)^{1/2}\, \lambda_{B\chi}^{\text{rad}}\ , \tag{3.43}$$

indicating that increasing n and/or decreasing T_r leads to larger values for the necessary coupling constant to reproduce the observed DM density of the universe.

3.4.2 DM Pair Production

We consider in this section the third and final freeze-in case: DM pair production

$$B_1 B_2 \to \chi\chi\ . \tag{3.44}$$

This process is the leading production mechanism for all models where the DM particle belongs to a dark sector very weakly coupled to the visible sector. Notable examples include Higgs portal models with small mixing angle and dark photon models with small kinetic mixing.

General results for this case are also given in App B.1, where the two equivalent forms are in Eqs. (B.34) and (B.35). We focus also for this case on models where the matrix element is a constant

$$\lambda_{\chi\chi}^2 = |\mathcal{M}_{B_1 B_2 \to \chi\chi}|^2 \ . \tag{3.45}$$

The collision operator then takes the simple form in Eq. (B.43). We write it here in the final form

$$\begin{aligned} \mathcal{C}_{B_1 B_2 \to \chi\chi} = & \frac{\lambda_{\chi\chi}^2 \, T}{512\pi^5} \int_{s_{\rm pair}^{\rm min}}^{\infty} \frac{ds}{s^{3/2}} \, K_1[\sqrt{s}/T] \times \\ & \lambda^{1/2}(s, m_{B_1}, m_{B_2}) \, \lambda^{1/2}(s, m_\chi, m_\chi) \ , \end{aligned} \tag{3.46}$$

with $\lambda(x, y, z)$ defined in Eq. (B.14) and the lower integration limit set by kinematics

$$s_{\rm pair}^{\rm min} = \max\left\{(m_{B_1} + m_{B_2})^2, (2m_\chi)^2\right\} \ . \tag{3.47}$$

Numerical results for the comoving yield are presented in Fig. 3.10. We choose $m_\chi = 100\,\text{GeV}$, we neglect the bath particle masses and we set $\lambda_{\chi\chi} = \lambda_{\chi\chi}^{\rm rad} = 3.41 \times 10^{-11}$. This is the value that reproduces the correct abundance for a standard cosmological history. We plot the comoving number density as a function of the "time variable" $x = m_\chi/T$. The freeze-in abundance is largely suppressed compared to the standard case also for DM pair production, forcing markedly larger couplings to explain the observed abundance. Quantitatively, this is illustrated in Fig. 3.11, where we keep m_χ and T_r fixed and we set the couplings $\lambda_{\chi\chi}^n$

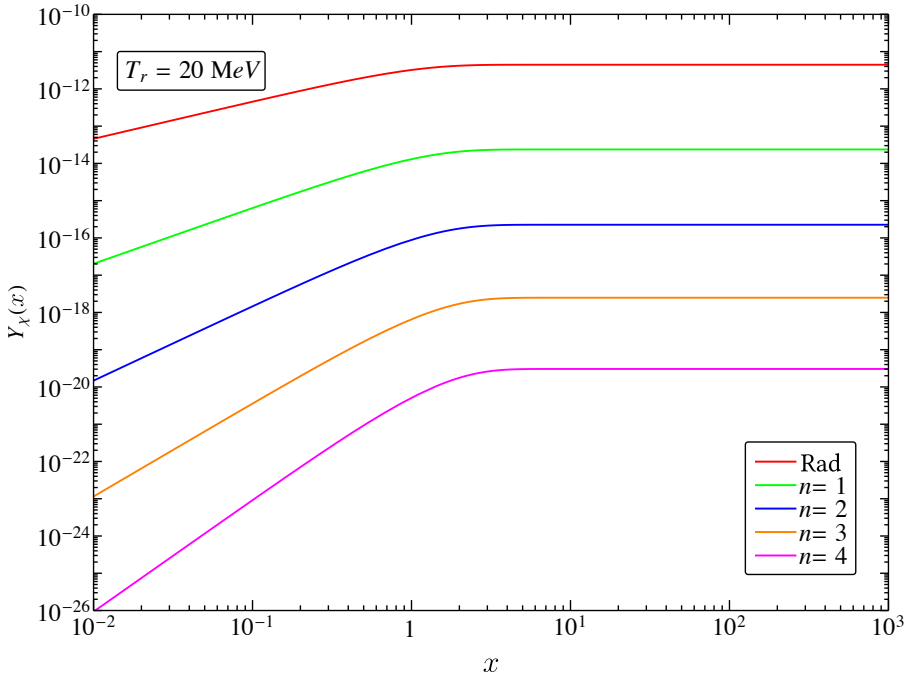

Figure 3.10: Numerical solution for the comoving number density Y_χ with $m_\chi = 100\,\text{GeV}$ and $\lambda_{\chi\chi} = 3.41 \times 10^{-11}$ in the case of Freeze-in by scattering $B_1 B_2 \to \chi\chi$. We set $T_r = 20\,\text{MeV}$ for all n.

needed for a modified cosmology featuring a given $n > 0$. The figure shows how the needed couplings are larger than in the standard case by up to more than four orders of magnitude, for large $n \sim 4$.

The analytical estimates are analogous to the previous case, and we therefore only quote the final results here. First, the collision operator neglecting the bath particles mass reads

$$\mathcal{C}_{B_1 B_2 \to \chi\chi} = \frac{\lambda_{\chi\chi}^2\, m_\chi^4}{128\pi^5}\, \frac{K_1[x]^2}{x^2} \ . \tag{3.48}$$

The comoving density as a function of the temperature is obtained by computing

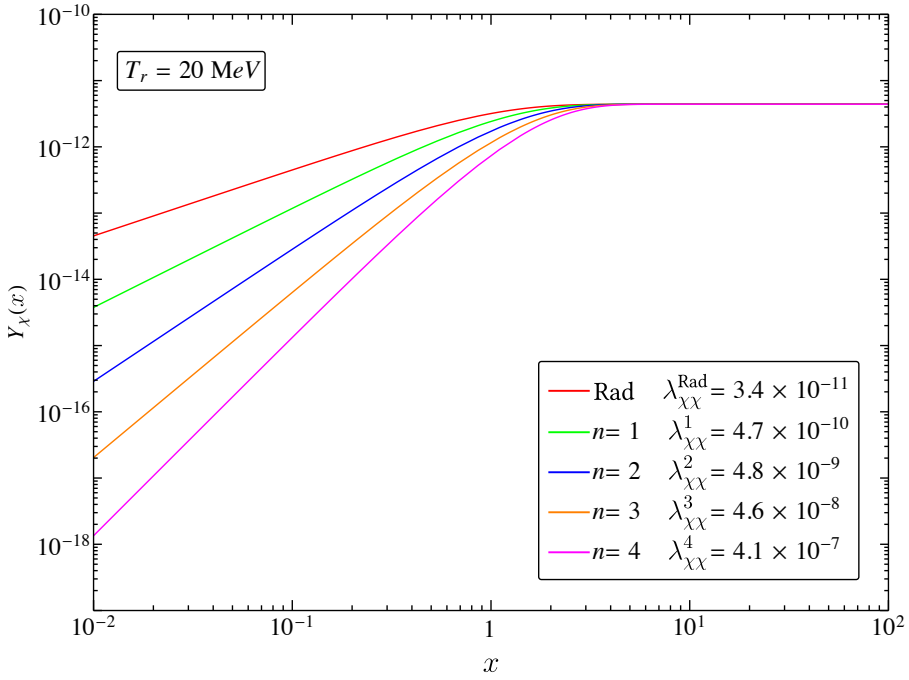

Figure 3.11: Numerical solution for the comoving number density Y_χ with $m_\chi = 100\,\text{GeV}$. Now $\lambda_{\chi\chi}$ is changed in order to reproduce the observed abundance ($\lambda^1_{\chi\chi} = 4.7 \times 10^{-10}$, $\lambda^2_{\chi\chi} = 4.8 \times 10^{-9}$, $\lambda^3_{\chi\chi} = 4.6 \times 10^{-8}$, $\lambda^4_{\chi\chi} = 4.1 \times 10^{-7}$). We set $T_r = 20\,\text{MeV}$ for all n.

the integral

$$Y_\chi(x) \simeq \frac{\lambda_{\chi\chi}^2}{\bar{g}_*^{3/2}} \frac{135\sqrt{10}}{256\pi^8} \frac{M_{\rm Pl}}{m_\chi x_r^{n/2}} \times \int_0^x dx' K_1[x']^2\, x'^{(2+n/2)} \,. \tag{3.49}$$

The slope of the different curves is the same as the one found for single DM production (see Eq. (3.37)).

We normalize again the asymptotic value with respect to the radiation case

$$Y_\chi^\infty = Y_\chi^\infty\big|_{\rm rad} \times \mathcal{F}_{\rm scatt}^{\chi\chi} \,, \tag{3.50}$$

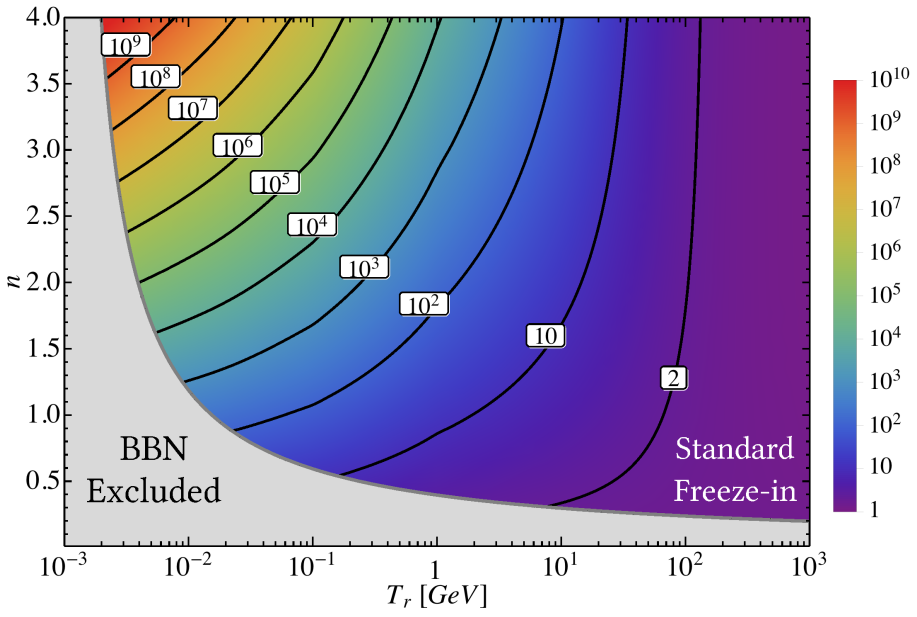

Figure 3.12: Relic density suppression in the case of freeze-in by scattering $B_1 B_2 \to \chi\chi$, compared with the observed DM density in the standard case (radiation)

which in this case it reads

$$Y_\chi^\infty\Big|_{\rm rad} = \frac{\lambda_{\chi\chi}^2}{\overline{g}_*^{3/2}} \frac{405\sqrt{10}}{8192\pi^6} \frac{M_{\rm Pl}}{m_\chi} \,. \tag{3.51}$$

The suppression we find in this case reads

$$\mathcal{F}_{\rm scatt}^{\chi\chi} \equiv \frac{8}{3\sqrt{\pi}} \frac{\Gamma\left[\frac{2+n}{4}\right]\Gamma\left[\frac{6+n}{4}\right]\Gamma\left[\frac{10+n}{4}\right]}{x_r^{n/2}\Gamma\left[\frac{8+n}{4}\right]} \,. \tag{3.52}$$

We quantify the DM relic abundance suppression $r_{\chi\chi}$ in the (T_r, n) plane in Fig. 3.12 for the same values of the DM particle mass. Also in this case, suppression factors can be as large as ten orders of magnitude.

3.4.3 Implications for Dark Matter Detection

Our general finding is that when the universe is dominated, at the time of DM production through freeze-in, by a species that produces a larger Hubble rate a given temperature than in the radiation-dominated case (what we dub a "fast-expanding" universe), the couplings needed to produce the observed DM abundance are *larger* than in a radiation-dominated, standard scenario. As a result, quite generically, DM detection prospects improve.

Besides the general conclusion above, it is however hard to solidly quantify how DM detection prospects are affected in a general, model-independent way for freeze-in via scattering in modified, fast-expanding cosmologies. A first difficulty stems from the impossibility of performing a cross-symmetry prediction for, e.g., the cross section for the $B_1 B_2 \to \chi\chi$ process versus the cross-symmetric $\chi B_1 \to \chi B_2$ process (and similarly for the single-production scattering case).

With that caveat in mind, however, for simple instances where for example the matrix element squared is a constant, as we considered above, we can attempt to draw a few general statements. Let us consider first the DM single-production case, $B_1 B_2 \to B_3 \chi$. In this case, let us assume that for instance B_3 is some visible-sector species which is abundant in the late universe, for instance an electron or a photon. As long as the inverse reaction to the process leading to freeze-in χ production is kinematically allowed for non-relativistic processes, i.e., approximately,

$$m_\chi + m_{B_3} > m_{B_1} + m_{B_2} \equiv m_{12} \ , \tag{3.53}$$

and as long as χ's stability is not jeopardized by decays to $B_1 + B_2 + B_3$, i.e.

$$m_\chi - m_{B_3} < m_{12} \ , \tag{3.54}$$

then, the reaction

$$B_3\chi \to B_1 B_2 \tag{3.55}$$

would be generically allowed, leading to potential completely novel indirect detection signals, involving a *single* DM particle in the initial state. Rates for this type of reaction are much larger in the fast-expanding universes we entertain here. If B_3 is a particle species abundant in direct detection targets, the reaction $B_3\chi \to B_1 B_2$ would also possibly produce striking signals at direct detection experiments.

In the case of DM pair production, $B_1 B_2 \to \chi\chi$, and again assuming a simple form for the matrix element squared, modified cosmologies would give a strikingly large enhancement to late-time DM pair annihilation rates, $\chi\chi \to B_1 B_2$. The relevant pair-annihilation cross sections, however, would presumably be quite small, unless $m_\chi \ll\sim$ GeV, since one would naively estimate, given what we find above,

$$\sigma_{\chi\chi\to B_1 B_2} \sim \frac{\lambda_{\chi\chi}^2}{m_\chi^2} \gtrsim 10^{-13}\ \mathrm{GeV}^{-2} \left(\frac{\mathrm{GeV}}{m_\chi}\right)^2, \tag{3.56}$$

while indirect detection is usually sensitive to pair-annihilation cross sections on the order of 10^{-10} GeV^{-2}. Strong constraints from annihilation effects on the CMB would however apply in the case of light dark matter masses.

The cross-symmetric process, $\chi B_1 \to \chi B_2$, is instead rather promising, as the implied rates (which again, in general do depend on the underlying model) might be large enough to be of interest for direct detection, provided a modified cosmology affects DM freeze-in pair production.

We postpone a more general and comprehensive analysis of implications of a modified cosmology with a fast-expanding universe at DM freeze-in, including the discussion of specific models, to future studies.

3.5 Discussion and Conclusions

The cosmological history of the universe is observationally and quantitatively tested only up to temperature of around 1 MeV: at larger temperatures, it is customary to *assume* a radiation dominated universe, which is thus the canvas on which pictures for dark matter production in the early universe are usually drawn. However, cosmological histories where at a given temperature the expansion rate, and thus the Hubble rate, was much larger are possible, and yield dramatic consequences for the prediction of the amount of dark matter produced in the early universe by thermal or non-thermal processes.

Here, we focused on the case of dark matter production via *freeze-in*: the dark matter is "dumped" by a decay or scattering process in the early universe, and never reaches thermal equilibrium. As is well known, given a certain cosmological history, and similarly to the case of thermal freeze-out, it is possible to compute the relic dark matter yield for freeze-in from a few particle physics input parameter characterizing the dark matter sector. Also in analogy to what we recently pointed out for the case of freeze-out in Ref. [49], in the presence of a modified cosmological history at temperatures above Big Bang nucleosynthesis, such relic dark matter yield can be profoundly affected, and the ensuing phenomenological and observational consequences for a given dark matter particle setup drastically changed.

To outline a simple yet comprehensive picture of the effects of a rapidly expanding pre-BBN universe, here we parameterized the additional energy density responsible for the modified expansion history with only two parameters, T_r and n, effective describing the normalization and the power-law temperature/redshift dependence of the extra species (concrete models for the cosmological history might feature a more complicated functional dependence for the energy density

and thus the Hubble rate, see e.g. the recent Ref. [50], but the resulting effects fall within the range of parameters we study here).

For each of the three cases, we illustrated the freeze-in production suppression, for various values of the parameters defining the cosmological background; We derived analytical expressions that accurately capture and illustrate our numerical results; We then specialized our analysis to simplified expressions for the decay or scattering rates, translating the freeze-in production suppression in the enhancement needed in the relevant particle coupling; Finally, for each of the three cases, we scanned the parameter space of background modified cosmologies, and calculated for each parameter space point the resulting freeze-in production suppression.

Our results are remarkable first for their generality: we demonstrated that in a fast-expanding universe, freeze-in dark matter production is systematically, and dramatically suppressed. Secondly, our results quantify such suppression, which, we find, can be as large as ten orders of magnitude in some cases. Thirdly, and perhaps most importantly, our work outlines the range of potential implications for collider studies and for direct and indirect dark matter detection, which can drastically affect detection strategies for entire classes of particle dark matter candidates.

Chapter 4

Primordial Black Holes and Effective Spin Measurements with LIGO-Virgo

4.1 Introduction

After the detection of binary black hole (BBH) merger events with LIGO-Virgo [67, 4], the question of the *physical origin* of the black holes has become somewhat pressing. In particular, there has been some significant interest in the possibility that some or all of the BBH events originate from *primordial* black holes (PBH) [68], i.e., black holes originating from large over-densities in the very early universe rather than from the collapse of stellar objects (see e.g. [69]). Interestingly, this interpretation is compatible with the notion that these PBH could be the *dark matter* needed for a consistent picture of the early and large-scale structure of the universe (see e.g. [68]). Whether or not this possibility is ruled out is the focus of intense debate, the key issues at stake including (1) the problem of matter

accretion that might produce significant-enough accelerated charged particles to perturb in a measurable, and excessive way the cosmic microwave background photons [70, 71] (see however [72]); (2) the problem of disruption of small-scale structure by the relatively massive black holes that would make up the dark matter [73, 74] (see however [75]); and (3) limits from gravitational lensing of type Ia supernovae [76] (see however [77]).

These constraints notwithstanding, it is known (and it is reviewed below) that PBH that were produced during a radiation-dominated cosmological epoch have low intrinsic spin magnitude. As a result, a generic prediction of the picture where the LIGO-Virgo BBH events are in part or all PBH mergers is that the effective spin parameter (to be defined below, and which depends among other things on the intrinsic black hole spin magnitudes) is very low. Incidentally, it is important to point out that this fact (that binary mergers of PBH should have a low effective spin parameter) does depend on cosmology: it has been shown, for instance, that if the universe went through a matter-domination phase during PBH formation, then in fact the intrinsic spin of the resulting PBHs is generically *close to maximal* [78]. Furthermore, other possibilities might arise for cosmologies where the early universe was neither matter- nor radiation-dominated at early times, as we explored recently [49, 79]. With this caveat in mind, we shall hereafter assume radiation domination at the time of PBH formation.

The key motivation for the present study is that, so far, 9 out of 10 of the LIGO-Virgo BBH mergers are compatible with very low effective spin parameters. It seems timely, therefore, to assess what the *predicted* probability density for PBH's effective spin parameter is, and to compare it with current observations; additionally, we intend to explore *how many events* it will take to differentiate in a statistically robust fashion different effective spin parameter models. Although

at present there is no firm prediction for astrophysical black holes' effective spin parameter, and there is debate concerning selection and bias effects in the detected BBH events, our study intends to point out that (i) current observations of the effective spin parameter are largely compatible with a dominant PBH component in the BBH mergers, and that (ii) in the future, the effective spin parameter distribution could help discriminating PBH from "ordinary", astrophysical black holes.

Aspects of the question we address here have been considered in the recent literature, with different assumptions and methods. Soon after the detection of the first four BBH mergers [67, 80, 81, 82, 83], Ref. [84] argued that information on the effective spin could be used to distinguish between aligned versus isotropic angular distributions; specifically, [84] concluded that as long as the black hole spin values are not intrinsically small (which, however, might well be a distinct possibility, as pointed out e.g. by Ref. [85]) then an aligned angular distribution is strongly disfavored. Additionally, Ref. [84] also showed how with relatively few additional events, the odds ratio would conclusively point in one direction or another (i.e., isotropic or aligned).

Ref. [86] reiterated how scenarios considered in the formation of astrophysical black hole binaries naturally lead to isotropic (for dynamical capture) or near-aligned (for common envelope evolution) black hole spins. They also showed that Bayesian statistics allows one to distinguish, at a given confidence level, which *fraction* of the binaries are preferentially aligned versus isotropically distributed. A similar analysis was conducted in Ref. [87], with the additional points that a discrimination between isotropic and aligned spin distributions might be possible even regardless of the intrinsic spin magnitude distribution. They also showed that once an aligned or isotropic spin distribution is established, it is possible

to re-construct the spin magnitude distribution with a high degree of confidence. The possibility of disentangling the existence of sub-populations of binary black holes with different spin orientations was explored in Ref. [88], which also pointed out how a "pure" distribution would be statistically preferred with relatively few events (see also Ref. [89]).

In this study, we utilize the intrinsic spin distribution of PBHs from the results of Ref. [90] to calculate (to our knowledge for the first time) the predicted prior probability distribution for the effective spin parameter. Ref. [90] assumes that there is no correlation between the overdensity leading to the formation of the PBH and its spin, and that the probability density for the spin distribution as a function of the overdensity is flat. A recent study, Ref. [3], challenges these assumptions, and finds a peaked distribution for the PBH spin parameter, which critically depends on the width of the power spectrum peak giving rise to the PBH, and on the relative abundance of PBH. As a result, the spin distribution is significantly narrower than what was predicted in Ref. [90]. In what follows, we compare the resulting spin distribution for a variety of assumptions for PBH formation as outlined in Ref. [3], and compare it to our benchmark choice which reflects the results of Ref. [90] (and which, as we explain below, can be seen as a limiting case of the setup of Ref. [3]).

To these ends, in this study we first explore, in sec. 4.2, the theoretical prediction for the effective spin parameter distribution for PBH. We outline the assumed astrophysical black holes spin magnitude distribution we consider, and we review LIGO-Virgo observations; in sec. 4.3 we compare the odds ratios for the models we consider and study the favored "mixture" of different such models; we then forecast how future events will inform both the odds ratios and the inference of the relative level of mixing of different models. Finally, in sec. 4.4 we discuss our

results and present our conclusions.

4.2 Effective Spin Distribution

The spin magnitude of a Kerr black hole (BH) is commonly defined via a dimensionless spin parameter χ,

$$\chi = \frac{|\vec{S}|}{Gm^2}, \tag{4.1}$$

where $\vec{S}$ and m are the spin and mass of the BH, respectively. One of the most important parameters that LIGO can infer from the gravitational waveform is the *effective spin parameter* χ_{eff}, defined as:

$$\chi_{\text{eff}} = \frac{m_1\chi_1 \cos\theta_1 + m_2\chi_2 \cos\theta_2}{m_1 + m_2}, \tag{4.2}$$

where $\theta_i = \cos^{-1}(\vec{L} \cdot \vec{S_i})$ is the tilt angle between the spin $\vec{S_i}$ and the orbital angular momentum vector $\vec{L}$. As apparent from its definition, the parameter χ_{eff} is a quantity sensitive to both the spin alignment of the two black holes with their orbit (angular momentum of the binary) before the merger, and to the magnitude of the individual spins. χ_{eff} is a dimensionless number ranging from -1 to 1, where for $\chi_{\text{eff}} = 1$ the spins of both black holes are perfectly aligned with their orbit, and $\chi_{\text{eff}} = -1$ the spins are perfectly anti-aligned. Values of $\chi_{\text{eff}} \approx 0$ can stem from one or both of the following physical situations: (i) the black hole intrinsic spins are anti-aligned with each other, or (ii) the magnitude of the intrinsic effective spin parameters, $\chi_i \ll 1$. There could be a third possibility, that both spins are perpendicular to the orbit, but this is somewhat less likely and less physically motivated.

First, let us gain some intuition about the effective spin distribution for a few binary black hole (BBH) formation channels. One possible formation channel for BBH is from massive isolated binaries through common envelope evolution, where the intrinsic spin is generally aligned along the same direction as the orbital angular momentum, meaning that $\chi_{\rm eff} \approx 1$. On the other hand, there exist dynamical scenarios where we expect most BBHs to have spins largely uncorrelated with their orbit meaning that $\chi_{\rm eff} \approx 0$. This is the case, for instance, for BBHs formed dynamically in dense stellar environments, and it is also the case for PBHs, which additionally are predicted to have small intrinsic spins. It is important to notice that a key consequence, and possible signature, of any isotropic formation mechanism is that the distribution of $\chi_{\rm eff}$ is *symmetric around zero*, regardless of the spin magnitude distribution [87].

4.2.1 LIGO-Virgo effective spin measurements

Event	$m_1[\mathrm{M}_\odot]$	$m_2\,[\mathrm{M}_\odot]$	$\chi_{\rm eff}$
GW150914	$35.6^{+4.8}_{-3.0}$	$30.6^{+3.0}_{-4.4}$	$-0.01^{+0.12}_{-0.13}$
GW151012	$23.3^{+14.0}_{-5.5}$	$13.6^{+4.1}_{-4.8}$	$0.04^{+0.28}_{-0.19}$
GW151226	$13.7^{+8.8}_{-3.2}$	$7.7^{+2.2}_{-2.6}$	$0.18^{+0.20}_{-0.12}$
GW170104	$31.0^{+7.2}_{-5.6}$	$20.1^{+4.9}_{-4.5}$	$-0.04^{+0.17}_{-0.20}$
GW170608	$10.9^{+5.3}_{-1.7}$	$7.6^{+1.3}_{-2.1}$	$0.03^{+0.19}_{-0.07}$
GW170729	$50.6^{+16.6}_{-10.2}$	$34.3^{+9.1}_{-10.1}$	$0.36^{+0.21}_{-0.25}$
GW170809	$35.2^{+8.3}_{-6.0}$	$23.8^{+5.2}_{-5.1}$	$0.07^{+0.16}_{-0.16}$
GW170814	$30.7^{+5.7}_{-3.0}$	$25.3^{+2.9}_{-4.1}$	$0.07^{+0.12}_{-0.11}$
GW170818	$35.5^{+7.5}_{-4.7}$	$26.8^{+4.3}_{-5.2}$	$-0.09^{+0.18}_{-0.21}$
GW170823	$39.6^{+10.0}_{-6.6}$	$29.4^{+6.3}_{-7.1}$	$0.08^{+0.20}_{-0.22}$

Table 4.1: Selected parameters of the ten BBH mergers events detected during LIGO's O1 and O2 runs. The parameters are median values, with 90% credible intervals [2].

We list in Table 4.1 the relevant observed properties of the 10 BBH merger

events we consider in our study: the masses of each individual black hole m_1 and m_2 (columns 2 and 3), and the corresponding dimensionless effective spin χ_{eff} (column 4). It is worth pointing out that before the first gravitational wave detection, LIGO was expecting 33-100 more NS-NS binary events compared with BH-BH binaries [91]; however, LIGO's O1 and O2 run showed that the rate of BH-BH binaries is an order of magnitude *greater* than the NS-NS binaries. Furthermore, the range of black hole masses was expected to be from $\sim 5\text{M}_\odot$ to $\sim 15\text{M}_\odot$ [92]. As a result, the first detection (GW150914) came somewhat as a surprise, because previously-known black holes were significantly lighter than the inferred masses, among various reasons.

As evident in Table 4.1, the majority of black holes are over $25\text{M}_\odot$ with the heaviest being $50\text{M}_\odot$ (GW170729). The nature of this new population of heavy stellar-mass black holes is still debated in the literature [93, 94, 95, 96]; notice that a reason for observing more massive binary mergers over lighter ones could partly be explained as a selection bias [97], since more massive BBH mergers produce a louder signal, and therefore the accessible space-time volume is larger than for lighter systems. It has been proposed that there exists a mass gap ($\sim 50\text{M}_\odot - 150\text{M}_\odot$) due to pair-instability supernovae for stellar black holes [98, 99, 93] and therefore, that the black hole masses cannot be arbitrary large. There have also been claims of a cutoff at high masses in the current detections made by LIGO to date [100, 101, 102, 103].

The last column of Table 4.1 shows the most interesting parameter for this work: the effective spin χ_{eff}, defined by Eq. (4.2). The listed 10 observed events appear to disfavor high spin magnitude aligned with the orbital angular momentum, unlike the large spin values (near to the maximum possible value) observed in the majority of black holes in X-ray binaries [104, 105]. Most events are consis-

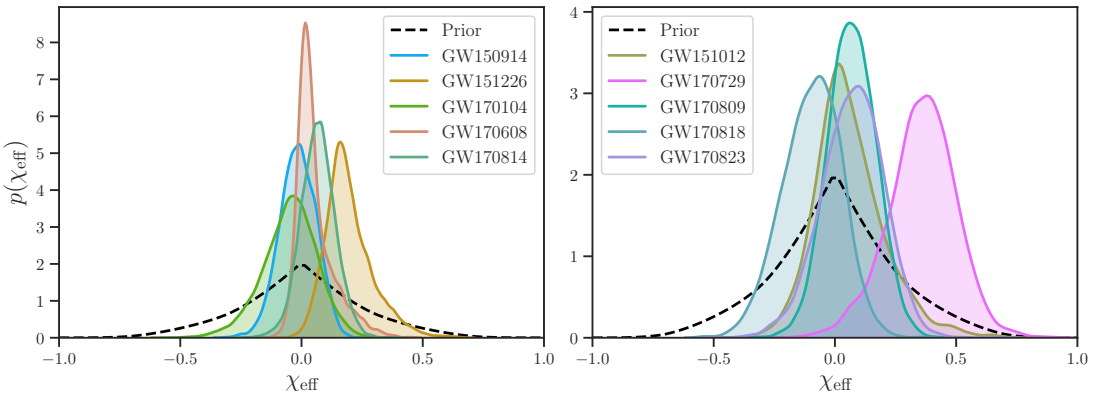

Figure 4.1: Posterior probability densities for the effective aligned spin magnitude $\chi_{\rm eff}$ for the 10 events from the LIGO-Virgo observations [2] as given in the files downloadable at `https://dcc.ligo.org/LIGO-P1800370/public`. Notice the difference in the vertical scale for the left and right panels.

tent with $\chi_{\rm eff} = 0$, with two exceptions: GW170729 and GW151226. These two events show evidence of positive, but relatively small, $\chi_{\rm eff}$ values. Fig. 4.1 shows the posterior distribution of $\chi_{\rm eff}$ for the ten events observed by LIGO's O1 and O2 run and the prior assumed by the LIGO Collaboration[1].

It is important to note that the LIGO Collaboration used Bayesian statistics to analyze the data and to infer the source properties of all ten BBH gravitational wave events [2]. This means that one needs to properly define prior probability density distributions. While ideally the conclusions should be robust and fairly independent under the choice of different priors, if the data are only mildly informative, priors could influence the statistical inference on the source parameters (see Ref. [106] for a discussion on this point). An analysis of the importance and effect of the choice of priors on the first three LIGO events has been carried out in Ref. [86]. One should also bear in mind that there certainly exist selection bias effects for the posterior distribution of $\chi_{\rm eff}$. For instance, sources with positive

[1] `https://dcc.ligo.org/LIGO-P1800370/public`

$\chi_{\rm eff} > 0$ have a more clear signal, due to longer time orbiting before merging, therefore allowing to better constrain the waveform (see e.g. Ref. [107, 108]).

4.2.2 PBH spin distribution

Given a spin distribution for the intrinsic spin of individual primordial black holes, and the assumption of isotropy in the spin-orbit alignment, one can calculate the distribution of $\chi_{\rm eff}$. We follow here Ref. [90] in assuming that the distribution function for the intrinsic spin magnitude of a single PBH can be closely approximated by the Gaussian functional form

$$p(\chi) \approx \exp\left[-\frac{\chi^2}{2\sigma^2}\right]. \tag{4.3}$$

The parameter σ is, in principle, calculable given the spectrum of density perturbations leading to PBH formation in the early universe. Absent this, and in view of the fact that there might be circumstantial evidence for a PBH origin of at least some of the detected BBH merger events [109], here we infer the value of σ directly from observations. To this end, we define a probability distribution for χ as a half Gaussian

$$p(\chi;\mu,\sigma) = \frac{\mathcal{N}(\mu,\sigma)}{\sqrt{2\pi}\sigma}\exp\left[-\frac{(\chi-\mu)^2}{2\sigma^2}\right], \tag{4.4}$$

entertaining a possible non-zero value for μ. In Eq. (4.4) $\mathcal{N}(\mu,\sigma)$ is the appropriate normalization constant. Notice that the function is only defined in the interval $\chi \in [0,1]$ and zero otherwise (see the definition of χ in Eq.(4.1)). Our goal is to investigate the probability distribution of $\chi_{\rm eff}$ resulting from an isotropic spin orientation distribution and the intrinsic spin distribution of Eq. (4.4) and to infer the posterior probability density for the parameters μ and σ from the LIGO-Virgo

data.

We utilize here a *hierarchical Bayesian analysis*: we assume that the individual BHs in the binary are coming from a primordial population which is described by some hyper-parameters Λ. Then, we use the 10 LIGO-Virgo events to derive the posterior distribution for Λ. Our approach is analogous to Refs. [84, 87, 101, 110]. Our goal is thus to find $p\left(\Lambda \mid d\right)$, the probability distribution of the parameters Λ given the data d, where Λ simply represents here the parameters that describe the PBH population $\Lambda = \{\mu, \sigma\}$.

Assuming that the events are independent of each other, we can combine the individual likelihoods to build a joint likelihood

$$p\left(\{d^i\} \mid \Lambda\right) = \prod_{i=1}^{N_{\rm obs}} p\left(d^i \mid \Lambda\right), \tag{4.5}$$

where

$$p\left(d^i \mid \Lambda\right) = \int \mathrm{d}\chi_{\rm eff}^i \, p\left(d^i \mid \chi_{\rm eff}^i\right) p\left(\chi_{\rm eff}^i \mid \Lambda\right) \tag{4.6}$$

is the likelihood function for ith event and $p\left(d \mid \chi_{\rm eff}\right)$ is the marginal likelihood, meaning that it has been marginalized over all parameters but $\chi_{\rm eff}$. Since the LIGO-Virgo collaboration have not yet released the marginalized or full likelihoods to the general public, but have rather provided the posterior distributions which we show in Fig. 4.1, we need to re-weight the posterior distribution of $\chi_{\rm eff}$ to obtain the likelihoods. The last term in the integral, $p\left(\chi_{\rm eff} \mid \Lambda\right)$, is the probability of measuring $\chi_{\rm eff}$ given the parameters of our model Λ. In our case this distribution of $\chi_{\rm eff}$ has been derived in App. C.1.1 and the result is given in Eq. (C.4). Finally, using Bayes' theorem we obtain the posterior distribution of the parameters Λ as

$$p\left(\Lambda \mid \left\{d^i\right\}\right) \propto \left[\prod_{i=1}^{N_{\rm obs}} \int \mathrm{d}\chi_{\rm eff}^i \, p\left(d^i \mid \chi_{\rm eff}^i\right) p\left(\chi_{\rm eff}^i \mid \Lambda\right)\right] p\left(\Lambda\right) \, . \tag{4.7}$$

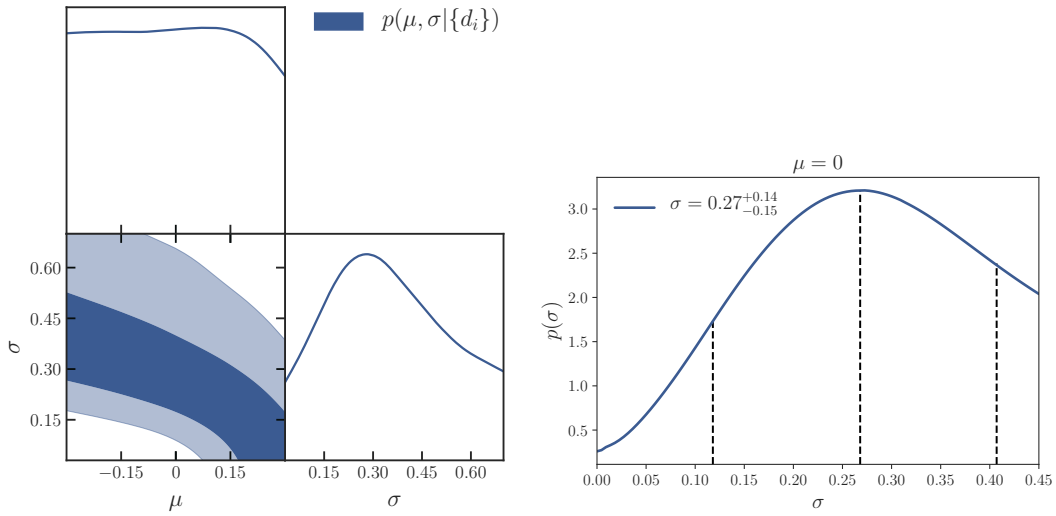

Figure 4.2: *Left*: Marginalized probability density functions for the μ and σ parameters describing the intrinsic PBH spin magnitude distribution. Colored contours show the 50% and 90% credible intervals. *Right*: Probability density functions for σ parameters with $\mu = 0$ with 90% credible intervals.

Here, $p(\Lambda)$ is the prior choice for the parameters Λ, which we take here to be uninformative (i.e. we use a flat prior for both μ and σ).

The posterior distribution for the hyper-parameters μ and σ describing the putative PBH population given the 10 LIGO-Virgo events is shown in the left panel in Fig. 4.2. The distribution for μ is almost flat, except for $\mu > 0.15$, a slightly disfavored range of values. In contrast, the distribution for σ offers more information: one can clearly see a peak around ~ 0.3. Notice that μ and σ are anti-correlated, as expected: given a half Gaussian with zero mean and fixed width, one can find an approximately equivalent distribution with a *negative* mean and larger width; conversely, a distribution with a positive mean will correspond to one with mean zero and a narrower width.

Finally, in the right panel of Fig. 4.2 we show the posterior distribution of σ when we set $\mu = 0$. This choice is motivated by the analytical findings of Ref. [90] (see their Eq.(17) and figure 2), and is approximately valid even in the scenario

discussed in Ref. [3], where the preferred value of μ is non-zero but extremely small (see their Eq.(8.7) and Fig.7).

Based on the 10 LIGO-Virgo events under consideration here, the best fit value for σ is $0.27^{+0.14}_{-0.15}$, which, remarkably, is *inconsistent* with zero at 90% confidence level. Notice that the distribution does not change much compared to the general case where we marginalize over μ, indicating that the data is largely insensitive to the value of μ.

4.2.3 Benchmark spin models for astrophysical BH

We are interested in comparing the $\chi_{\rm eff}$ distribution for PBH, discussed above, with what predicted in the case of astrophysical black holes. Given the current status of observations and the output of population synthesis codes, it is presently unwarranted to try to reproduce specific binary black hole spin distribution reflective of given astrophysical formation processes. Rather, it has become somewhat customary in the literature to adopt simplified benchmark models for the alignment and intrinsic spin distributions of astrophysical black holes, following what proposed in Ref. [87], and endorsed and utilized by the LIGO collaboration [4] and by others (see e.g. [110]). We shall assume that the merging black holes have equal mass (see a discussion of the effect of unequal mass mergers on $\chi_{\rm eff}$ in the Appendix), and that the distribution for the spin magnitude is statistically independent of that for the spin alignment.

Noting that the spin directions for isolated binary black holes are thought to be dominantly aligned (see e.g. [111, 112, 113]), we choose a distribution for the spin direction with perfect alignment as an extreme case. We note that this assumptions reflects under any circumstances an extreme, idealized situation for a variety of reasons: for instance, there exists evidence for spin-orbit *misalignment* in

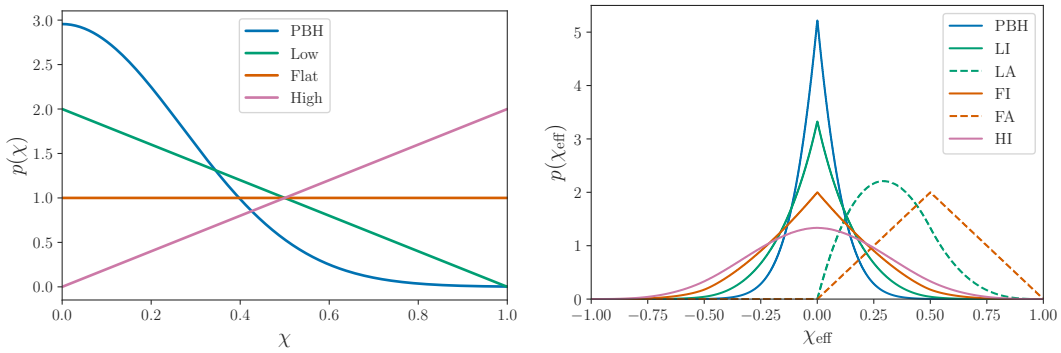

Figure 4.3: *Left*: Normalized spin magnitude distributions for PBH, low, flat and high spin models. *Right*: Prior distributions for $\chi_{\rm eff}$ for the different models under consideration here. Solid lines indicate isotropic models while the two dashed lines to the far right (peaking at $\chi_{\rm eff} \neq 0$) correspond to spin-orbit aligned ones.

black hole X-ray binaries [114], and effects from the supernova explosion could also contribute to tilt the spin-orbit angle (natal kicks) [115]. We study the systematic effects of relaxing the assumption of perfect alignment in the Appendix, see in particular Fig. C.2, bottom panel.

We parameterize the astrophysical spin magnitude following the spin distribution proposed by [87] and used by LIGO [4] and [110]. The models consist of 3 different spin magnitude distributions:

- a *low* (intrinsic) spin distribution $p(\chi) = 2(1-\chi)$ (L),
- a *flat* spin distribution $p(\chi) = 1$ (F), and
- a *high* spin distribution $p(\chi) = 2\chi$ (H).

We reproduce the distributions in the left panel of Fig. 4.3, together with the PBH intrinsic spin distribution for PBH for the central value of $\sigma = 0.27$ and $\mu = 0$ inferred above.

Also following Ref. [87], we consider two spin-orbit distribution orientations: *aligned* and *isotropic*. Notice that the tilt angle is an excellent tracer of BBH

formation channels [116], with the aligned distribution expected for isolated binary formation channel [99, 88, 92, 117], under the simplifying assumption that the binaries remain perfectly aligned throughout their evolution (an assumption that could be violated by effects such as supernova natal kicks, although mass transfer and tidal interactions might work in the opposite direction and tend to re-align the binary). The isotropic distribution is motivated by dynamical formation mechanisms in dense stellar environments or similarly disordered assembly scenarios [118, 119, 120], as well as by what expected for PBH [121].

The final prior distribution for $\chi_{\rm eff}$ for the various models under consideration is shown in the right panel of Fig. 4.3, where we do not include the HA model which is already strongly excluded by data. Notice that since the intrinsic spin distribution is positive-definite, "aligned" models do not allow for negative values of $\chi_{\rm eff}$; finally, also notice how the prior distribution for "isotropic" models is symmetric in $\chi_{\rm eff}$.

4.3 Analysis and Results

We present here our results for the odds ratios of the different prior distributions for $\chi_{\rm eff}$ outlined in the previous section, as well as the posterior probability density functions for a "mixed" scenario with PBH providing a fraction f of the BBH events. We then discuss how, under different assumptions, such odds ratios will evolve with additional events in the future, and how knowledge of which fraction of the events originates from which prior distribution will change with greater statistics (sec. 4.3.2).

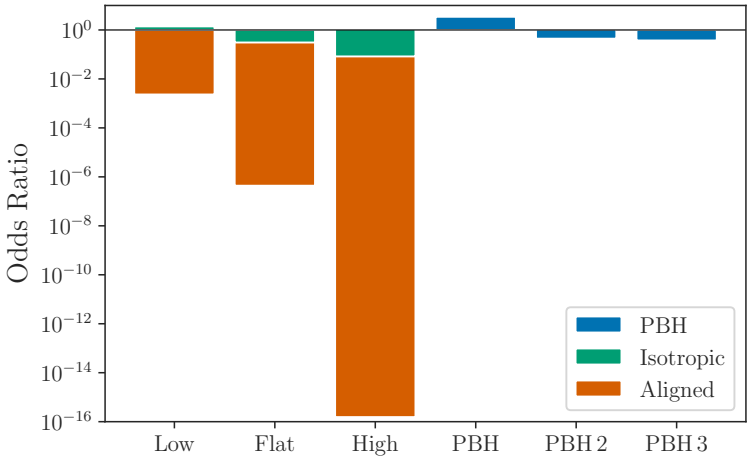

Figure 4.4: Odds ratios for different models with respect to the LI benchmark model. Larger odds ratios show higher statistical preference, with ratios larger than 1 indicating a preference with respect to the benchmark LI model. The low, flat and high spin magnitude are combined with the isotropic and aligned spin-orbit orientation distributions. The PBH model is for a fixed $\sigma = 0.27$, PBH 2 and PBH 3 are for $(\nu = 6, \gamma = 0.8)$ and $(\nu = 6,\ \gamma = 0.88)$ respectively, in the notation of Ref. [3] (see text for details).

4.3.1 Comparing models to observations: odds ratios and mixture

We confront here the prior distributions obtained in the previous section with data by calculating *odds ratios*, which quantify the statistical support for a model over another, allowing us to compare models and giving us a statistically-motivated selection criterion. Fig. 4.4 shows the odds ratios between all possible models and the reference low-intrinsic-spin, isotropic (LI) model; what we show is therefore defined as $p(d|\mathrm{M})/p(d|\mathrm{LI})$ for model M given the 10 events d. Here, we have already assigned equal probability to the prior probability distributions of each and every model (i.e., we assume that all models are equally likely a priori). This implies that the odds ratio and the Bayes factor are equivalent.

Fig. 4.4 shows how all models with aligned spin distribution are significantly

LIGO	Low	Flat	High
Isotropic	0.0	-0.93	-2.07
Aligned	-4.12	-12.92	-32.37

This work	Low	Flat	High	PBH
Isotropic	0.0	-1.18	-2.49	0.39
Aligned	-6.07	-14.65	-36.41	

Table 4.2: Natural log Bayes factors for various spin distributions with $q = 1$. *Right*: Values reported by LIGO [4]. *Left*: Values found in this work.

disfavored with respect to the isotropic ones. Also if we compare the "favored" aligned model, which is the one corresponding to a low intrinsic spin distribution (LA), with the least favored isotropic model, which is the one with high intrinsic spin distribution (HI), the odds ratio in favour of HI is still very large, at $36:1$.

In addition to showing a strong statistical evidence for isotropy of spin and orbit orientations, the data favour models with small intrinsic spin magnitude distributions and heavily disfavour those with high spin. The two best models are the PBH and LI with the PBH model slightly preferred over the LI with an odds ratio of $3:2$.

Notice that the intrinsic spin distribution we assume for PBH was calculated in Ref. [90] by integrating the probability density $P(\chi, \delta)$, with χ the intrinsic spin and δ the overdensity giving rise to the PBH formation, over δ. Critically, Ref. [90] assumes no correlation between δ and χ. When this assumption is relaxed, one generally finds much narrower intrinsic spin distributions [3]. In the notation of Ref. [3], the probability distribution for χ in the case of PBH depends on the parameter ν, defined as the ratio of the critical collapse overdensity and the variance of the overdensity at horizon crossing, and on the parameter γ which effectively measures the width of the PBH mass function, with $\gamma = 1$ for a monochromatic

power spectrum.

Figure 5 of Ref. [3] shows that the relevant range for the parameter ν for LIGO-sized PBH is around $\nu \sim 6$. While the range for the parameter γ depends on the PBH mass function, mass functions peaked around a few solar masses typically have values of $\gamma \sim 0.85...0.88$ (see their sections 7.2 and 7.3), although a broader range is possible. Here, we take as benchmark cases ($\nu = 6,\ \gamma = 0.8$) (which we indicate in Fig. 4.4 as PBH 2) and ($\nu = 6,\ \gamma = 0.88$) (PBH 3 in Fig. 4.4), the latter leading to the narrowest possible prior distribution for $\chi_{\rm eff}$, and the former with a broader distribution. We show the prior distribution for the two models in the bottom panel of Fig. C.1.

We find odds ratio of 0.44 and 0.37 respectively for PBH 2 and 3, indicating (since both odds ratios are smaller than 1) a statistical preference for the LI model as well as for our benchmark PBH model over these narrower intrinsic PBH spin distribution. As expected, our current ability to distinguish between models with very low spin distribution is very limited with the available data. Similar results and conclusions have been found in [84, 110]. For reference and to summarize our findings, we list in Table 4.2 the natural log Bayes factors for various models compared to the benchmark LI model.

The actual LIGO BBH population likely reflects a mixed population of two different models (or more). Here, we are going to assume that the mixture is our PBH model with the second one any of the following models: LI, LA, FI, FA and HI. In Fig. 4.5 we show the posterior probability density for the *fraction of the BBH mergers coming from PBH*, which we indicate with f, where $f = 1$ means that all the events are from PBH and $f = 0$ means the opposite, i.e. all the events are coming from the second model and none from PBH. Notice that if we allow a mixed model we find a statistical preference for the majority of events coming

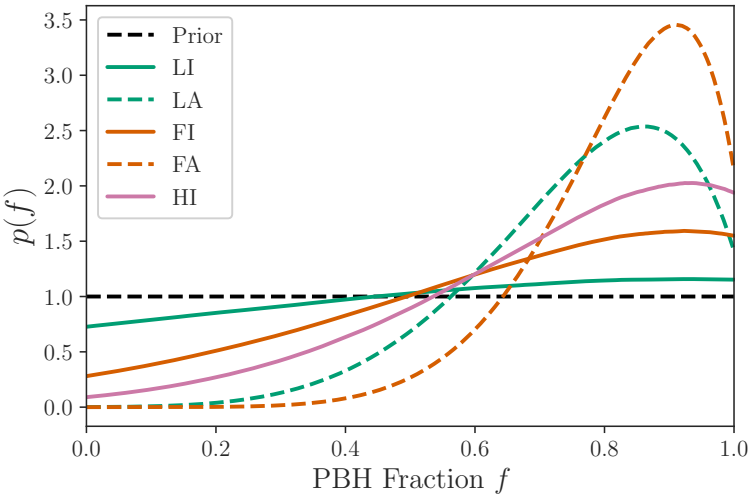

Figure 4.5: Posterior probability density functions on the parameter f for the 10 events observed by LIGO. $f = 1$ corresponds to all coming from PBH.

from a PBH population. For the case where the mixed model consists of PBH and FA (dashed orange line), the f distribution peaks around ~ 0.9, therefore favoring a scenario where 9 events come from a PBH population and 1 event from the FA population. This is somewhat expected because there clearly is one event (GW170729) that could have come more likely from a population favoring large $\chi_{\rm eff}$ values such as what predicted in the FA prior distribution rather than PBH. A similar conclusion can be drawn when the second mixture model is LA (dashed green line). In this second case, there are *two events* that could be ascribed to a LA distributions: GW170729 and GW170729. This is why the f posterior distribution peaks around ~ 0.85, a little lower than the case of FA. For the case of a mixture of FI (solid orange line) or HI (solid pink line) with PBH, the probability distribution for f is flatter, but we still can conclude that more than half of the events are coming from a PBH population. Lastly, in the case of a mixture model consisting of PBH and LI (solid green line) the distribution is almost half PBH and half LI with a slight preference for the PBH model, as

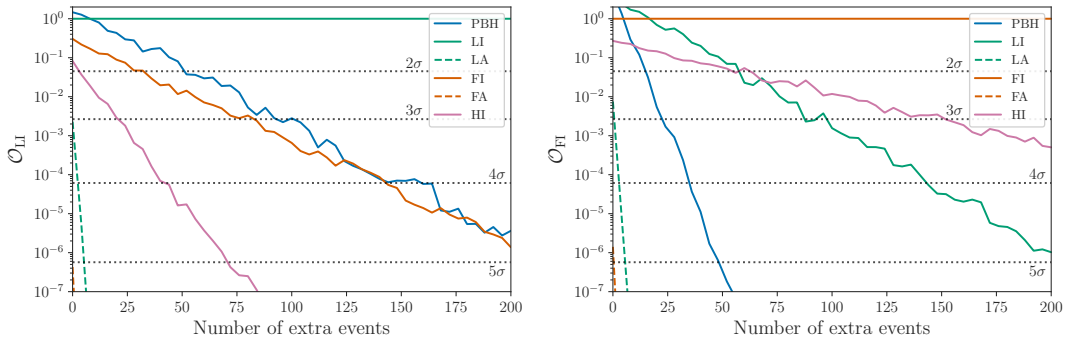

Figure 4.6: Evolution of the odds ratio as a function of the number of extra events for 200 LI (*left*) and 200 FI (*right*) simulated events.

expected from the odds ratio between the two models, which have comparably similar $\chi_{\rm eff}$ prior distributions.

4.3.2 Future events

To test the sensitivity of our setup to the different benchmark models under consideration, we simulate future events for each of the six population models under consideration: PBH, LI, LA, FI, FA and HI. We generate mock observations following the same approach as in Refs. [87, 84]. First, We approximate each LIGO event as a Gaussian with the same mean value and 90% credible interval; Second, we draw a value of $\chi_{\rm eff}^{\rm true}$ from the population's distribution we want to simulate; third, we generate an observation from the distribution $\chi_{\rm eff}^{\rm obs} \sim \mathcal{N}(\chi_{\rm eff}^{\rm true}, \sigma^{\rm unc})$, where $\sigma^{\rm unc}$ is a random uncertainty from one of LIGO's ten events. Finally, the we calculate the posterior probability as $\sim \mathcal{N}(\chi_{\rm eff}^{\rm true}, \sigma^{\rm unc}) p_{\rm FI}(\chi_{\rm eff})$.

Assuming that all events are coming from the same population, we simulate 200 events for three possible "true" scenarios: FI, LI or PBH. Fig. 4.6 shows the dependence of the odds ratio with respect to the number of extra events from LI (left) and FI (right) populations. Notice that the odds ratios for the models already start at different values, because the current 10 LIGO events are included:

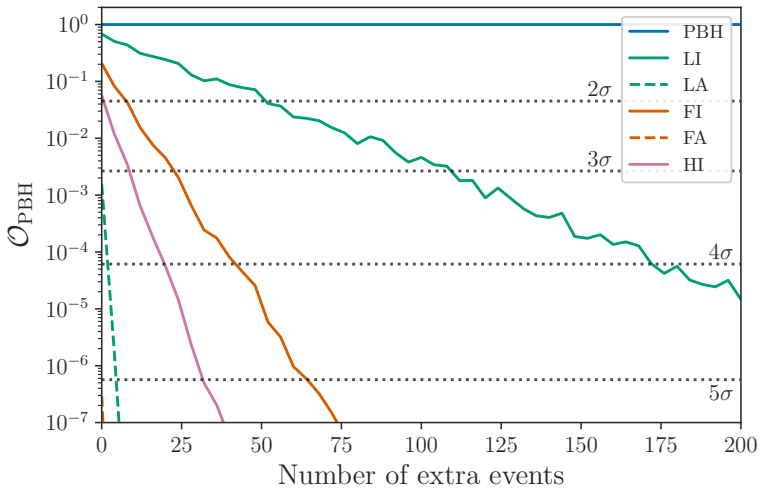

Figure 4.7: Evolution of the odds ratio as a function of the number of extra events for 200 PBH simulated events.

the starting point for each model is thus just the odds ratio from Table 4.2.

For the fully LI-simulated population, our results show that with only 10 extra events the FA and LA models might be disfavoured at more than the 5σ level, and that 75 extra events are needed to reject the the HI model at the same confidence level. The LI and PBH models would be disfavored at the same level with even more events, reaching close to a 5σ level with 200 extra events.

Under the assumption that the true population is FI, the evolution of the odds ratios is shown in the right panel of Fig. 4.6. With less than 10 extra events we find that it would be possible to heavily disfavor both the FA and LA models; interestingly, the PBH model can also be rejected at the 5σ level with only 50 extra events. The entire 200 extra events would allow for a 5σ rejection threshold for the LI model and 3σ for the HI model. Finally, if the true population is that of PBHs, as in Fig. 4.7, all models except LI can be rejected at 5σ level with only 75 extra events. We find that 200 extra events would be needed to discriminate the LI model over the PBH one at the 4σ level.

Once again, we emphasize that there is no reason to assume all events observed

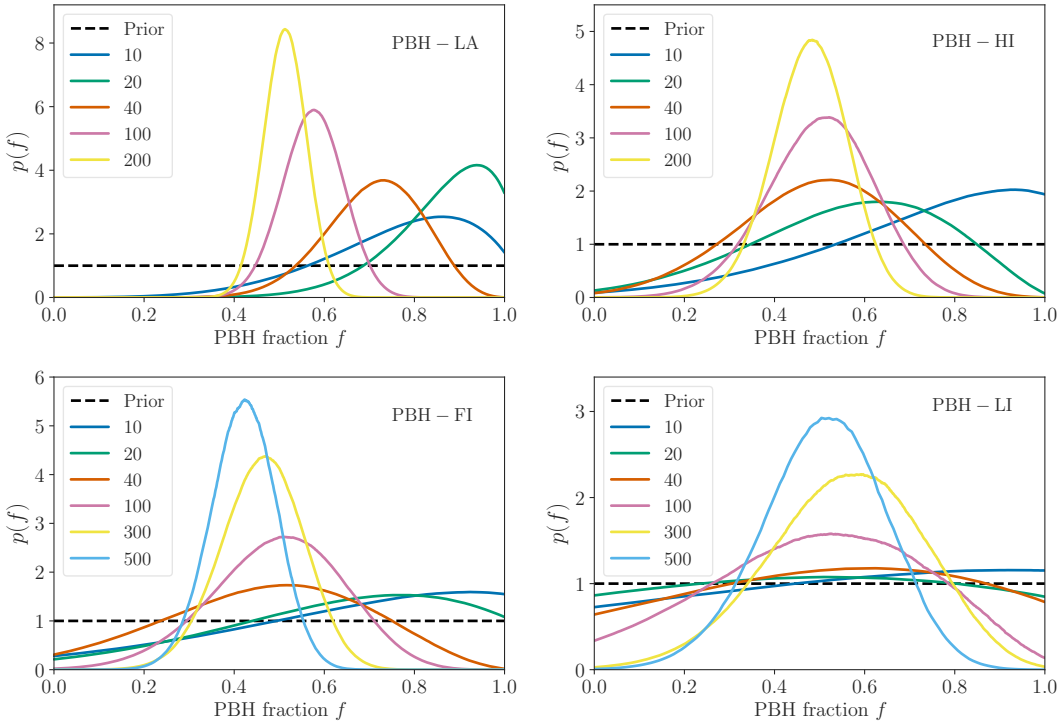

Figure 4.8: Posterior probability density functions for the PBH fraction f for 4 mixed populations.

by LIGO are coming from the same single population. In what follows we therefore consider a mixed population consisting of half PBH and half of a second model among LI, FI, HI or LA. We simulate up to 500 mixed events for each of these mixed populations.

In the upper panels of Fig. 4.8, we show that it is possible to infer the relative fraction of PBH f (which is given on the horizontal axis) with high confidence with 200 events for the case of PBH-LA and PBH-HI mixture models. To be able to discriminate the mixture fraction between PBH and FI, more events are needed than in the previous two cases, as shown in the bottom left panel of Fig. 4.8. After detecting 500 events the value of f can be determined fairly precisely. Additional events are needed when the two prior distributions for the two models are similar, such as for the case of a mixed PBH-LI population, bottom right in Fig. 4.8. This notwithstanding, the value of f peaks at the correct value of ~ 0.5 but the spread is still substantial, even with 500 extra events.

Run O3 of LIGO-Virgo has already commenced, and the projected inferred rate of BBH mergers from the previous runs is around $9.7 - 101\,\mathrm{Gpc}^{-3}\,\mathrm{y}^{-1}$ [2]. At this moment, the number of putative candidate run O3 BBH merger events is 10, from a period of approximately 1.5 months[2], which would imply an approximate total number of events per year of around 80.

4.4 Discussion and Conclusions

In this study we considered how measurements of the effective spin parameter $\chi_{\rm eff}$ provide information on the origin of merging binary black holes observed with gravitational wave telescopes. To this end, we presented a calculation of the prior distribution for primordial black holes as well as for a few representative bench-

[2] `https://gracedb.ligo.org/latest/`

mark distributions possibly indicative of what expected in simple astrophysical black hole binary populations.

In the case of PBHs, following Ref. [90] we assumed no correlation between the overdensity leading to the black hole formation in the early universe and the intrinsic black hole spin; the resulting intrinsic spin distribution is a positive-definite half-Gaussian with zero mean; to fix the width of the intrinsic spin distribution we calculated the prior distribution for the effective spin parameter $\chi_{\rm eff}$ and we utilized 10 LIGO-Virgo measurements of $\chi_{\rm eff}$ to determine a best-fit intrinsic spin width.

We then proceeded to compare odds ratios for the current set of 10 measurements for $\chi_{\rm eff}$ for the various models under consideration. We showed that with current data the $\chi_{\rm eff}$ measurements have a marginal, and not highly statistical significant preference for a dominant population of primordial black holes over the best fitting astrophysical model. We also calculated the posterior probability for the relative fraction of primordial versus astrophysical BBH events, finding that there is a preference for a scenario where one or two events originate from a population with preferentially aligned spin-orbit distributions, and the remaining eight-to-nine events from a population with an isotropic spin-orbit distribution and low intrinsic spin.

We then assessed the number of future events needed to disentangle, at a given significance level, BBH from different populations, assuming that all binaries originate from the same "true" distribution. Generally, non-isotropic spin distributions are highly disfavored even when only considering the current 10 events. In addition, even for isotropic alignment distributions, it will quickly become possible to distinguish models with large intrinsic spin from those with low intrinsic spin magnitude distributions. Assuming that the entirety of the merging black holes

have a primordial origin, we anticipate that distinguishing at 3σ their $\chi_{\rm eff}$ distribution from a low intrinsic spin, aligned spin distribution will require on the order of 100 additional events.

Finally, we illustrated the number of events necessary to acquire information on the relative fraction of primordial versus non primordial binary black holes. Once again, if the population of non-primordial black holes has a preferentially aligned spin-orbit distribution, such fraction can be pinpointed with relatively few additional events; the posterior distribution for the relative fraction of events from populations with isotropic spin-orbit distribution shows a peak generally pointing to a systematically larger-than-true fraction of primordial black holes, but eventually converging with large-enough statistics to the "true" value.

In the App. C, we discuss the systematics associated with three key assumptions used in our analysis: (1) the width σ of the primordial black hole intrinsic spin distribution, (2) the mass ratio we use to calculate the $\chi_{\rm eff}$ prior distribution, and (3) the assumption of perfect alignment between spin and orbit.

Clearly, as an increasingly large statistics of BBH mergers becomes available, the question of the origin of the population of merging black holes will come into sharper focus not only with studies of the effective spin parameter, but using all other pieces of information, including but not limited to the mass distribution of events, the correlation between mass and spin, localization information, etc. Interesting questions relating for instance to the degree to which BBH accrete will also be tackled, including the issue of whether there could be substantial accretion for PBH and how much accretion would spin up individual PBHs [122]: possibly, if PBHs do significantly accrete, the heavier ones would have both higher spin and higher $\chi_{\rm eff}$. Interestingly, this seems to be the case for the most massive LIGO event (GW170729) and for the recent, claimed detection events GW151216

[123] and GW170403 [124]. The central issue of observational bias in inferring the origin of merging BBH will also be helped greatly by benefiting from increased statistics. Finally, we also expect that theoretical and observational progress will lead to more realistic models for the expected distributions for the intrinsic spin and spin-orbit correlation of different populations of astrophysical black holes, allowing firmer statements on the origin of merging black holes than what is possible with the benchmark models currently in use.

Chapter 5

Conclusion

In this thesis, we have presented a comprehensive study of DM production in modified cosmologies for two popular mechanisms: freeze-out and freeze-in. In chapter 2, we showed that in an non-standard cosmological history where the universe expands very fast, as in presence of a new species ϕ whose energy density red-shifts as $\rho_\phi \propto a^{-(4+n)}$, the relic DM density from freeze-out is then significantly larger than the one obtained by a standard calculation, as a result of equality between the (faster) expansion rate and the thermal processes rates occurring at earlier times (i.e. at higher temperatures, when the comoving DM density is larger). The key consequence for DM phenomenology is that that larger couplings (and therefore larger predicted experimental signals, for example for the annihilation rate of dark matter pairs in the late universe) are needed to produce the observed DM abundance. Moreover, we identified a completely new phenomenon that happens for large enough n: unlike the standard case, DM particles keep annihilating even long after the departure from chemical equilibrium. This novel behavior was dubbed *relentless* DM, and it was later confirmed by Ref. [50]. Relentless DM also generically features larger-than-usual DM interaction rates with ordinary particles.

In chapter 3, we focused our study on three specific mechanisms of dark matter freeze-in: (i) the production from decay of some other particle species in the early universe, (ii) the production of a single dark matter particle in the final state of a $2 \to 2$ scattering process, and (iii) the production of a dark matter pair from a scattering process. For each case, we provided complete expression for the relevant collision operators, reducing the task of calculating the resulting freeze-in abundance to a simple integral. The general and universal finding is that in a faster-than-standard expanding universe, freeze-in production is suppressed, implying that to produce enough dark matter to match observations, larger couplings, and thus larger detection rates, are in order.

Lastly in chapter 4, we considered how measurements of the effective spin parameter $\chi_{\rm eff}$ provide information on the origin of merging binary black holes observed by LIGO-Virgo. To this end, we presented a calculation of the odds ratio for primordial black holes as well as for a few representative benchmark distributions possibly indicative of what expected in simple astrophysical black hole binary populations. We found that the PBH model agrees well with the data and can be a possible explanation of the events observed by LIGO and Virgo. Furthermore, if the underlying population of the BBH is unique, only 100 events are needed to be able to distinguish between models with very high statistical significance. Finally, we illustrated the number of events necessary to acquire information on the relative fraction of primordial versus non primordial binary black holes.

Appendix A

Appendix

A.1 Dark matter thermalization

The DM production mechanism depends on whether the DM ever reaches thermal equilibrium at early times. Thermalization is achieved by collisions, therefore a faster expanding universe makes it harder for the DM to thermalize. This is what we investigate in this Appendix, checking whether the interaction rate between DM and the radiation bath was ever larger than the expansion rate at high temperatures. If this was the case, then DM reaches thermal equilibrium and it is produced through thermal freeze-out. In the opposite case, the production mechanism must be non-thermal.

For temperatures much larger than the DM mass, the scattering rate can be parameterized as follows

$$\begin{aligned}\Gamma_{\rm scatt}(T) &\simeq n_{\rm DM}\sigma_{\rm scatt}v_{\rm rel} \\ &\simeq \frac{3}{2}\frac{\zeta(3)}{\pi^2}T^3\,\frac{\lambda^4}{32\pi}\,\frac{T^2}{(T^2+M_*^2)^2}\ .\end{aligned} \tag{A.1}$$

Here, we use the number density for a Majorana fermion in the relativistic regime,

and the scattering is assumed to be mediated by a particle with mass M_* that couples to DM and radiation with strength λ. In what follows, we explore two different possibilities for M_*.

A.1.1 Massless Mediator

The first case we study is a massless mediator, $M_* = 0$. Strictly speaking, this analysis is valid also for the case of a massive mediator with mass smaller than the temperatures under consideration. For example, any mediator lighter than the DM particle would fall within this category. The scattering rate in this case reads

$$\Gamma_{\rm scatt}(T) \simeq \frac{3\,\lambda^4\,\zeta(3)}{64\pi^3}\,T\ , \qquad (M_* \ll T)\ . \tag{A.2}$$

This linear scaling with the temperature has to be contrasted with the Hubble rate proportional to $T^{2+n/2}$ (with $n > 0$, see Eq. (2.8)). At high enough temperatures the expansion rate wins, and interactions become more effective as the universe expands and cools down.

A comparison between the Hubble rate in Eq. (2.8) for different values of n and the scattering rate in Eq. (A.2) is shown in Fig. A.1, where we plot both these quantities as a function of the inverse temperature. The Hubble rate is obtained by fixing $T_r = 20$ MeV in order to have the faster expanding phase to last as long as possible, but still consistent with the BBN bounds discussed in Sec. 2.3. The red line corresponds to the standard cosmological history, the other colored line represent the faster expansion rate, with n the index appearing in the exponent of Eq. (2.8). The rate is computed by setting the size of the coupling $\lambda \simeq 1$. DM thermalizes at a temperature $T_{\rm th}$ defined to satisfy the condition $H(T_{\rm th}) = \Gamma_{\rm scatt}(T_{\rm th})$. In other words, this temperature can be obtained by finding the intersection between the black lined and the colored line under

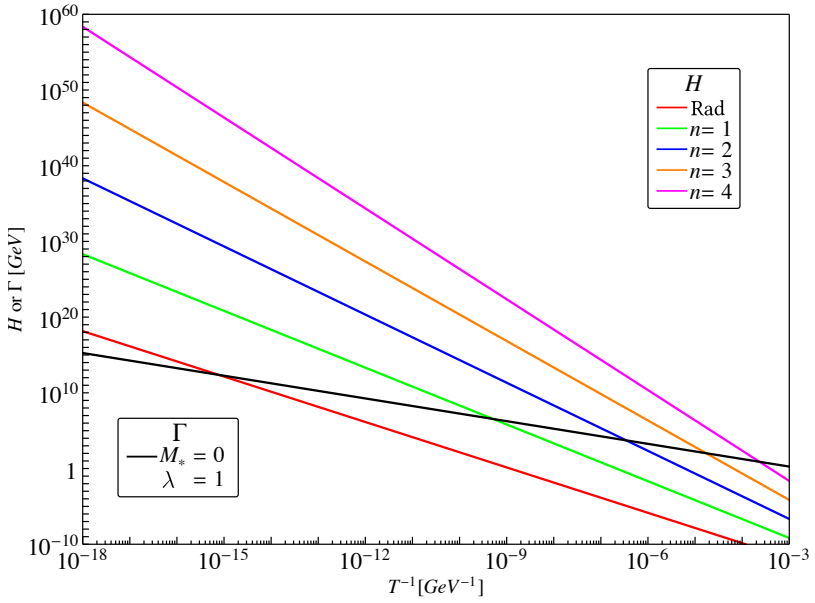

Figure A.1: Expansion rate (colored lines) and DM scattering rate (black line) as a function of the inverse temperature (time from left to right). We set the equality temperature between ϕ and radiation $T_r = 20\,\mathrm{MeV}$, and the coupling strength of the massless mediator $\lambda = 1$. DM is in thermal equilibrium for temperatures below the intersection between the black line and the colored line under consideration.

consideration in Fig. A.1. This value depends on n, and it falls within the range $T_{\rm th} \simeq (10^3, 10^9)\,\mathrm{GeV}$ as we vary n from 1 to 4. DM particles always achieve thermal equilibrium at temperatures higher than the weak scale, even in the extreme case $n = 4$.

The above conclusion would be altered if we considered smaller values for the coupling λ. We find it useful to write down an analytical expression for $T_{\rm th}$, which can be obtained by using the approximate expression for the Hubble rate in Eq. (2.8). The thermalization temperature approximately reads

$$T_{\rm th} \simeq \left(\frac{9\sqrt{10}\,\zeta(3)\,\lambda^4}{64\pi^4\,\overline{g}_*^{1/2}}\, M_{\rm Pl}\, T_r^{n/2} \right)^{2/(n+2)} . \tag{A.3}$$

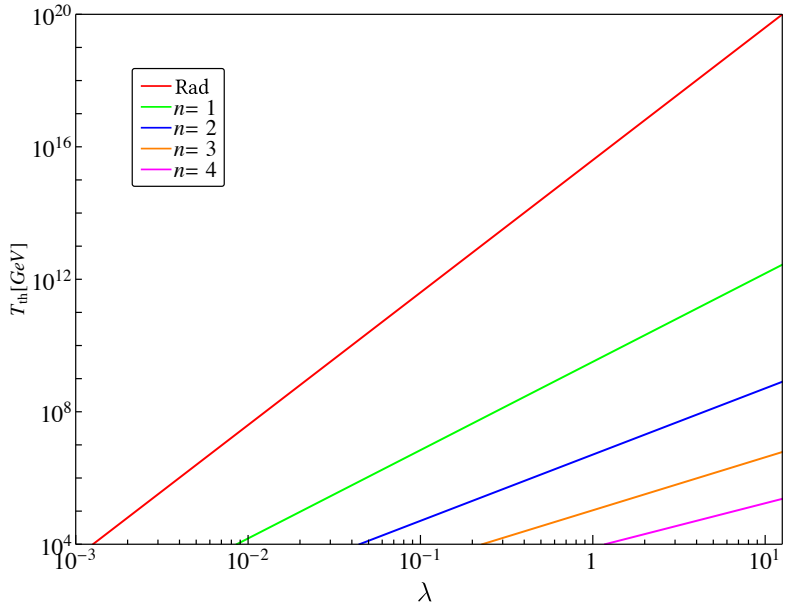

Figure A.2: DM thermalization temperature for a massless mediator as a function of λ. Parameters are chosen as in Fig. A.1.

It scales as $\lambda^{8/(n+2)}$, so taking a smaller λ would affect less the cases of larger n. By taking a weak interaction coupling $\lambda \simeq 0.3$, the thermalization temperature is in the range $T_{\rm th} \simeq (10^3, 10^8)\,\text{GeV}$. The numerical solution for the thermalization temperature as a function of λ is shown in Fig. A.2. For small couplings, $\lambda \lesssim 10^{-3}$, the thermalization temperature is below the weak scale. For weak scale DM this implies that thermal equilibrium is never achieved, and the production mechanism must necessarily be non-thermal.

A.1.2 Heavy Mediator

We consider here the case of heavy mediators. At temperatures below M_*, the scattering rate in approximately

$$\Gamma_{\rm scatt}(T) \simeq \frac{3\,\lambda^4\,\zeta(3)}{64\pi^3}\,\frac{T^5}{M_*^4}\ , \qquad (T \ll M_*)\ . \tag{A.4}$$

Unlike the case discussed above, the interaction rate now scales with a higher temperature power than the Hubble parameter. This means that at very early times interactions are effective, and as the temperature drops the expansion takes over. We illustrate this case in Fig. A.3, where we compare again the rates as a function of the (inverse) temperature. We consider three masses for the mediator. We define $m_\Lambda \simeq 10^{10}\,\text{GeV}$, the scale where the SM Higgs quartic vanishes [125], hinting for possible new physics [126, 127, 128, 129]. We also consider the unification scale for the gauge couplings ($M_{\rm GUT} \simeq 2\times 10^{16}\,\text{GeV}$) and the reduced Planck mass ($M_{\rm Pl}$). For an order one coupling, $\lambda \simeq 1$, thermalization is never achieved for $n > 0$. This conclusion is unchanged even if we badly break perturbation theory, $\lambda \simeq 4\pi$, and it is only strengthened if we consider smaller couplings. We conclude that for a heavy mediator, as heavy as at least $10^{10}\,\text{GeV}$, DM never equilibrates with the thermal plasma.

A.2 Neutron Freeze-Out and BBN

The neutron freeze-out temperature for the cosmological background studied in this work can be found by using the analytical results of Ref. [130]. The neutron abundance in conveniently expressed in terms of the neutron fraction $X_n \equiv n_n/(n_n + n_p)$, where $n_{n(p)}$ is the neutron (proton) abundance. The time

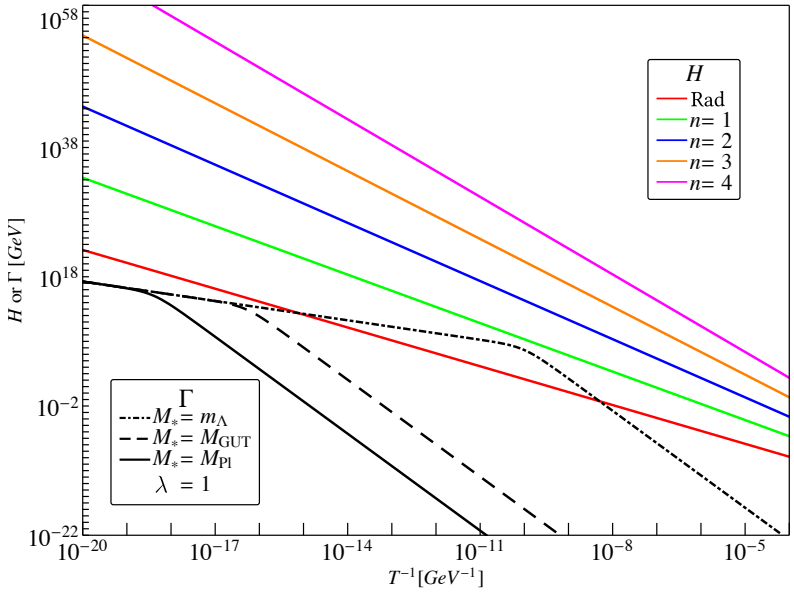

Figure A.3: Comparison between expansion and interaction rates. Parameters are chosen as in Fig. A.1, with the only difference that the mediator is massive.

evolution is described by the Boltzmann equation

$$\frac{dX_n}{dt} = -\lambda_{n\to p}\left(1 + e^{-Q/T}\right)\left(X_n - X_n^{\rm eq}\right) \ . \tag{A.5}$$

Here, we introduce the neutron-proton mass difference

$$Q \equiv m_n - m_p = 1.293 \text{ MeV} \ , \tag{A.6}$$

and the equilibrium neutron fraction reads

$$X_n^{\rm eq} = \frac{1}{1 + e^{Q/T}} \ . \tag{A.7}$$

For temperatures above the electrons mass, the neutron to proton conversion rates can be approximated by the analytical expression

$$\lambda_{n\to p} \simeq 2 \times 1.63 \left(\frac{T}{Q}\right)^3 \left(\frac{T}{Q} + 0.25\right)^2 \text{ sec}^{-1} \ . \tag{A.8}$$

This simple expression reproduces the full result within the accuracy of a few percent.

The Boltzmann equation for the neutron fraction can be solved as an asymptotic series

$$X_n = X_n^{\rm eq} \left[1 - \frac{\left(1 + e^{-Q/T}\right)^{-1}}{\lambda_{n\to p}} \frac{dX^{\rm eq}/dt}{X^{\rm eq}} + \dots\right] \ . \tag{A.9}$$

This expression is valid as long as the second term in the parenthesis is smaller than the first, namely if we are close to the equilibrium value. We define the neutron freeze-out as the temperature when the two are equal

$$\left| \frac{\left(1 + e^{-Q/T}\right)^{-1}}{\lambda_{n\to p}(T)} \frac{dX^{\rm eq}/dt}{X^{\rm eq}} \right|_{T=T_n^{\rm FO}} \simeq 1 \ . \tag{A.10}$$

The only missing information to solve this equation is the time vs temperature relation, which differs from the one for a standard cosmology due to the presence of ϕ. This can be derived by imposing conservation of the total entropy. Since we focus on temperatures around the MeV scale, we neglect the g_{*s} temperature dependence and the final equation for the freeze-out temperature reads

$$\left| \frac{\left(1 + e^{-Q/T}\right)^{-2}}{\lambda_{n\to p}(T)} \frac{Q}{T} H(T) \right|_{T=T_n^{\rm FO}} \simeq 1 \ . \tag{A.11}$$

The Hubble rate H as defined in Eq. (2.7) contains both the energy density of ϕ and radiation. If we only account for radiation and we solve Eq. (A.11) we find

$T_n^{\rm FO} \simeq 0.76\,{\rm MeV}$, valid for a standard cosmology [130]. If we also account for the ϕ energy density, we find that this result is not changed by much as long as we consider $T_r \geq 1\,{\rm MeV}$. More specifically, in the extreme case $n = 0$ (where there is no temperature dependence in N_ν) and $T_r = 1\,{\rm MeV}$ we find $T_n^{\rm FO} \simeq 0.83\,{\rm MeV}$. In order to put the most conservative bounds, we evaluate ΔN_ν as defined in Eq. (2.13) for $T = 1\,{\rm MeV}$.

A.3 Semi-Analytical Freeze-Out

In this Appendix we derive semi-analytical solutions for freeze-out relic density. We start with a review of the standard calculation for DM production in a background of radiation, then we extend it to the modified cosmological histories considered in this work.

A.3.1 Standard Cosmology

In order to connect with the new freeze-out scenarios studied in chapter 2, we review the Lee-Weinberg calculation for cold relics [8]. We simplify the Boltzmann equation in Eq. (2.16) by setting $g_* = g_{*s} = \text{const}$. Furthermore, we Taylor expand the equilibrium density in Eq. (2.17) for temperatures lower than the DM mass

$$Y_\chi^{\rm eq}(x) = \frac{45}{4\sqrt{2}\,\pi^{7/2}} \frac{g_\chi}{g_*}\, x^{3/2} e^{-x} + \ldots \qquad (x \gg 1)\ . \tag{A.12}$$

The Boltzmann equation can be written as follows

$$\frac{dY_\chi}{dx} = -\,A \frac{\langle \sigma v_{\rm rel} \rangle}{x^2} \left(Y_\chi^2 - Y_\chi^{\rm eq\,2} \right)\ , \tag{A.13}$$

where we define the constant [1]

$$A = \frac{s(m_\chi)}{H_{\rm rad}(m_\chi)} = \frac{2\sqrt{2}\,\pi}{3\sqrt{5}}\, g_*^{1/2}\, m_\chi M_{\rm Pl}\ . \tag{A.14}$$

We identify two distinct regimes for the solution. At early times, DM annihilations are efficient and Y_χ closely tracks the equilibrium distribution. At late times, the expansion takes over and the density freezes-out. We solve the Boltzmann equation in these two regimes and then match the two solutions at some intermediate point. We perform the matching at the temperature where Y_χ moves away from its equilibrium expression, a point known as the DM freeze-out.

We find it convenient to write the Boltzmann equation for $\Delta_\chi \equiv Y_\chi - Y_\chi^{\rm eq}$, which is obtained by plugging its definition into Eq. (A.13). We find

$$\frac{d\Delta_\chi}{dx} = -A\frac{\langle\sigma v_{\rm rel}\rangle}{x^2}\,\Delta_\chi(2Y_\chi^{\rm eq} + \Delta_\chi) - \frac{dY_\chi^{\rm eq}}{dx}\ . \tag{A.15}$$

At times much earlier than freeze-out, the departure from thermal equilibrium is minimal and we can neglect terms quadratic in Δ_χ and its derivative. As a consequence, the DM number density can be approximated by

$$Y_\chi(x) \simeq Y_\chi^{\rm eq}(x) + \frac{x^2}{2A\langle\sigma v_{\rm rel}\rangle} \qquad (1 < x < x_f)\ . \tag{A.16}$$

In the opposite regime, we neglect the equilibrium distribution in the Boltzmann equation (A.13), which can be integrated to find the solution

$$Y_\chi(x) \simeq \left[\frac{1}{Y_\chi(x_f)} + A\,J(x)\right]^{-1} \qquad (x > x_f)\ . \tag{A.17}$$

[1] $H_{\rm rad}(x)$ is Hubble parameter obtained by plugging only the energy density of the radiation bath. This is obviously the case for standard freeze-out. We find this definition useful also for the case when the energy density is dominated by ϕ.

Here, we define the annihilation integral

$$J(x) \equiv \int_{x_f}^{x} \frac{\langle \sigma v_{\rm rel} \rangle}{x^2} dx \ . \tag{A.18}$$

The term equal proportional to the inverse comoving density at the freeze-out in Eq. (A.17) is important to ensure that our solution is continuous. However, it is numerically subdominant, unless we consider values $x \simeq x_f$. This can be explicitly checked for the partial wave expansion of Eq. (2.18), for which the annihilation integral now reads:

$$J(x) \simeq \sigma_s \left(\frac{1}{x_f} - \frac{1}{x} \right) + \frac{\sigma_p}{2} \left(\frac{1}{x_f^2} - \frac{1}{x^2} \right) \ . \tag{A.19}$$

The comoving number density after freeze-out reads

$$Y_\chi(x) = \frac{x_f}{A} \begin{cases} \frac{\left(1 - x_f/x\right)^{-1}}{\sigma_s} & \text{s-wave} \\ \frac{2x_f \left(1 - (x_f/x)^2\right)^{-1}}{\sigma_p} & \text{p-wave} \end{cases} \ . \tag{A.20}$$

The above equation illustrates how the comoving number density quickly approaches a constant values after freeze-out. This is only valid for the standard case of a radiation background. In the cosmological histories discussed in this work, we find that DM particles keep annihilating well after the number density has departed from its equilibrium value.

The current DM abundance is evaluated from the asymptotic value ($x \gg x_f$) of the comoving number density. This can be obtained by extrapolating Eq. (A.17) to very large values of x, and we find

$$Y_\chi^\infty = \frac{1}{A\, J(\infty)} = \frac{3\sqrt{5}}{2\sqrt{2}\,\pi} \frac{\left(\frac{\sigma_s}{x_f} + \frac{\sigma_p}{2x_f^2} \right)^{-1}}{g_*^{1/2}\, m_\chi M_{\rm Pl}} \ . \tag{A.21}$$

The first equality is general, whereas the second assumes the solutions in Eq. (A.20) for a partial wave expansion. The asymptotic number density scales as the inverse DM mass. In units of the critical density, the DM density results in

$$\Omega_\chi h^2 \equiv \frac{m_\chi Y_\chi^\infty \, s(T_0)}{\rho_{\rm cr}/h^2} = \frac{2 \times 10^8 \, {\rm GeV}^{-1}}{M_{\rm Pl} \, g_*^{1/2} \left(\frac{\sigma_s}{x_f} + \frac{\sigma_p}{2 x_f^2} \right)} \, . \tag{A.22}$$

This quantity depends on the DM mass only through the value of x_f.

Finally, we determine the value of the freeze-out temperature. This is the point where we match the two solutions in Eqs. (A.16) and (A.17). We define the freeze-out as temperature x_f by imposing $\Delta_\chi(x_f) = c \, Y_\chi^{\rm eq}(x_f)$, where c is an order one coefficient. We plug this definition into the Boltzmann equation (A.15), and the freeze-out condition is expressed as follows

$$\left. \frac{e^x \, x^{1/2}}{\langle \sigma v_{\rm rel} \rangle} \right|_{x=x_f} = \frac{c(c+2)}{c+1} \frac{3\sqrt{5}}{2 \, \pi^{5/2}} \frac{g_\chi}{g_*^{1/2}} \, m_\chi \, M_{\rm Pl} \, , \tag{A.23}$$

where we also restore the definition for A as in Eq. (A.14). We remind that the thermally averaged cross section can depend on x, as in the case of p-wave annihilation.

A.3.2 Non-Standard Cosmology Freeze-Out

For the modified cosmological backgrounds considered here, the DM number density evolution is still described by Eq. (2.16). However, the temperature dependence of the Hubble parameter is different. We introduce the quantity $x_r \equiv m_\chi / T_r$, where T_r was defined as the temperature where the energy of the

radiation bath reaches the one of ϕ. The Boltzmann equation now reads

$$\frac{dY_\chi}{dx} = -A\frac{\langle\sigma v_{\rm rel}\rangle}{x^{2-n/2}\left(x^n + x_r^n\right)^{1/2}}\left(Y_\chi^2 - Y_\chi^{\rm eq\,2}\right) \ , \tag{A.24}$$

where we use again the parameter A defined in Eq. (A.14).

We assume that freeze-out happens during the time of ϕ domination, namely $x_f \ll x_r$. At the freeze-out time, the Boltzmann equation can then be approximated by

$$\frac{dY_\chi}{dx} \simeq -A\frac{\langle\sigma v_{\rm rel}\rangle}{x^{2-n/2}\,x_r^{n/2}}\left(Y_\chi^2 - Y_\chi^{\rm eq\,2}\right) \ . \tag{A.25}$$

We solve again before and after freeze-out by using the convenient variable Δ_χ. At earlier times we neglect terms quadratic in Δ_χ and its derivative

$$Y_\chi(x) \simeq Y_\chi^{\rm eq}(x) + \frac{x^{2-n/2}x_r^{n/2}}{2A\langle\sigma v_{\rm rel}\rangle} \qquad (1 < x < x_f) \ . \tag{A.26}$$

After freeze-out, the solution takes the same form

$$Y_\chi(x) \simeq \left[\frac{1}{Y_\chi(x_f)} + A\,J_\phi(x)\right]^{-1} \qquad (x_f < x < x_r) \ . \tag{A.27}$$

This looks analogous to Eq. (A.17), but with the crucial difference that the annihilation integral reads

$$J_\phi(x) \equiv \frac{1}{x_r^{n/2}}\int_{x_f}^{x}\frac{\langle\sigma v_{\rm rel}\rangle}{x^{2-n/2}}dx \ . \tag{A.28}$$

We can perform the integral for partial wave expansion, and we find the expressions

$$J_\phi^{(\rm s)}(x) = \frac{\sigma_s}{x_r^{n/2}}\begin{cases} \frac{x_f^{n/2-1} - x^{n/2-1}}{1-n/2} & n \neq 2 \\ \log(x/x_f) & n = 2 \end{cases} \ , \tag{A.29}$$

and

$$J_\phi^{(\mathrm{p})}(x) = \frac{\sigma_p}{x_r^{n/2}} \begin{cases} \frac{x_f^{n/2-2} - x^{n/2-2}}{2-n/2} & n \neq 4 \\ \log(x/x_f) & n = 4 \end{cases} , \tag{A.30}$$

for s- and p-wave, respectively.

The solution in Eq. (A.27) can only be extrapolated up to $x = x_r$. Once the radiation bath dominates the energy density, we perform an additional matching, analogous to the one for standard freeze-out (see Eq. (A.17)). The subsequent evolution is described by

$$Y_\chi(x) \simeq \left[\frac{1}{Y_\chi(x_r)} + A\, J_{\mathrm{rad}}(x) \right]^{-1} \qquad (x > x_r) , \tag{A.31}$$

where define the annihilation integral now reads

$$J_{\mathrm{rad}}(x) \equiv \int_{x_r}^{x} \frac{\langle \sigma v_{\mathrm{rel}} \rangle}{x^2} dx . \tag{A.32}$$

The final DM density is $\rho_\chi(t_0) = m_\chi Y_\chi^\infty\, s(T_0)$, where the asymptotic value of the comoving density can be extracted by Eq. (A.31).

We conclude with the evaluation of the freeze-out temperature, defined as before by the condition $\Delta_\chi(x_f) = c\, Y_\chi^{\mathrm{eq}}(x_f)$. We find

$$\left. \frac{e^x\, x^{1/2}}{\langle \sigma v_{\mathrm{rel}} \rangle} \left(\frac{x_r}{x} \right)^{n/2} \right|_{x=x_f} = \frac{c(c+2)}{c+1} \frac{3\sqrt{5}}{2\,\pi^{5/2}} \frac{g_\chi}{g_*^{1/2}}\, m_\chi\, M_{\mathrm{Pl}} . \tag{A.33}$$

This relation is very similar to Eq. (A.33) with the important difference of a $(x_r/x)^{n/2}$ factor, which significantly enhances the left-hand side since we consider freeze-out during the ϕ domination phase ($x_f \ll x_r$). If we fix the DM mass and annihilation cross section, freeze-out must happen earlier with respect to the standard case.

Appendix B

Appendix

B.1 Collision Operators

The explicit expression for the collision operator $\mathcal{C}_\alpha$ appearing in the Boltzmann equation (3.1) depends on the specific freeze-in process α under consideration. In this Appendix, we derive its expression for the reactions considered in this work.

Bath particles always have an equilibrium phase space distribution $f^{\rm eq}_{B_i}(E,t)$ that depends on time and energy, under the assumptions that the universe is homogeneous and isotropic. Equilibrium number densities are defined as follows [131]

$$n^{\rm eq}_{B_i}(t) = g_{B_i} \int \frac{d^3p}{(2\pi)^3} f^{\rm eq}_{B_i}(E_{B_i}(|\boldsymbol{p}|),t) \ . \tag{B.1}$$

Here, g_{B_i} accounts for internal degrees of freedom (e.g. spin or color) and the dispersion relation reads

$$E_{B_i}(|\boldsymbol{p}|) = \sqrt{|\boldsymbol{p}|^2 + m^2_{B_i}} \ . \tag{B.2}$$

From now on, we leave the time dependence implicit. In the early universe we are always away from Bose condensation or Fermi degeneracy. This allows us to use $f_{B_i}^{\rm eq}(E_{B_i}) = \exp[-E_{B_i}/T]$ for both bosons and fermions in thermal equilibrium, and the number density of bath particles reads

$$n_{B_i}^{\rm eq} = \frac{g_{B_i}}{2\pi^2}\, m_{B_i}^2 T\, K_2[m_{B_i}/T] \ , \tag{B.3}$$

where K_2 is the modified Bessel function. Another useful quantity for the analysis of this Appendix is the Lorentz invariant phase space

$$d\Pi_{B_i} = \frac{d^3 p_i}{2E_{B_i}(2\pi)^3} \ . \tag{B.4}$$

B.1.1 Collision Operator for Decays

We start with the derivation of the collision operator for the decay processes considered in Sec. 3.3. The number density of χ can change both due to decays and inverse decays. Here, we only consider decays since DM particles never thermalize and the reaction goes only toward one direction. The collision operator is thus

$$\begin{aligned} \mathcal{C}_{B_1 \to B_2 \chi} = \int d\Pi_{B_1}\, d\Pi_{B_2}\, d\Pi_{\chi}\, f_{B_1}^{\rm eq}\, |\mathcal{M}_{B_1 \to B_2 \chi}|^2 \\ (2\pi)^4 \delta^4(p_{B_1} - p_{B_2} - p_X) \ . \end{aligned} \tag{B.5}$$

The decaying bath particles B_1 are in thermal equilibrium. It is important to emphasize here that the squared matrix element in the above equation in summed over initial *and* final states. In particular, we do not average over initial polarizations. We identify the *partial* decay width for the channel $B_1 \to B_2 \chi$ computed

in the rest frame of B_1 and we rewrite the collision operator [1]

$$\mathcal{C}_{B_1\to B_2\chi} = g_{B_1}\,\Gamma_{B_1\to B_2\chi}\int \frac{d^3p}{(2\pi)^3}\,\frac{m_{B_1}}{E_{B_1}}\,f^{\rm eq}_{B_1}\ . \tag{B.6}$$

We perform the last integration and we find

$$\mathcal{C}_{B_1\to B_2\chi} = n^{\rm eq}_{B_1}\,\Gamma_{B_1\to B_2\chi}\,\frac{K_1[m_{B_1}/T]}{K_2[m_{B_1}/T]}\ , \tag{B.7}$$

where the equilibrium number density of the decaying bath particle is given in Eq. (B.3).

B.1.2 Collision Operator for Scattering

The other freeze-in process we consider in this work is production via scattering. As done in Sec. 3.4, we distinguish between single and double production.

Single Production

For single production the collision operator reads

$$\begin{aligned}\mathcal{C}^{(a)}_{B_1B_2\to B_3\chi} = &\int d\Pi_{B_1}\,d\Pi_{B_2}\,d\Pi_{B_3}\,d\Pi_{\chi}\,f^{\rm eq}_{B_1}\,f^{\rm eq}_{B_2}\times\\ &|\mathcal{M}_{B_1B_2\to B_3\chi}|^2\,(2\pi)^4\delta^4(p_{B_1}+p_{B_2}-p_{B_3}-p_{\chi})\ .\end{aligned} \tag{B.8}$$

The initial state bath particles are in equilibrium and the squared matrix element is summer over both initial *and* final polarizations, without taking any average as before. Before we further develop the expression above, we observe that it can be

[1] The partial width $\Gamma_{B_1\to B_2\chi}$ can be different from the total width Γ_{B_1} if other decay channels for B_1 are allowed.

rewritten into an equivalent form. Conservation of energy enforces the equality

$$f_{B_1}^{\rm eq}\, f_{B_2}^{\rm eq} = \exp[-(E_{B_1}+E_{B_2})/T] = \\ \exp[-(E_{B_3}+E_{\chi})/T] = f_{B_3}^{\rm eq}\, f_{\chi}^{\rm eq}\ . \tag{B.9}$$

Moreover, if we assume CP invariance, we have the equality between the squared matrix elements

$$|\mathcal{M}_{B_1 B_2 \to B_3 \chi}|^2 = |\mathcal{M}_{B_3 \chi \to B_1 B_2}|^2 \tag{B.10}$$

Putting these two results together, we have

$$\mathcal{C}^{(b)}_{B_1 B_2 \to B_3 \chi} = \int d\Pi_{B_3}\, d\Pi_{\chi}\, d\Pi_{B_1}\, d\Pi_{B_2}\ f_{B_3}^{\rm eq}\, f_{\chi}^{\rm eq} \times \\ |\mathcal{M}_{B_3 \chi \to B_1 B_2}|^2\, (2\pi)^4 \delta^4(p_{B_3}+p_{\chi}-p_{B_1}-p_{B_2})\ . \tag{B.11}$$

The expressions in Eqs. (B.8) and (B.11) are equivalent forms for the collision operator and they give the same result. In spite of $f_{\chi}^{\rm eq}$ appearing in the second one, DM particles never reach thermal equilibrium. Conservation of energy as expressed in Eq. (B.9) brings $f_{\chi}^{\rm eq}$ into the game, but we are still averaging over initial state bath particles. Although the two expressions are equivalent, it is computationally advantageous to use the one for the reaction allowed at zero kinetic energy: in other words, if $m_{B_1}+m_{B_2} > m_{B_3}+m_{\chi}$ we use Eq. (B.8), otherwise Eq. (B.11). This strategy isolates thermal suppressions in the distribution functions rather than phase space integrals. In what follows, we develop both expressions.

We present the derivation starting from Eq. (B.8); the one correspondent to the definition in Eq. (B.11) is analogous. We define the Lorentz invariant relative

velocity between the two initial state particles

$$v_{B_1B_2} \equiv \frac{\sqrt{(p_{B_1} \cdot p_{B_2})^2 - m_{B_1}^2 m_{B_2}^2}}{p_{B_1} \cdot p_{B_2}} \ . \tag{B.12}$$

Here, p_{B_i} (with $i = 1, 2$) are Lorentz four-vectors denoting initial state four-momenta, and the only consider Lorentz invariant products. Once we put particles on-shell ($p_{B_i}^2 = m_{B_i}^2$), the relative velocity reads

$$v_{B_1B_2} = \frac{\lambda^{1/2}(s, m_{B_1}, m_{B_2})}{2\, p_{B_1} \cdot p_{B_2}} \ , \tag{B.13}$$

where we introduce the (square of the) center of mass energy $s = (p_{B_1} + p_{B_2})^2$ and we define the function

$$\lambda(x, y, z) \equiv [x - (y + z)^2][x - (y - z)^2] \ . \tag{B.14}$$

The Lorentz invariant cross section for each individual binary collision is defined as it follows [132]

$$\begin{aligned} \sigma_{B_1B_2 \to B_3\chi}(s) = & \frac{1}{g_{B_1} g_{B_2}} \frac{1}{4\, p_{B_1} \cdot p_{B_2}\, v_{B_1B_2}} \\ & \int d\Pi_{B_3}\, d\Pi_\chi \ |\mathcal{M}_{B_1B_2 \to B_3\chi}|^2 \\ & (2\pi)^4 \delta^4(p_{B_1} + p_{B_2} - p_{B_3} - p_\chi) \ . \end{aligned} \tag{B.15}$$

According to our conventions, the squared matrix element appearing in Eq. (B.8) is only summed over initial states, and this is why we divided the expression above by an overall factor of $g_{B_1} g_{B_2}$. This allows us to express the collision operator in

Eq. (B.8) in terms of a thermally averaged cross section

$$\begin{aligned}\mathcal{C}^{(a)}_{B_1B_2\to B_3\chi} = 2g_{B_1}g_{B_2}\int d\Pi_{B_1}\, d\Pi_{B_2}\, f^{\rm eq}_{B_1}\, f^{\rm eq}_{B_2} \\ \lambda^{1/2}(s, m_{B_1}, m_{B_2})\sigma_{B_1B_2\to B_3\chi}(s)\ ,\end{aligned} \tag{B.16}$$

where we use Eq. (B.13) for the relative velocity.

The last task left for us is the phase space integration. The integrand depends only on the energies E_{B_1} and E_{B_2} and on s, thus the only non-trivial angular integration is the one over the angle θ between the initial momenta. The integration over the remaining angles is straightforward. After plugging in the definition in Eq. (B.4), the integration measure reads

$$\begin{aligned}d\Pi_{B_1}\, d\Pi_{B_2} = \frac{|p_{B_1}|^2\, d|p_{B_1}|\, d\Omega_{B_1}}{16\pi^3 E_{B_1}}\frac{|p_{B_2}|^2\, d|p_{B_2}|\, d\Omega_{B_2}}{16\pi^3 E_{B_2}} = \\ \frac{|p_{B_1}|\,|p_{B_2}|}{32\pi^4}\, dE_{B_1} dE_{B_2} d\cos\theta\ ,\end{aligned} \tag{B.17}$$

where in the second row we perform the straightforward integration over the angles and we we use the dispersion relation in Eq. (B.2). In order to proceed, it is convenient to use the following variables [11]

$$E_+ = E_{B_1} + E_{B_2}\ , \tag{B.18}$$

$$E_- = E_{B_1} - E_{B_2}\ , \tag{B.19}$$

$$\begin{aligned}s = m^2_{B_1} + m^2_{B_2} + \\ 2\left(E_{B_1}E_{B_2} - |p_{B_1}||p_{B_2}|\cos\theta\right)\ .\end{aligned} \tag{B.20}$$

The Jacobian for this transformation reads

$$dE_{B_1} dE_{B_2} d\cos\theta = \frac{dE_+ dE_- ds}{4|p_{B_1}||p_{B_2}|}\ , \tag{B.21}$$

and the integration measure expressed in terms of the new variables takes a much simpler form

$$d\Pi_{B_1}\, d\Pi_{B_2} = \frac{dE_+ dE_- ds}{128\pi^4}\ . \tag{B.22}$$

Before computing the integral, we need to identify the integration domain. The Mandelstam variables s is bound to be in the region

$$s \geq s_{12}^{\min} \equiv (m_{B_1} + m_{B_2})^2\ . \tag{B.23}$$

Once we fix s, the variable E_+ can take the values

$$E_+ = \sqrt{s - \left(\boldsymbol{p}_{B_1} + \boldsymbol{p}_{B_2}\right)^2} \geq \sqrt{s}\ . \tag{B.24}$$

The allowed values for E_- are found after imposing that the absolute value of $\cos\theta$ as expressed in Eq. (B.20) is always smaller than one. We find the range

$$\frac{\left|E_- - E_+ \frac{(m_{B_1}^2 - m_{B_2}^2)}{s}\right|}{\left(E_+^2 - s\right)^{1/2}} \leq \frac{\lambda^{1/2}(s, m_{B_1}, m_{B_2})}{s}\ . \tag{B.25}$$

Finally, we perform the integrations. The product $f_{B_1}^{\rm eq}\, f_{B_2}^{\rm eq} = \exp[-E_+/T]$ depends only on E_+, therefore we can always perform the integration over dE_-

$$\begin{aligned} \mathcal{C}^{(a)}_{B_1 B_2 \to B_3 \chi} &= \frac{g_{B_1} g_{B_2}}{32\pi^4} \times \\ &\int_{s_{12}^{\min}}^{\infty} ds\, \frac{\lambda(s, m_{B_1}, m_{B_2})}{s}\, \sigma_{B_1 B_2 \to B_3 \chi}(s) \\ &\int_{\sqrt{s}}^{\infty} dE_+ \exp[-E_+/T] \left(E_+^2 - s\right)^{1/2}\ . \end{aligned} \tag{B.26}$$

The integral over dE_+ gives a Bessel function

$$\begin{aligned}\mathcal{C}^{(a)}_{B_1B_2\to B_3\chi} &= \frac{g_{B_1}g_{B_2}}{32\pi^4}\,T\times \\ &\int_{s_{12}^{\min}}^{\infty} ds\,\frac{\lambda(s,m_{B_1},m_{B_2})}{s^{1/2}}\,\sigma_{B_1B_2\to B_3\chi}(s)\,K_1[\sqrt{s}/T]\ .\end{aligned} \tag{B.27}$$

This is our final expression. The last integral over s can be performed only after we specify the explicit cross section, and it is in general model dependent.

We conclude with two additional results. First, we quote the final expression for the collision operator as defined in Eq. (B.11). After a similar derivation to the decay case, we find

$$\begin{aligned}\mathcal{C}^{(b)}_{B_1B_2\to B_3\chi} &= \frac{g_{B_3}g_{\chi}}{32\pi^4}\,T\times \\ &\int_{s_{3\chi}^{\min}}^{\infty} ds\,\frac{\lambda(s,m_{B_3},m_{\chi})}{s^{1/2}}\,\sigma_{B_3\chi\to B_1B_2}(s)\,K_1[\sqrt{s}/T]\ ,\end{aligned} \tag{B.28}$$

where this time $s_{3\chi}^{\min}=(m_{B_3}+m_{\chi})^2$. Second, we introduce a compact form to express the collision operator

$$\mathcal{C}^{(a)}_{B_1B_2\to B_3\chi} = \langle\sigma_{B_1B_2\to B_3\chi}v\rangle\,n^{\rm eq}_{B_1}n^{\rm eq}_{B_2}\ , \tag{B.29}$$

$$\mathcal{C}^{(b)}_{B_1B_2\to B_3\chi} = \langle\sigma_{B_3\chi\to B_1B_2}v\rangle\,n^{\rm eq}_{B_3}n^{\rm eq}_{\chi}\ , \tag{B.30}$$

as a combination of equilibrium number densities and a thermally averaged cross section. The explicit forms for the latter can be obtained by identifying the

equilibrium distribution as defined in Eq. (B.3), and they result in

$$\langle \sigma_{B_1 B_2 \to B_3 \chi} v \rangle = \frac{1}{8\, K_2[m_{B_1}/T] K_2[m_{B_2}/T]\, m_{B_1}^2 m_{B_2}^2 T} \int_{s_{12}^{\min}}^{\infty} ds \frac{\lambda(s, m_{B_1}, m_{B_2})}{s^{1/2}} \sigma_{B_1 B_2 \to B_3 \chi}(s) K_1[\sqrt{s}/T] \ . \tag{B.31}$$

$$\langle \sigma_{B_3 \chi \to B_1 B_2} v \rangle = \frac{1}{8\, K_2[m_{B_3}/T] K_2[m_{\chi}/T]\, m_{B_3}^2 m_{\chi}^2 T} \int_{s_{3\chi}^{\min}}^{\infty} ds \frac{\lambda(s, m_{B_3}, m_{\chi})}{s^{1/2}} \sigma_{B_3 \chi \to B_1 B_2}(s) K_1[\sqrt{s}/T] \ . \tag{B.32}$$

The equality between the collision operators expressed as in Eqs. (B.8) and (B.11) can be also written as

$$\langle \sigma_{B_1 B_2 \to B_3 \chi} v \rangle \, n_{B_1}^{\rm eq} n_{B_2}^{\rm eq} = \langle \sigma_{B_3 \chi \to B_1 B_2} v \rangle \, n_{B_3}^{\rm eq} n_{\chi}^{\rm eq} \ . \tag{B.33}$$

Pair Production

The collision operator for the case of DM pair production can be derived by employing similar techniques. As usual, the collision operator can be written in two equivalent forms. Here, we report the final results

$$\mathcal{C}^{(a)}_{B_1 B_2 \to \chi\chi} = \frac{g_{B_1} g_{B_2}}{32\pi^4}\, T \times \int_{s_{12}^{\min}}^{\infty} ds\, \frac{\lambda(s, m_{B_1}, m_{B_2})}{s^{1/2}}\, \sigma_{B_1 B_2 \to \chi\chi}(s)\, K_1[\sqrt{s}/T] \ . \tag{B.34}$$

$$\mathcal{C}^{(b)}_{B_1 B_2 \to \chi\chi} = \frac{g_{\chi}^2}{32\pi^4}\, T \times \int_{s_{\chi\chi}^{\min}}^{\infty} ds\, \frac{\lambda(s, m_{\chi}, m_{\chi})}{s^{1/2}}\, \sigma_{\chi\chi \to B_1 B_2}(s)\, K_1[\sqrt{s}/T] \ . \tag{B.35}$$

As already done before, we give expressions for both cases of direct and inverse reactions. We can also write the collision operators in the form

$$\mathcal{C}^{(a)}_{B_1B_2\to\chi\chi} = \langle\sigma_{B_1B_2\to\chi\chi}v\rangle\, n^{\rm eq}_{B_1} n^{\rm eq}_{B_2} \ , \tag{B.36}$$

$$\mathcal{C}^{(b)}_{B_1B_2\to\chi\chi} = \langle\sigma_{\chi\chi\to B_1B_2}v\rangle\, n^{\rm eq}_{\chi} n^{\rm eq}_{\chi} \ , \tag{B.37}$$

where the thermally averaged cross sections result in

$$\langle\sigma_{B_1B_2\to\chi\chi}v\rangle = \frac{1}{8\,K_2[m_{B_1}/T]K_2[m_{B_2}/T]\,m^2_{B_1}m^2_{B_2}T} \int_{s^{\rm min}_{12}}^{\infty} ds \frac{\lambda(s,m_{B_1},m_{B_2})}{s^{1/2}}\sigma_{B_1B_2\to\chi\chi}(s)K_1[\sqrt{s}/T] \ , \tag{B.38}$$

$$\langle\sigma_{\chi\chi\to B_1B_2}v\rangle = \frac{1}{8\,K_2[m_{\chi}/T]^2\,m^4_{\chi}T} \int_{s^{\rm min}_{\chi\chi}}^{\infty} ds \frac{\lambda(s,m_{\chi},m_{\chi})}{s^{1/2}}\sigma_{\chi\chi\to B_1B_2}(s)K_1[\sqrt{s}/T] \ . \tag{B.39}$$

Some Limiting Expressions

All results derived in this Appendix so far did not rely upon any approximation. Here, we conclude by providing some limiting expressions that are useful for the analytical estimates found in this work. The scattering analysis in Sec. 3.4 always assumes a constant matrix element for the collision. In other words, we always consider matrix element independent on the kinematics. Within this assumption, the cross section for binary collisions in Eq. (B.15) can be immediately computed because the phase space integral is straightforward.

For single DM production, and within this assumption, the binary cross section reads

$$\sigma_{B_1B_2\to B_3\chi}(s) = \frac{|\mathcal{M}_{B_1B_2\to B_3\chi}|^2}{g_{B_1}g_{B_2}\,16\pi s}\frac{\lambda^{1/2}(s,m_{B_3},m_{\chi})}{\lambda^{1/2}(s,m_{B_1},m_{B_2})} \ . \tag{B.40}$$

Likewise, the cross section for the inverse reaction reads

$$\sigma_{B_3\chi\to B_1B_2}(s) = \frac{|\mathcal{M}_{B_3\chi\to B_1B_2}|^2}{g_{B_3}g_\chi\, 16\pi s}\frac{\lambda^{1/2}(s,m_{B_1},m_{B_2})}{\lambda^{1/2}(s,m_{B_3},m_\chi)}\ . \tag{B.41}$$

The collision operator can be computed from Eqs. (B.27) or (B.28). Both expressions give the same result

$$\begin{aligned}&\mathcal{C}^{(a)}_{B_1B_2\to B_3\chi} = \mathcal{C}^{(b)}_{B_1B_2\to B_3\chi} = \\ &\frac{|\mathcal{M}_{B_1B_2\to B_3\chi}|^2\ T}{512\pi^5}\int_{s^{\rm min}_{\rm single}}^{\infty}\frac{ds}{s^{3/2}}\,K_1[\sqrt{s}/T]\times \\ &\lambda^{1/2}(s,m_{B_1},m_{B_2})\lambda^{1/2}(s,m_{B_3},m_\chi)\ ,\end{aligned} \tag{B.42}$$

where the lower integration limit is set by the kinematical threshold for the reaction $s^{\rm min}_{\rm single} = \max\left\{s^{\rm min}_{12}, s^{\rm min}_{3\chi}\right\}$. The remaining integral depends on the spectrum of the model and it can be computed numerically.

For DM pair production, an analogous calculation leads to the result

$$\begin{aligned}&\mathcal{C}^{(a)}_{B_1B_2\to\chi\chi} = \mathcal{C}^{(b)}_{B_1B_2\to\chi\chi} = \\ &\frac{|\mathcal{M}_{B_1B_2\to\chi\chi}|^2\ T}{512\pi^5}\int_{s^{\rm min}_{\rm pair}}^{\infty}\frac{ds}{s^{3/2}}\,K_1[\sqrt{s}/T]\times \\ &\lambda^{1/2}(s,m_{B_1},m_{B_2})\lambda^{1/2}(s,m_\chi,m_\chi)\ ,\end{aligned} \tag{B.43}$$

where this time $s^{\rm min}_{\rm pair} = \max\left\{s^{\rm min}_{12}, s^{\rm min}_{\chi\chi}\right\}$.

Appendix C

Appendix

C.1 Priors

In this Appendix we derive the probability distribution for $\chi_{\rm eff}$ for general given *spin magnitude* and *angular* distributions. Subsequently, we show how the distribution for $\chi_{\rm eff}$ differs when we relax some assumptions that we employed in our calculations, specifically the assumption that the merging black holes have the same mass, and the assumption of perfect alignment between the individual spin and the orbital angular momentum for the "aligned" models.

Let us define the direction of the orbital angular momentum as the direction of the z-axis, then $\chi_{\rm eff}$ can be re-written as

$$\chi_{\rm eff} = \frac{\chi_1^z + q\chi_2^z}{1+q}, \tag{C.1}$$

where q is the mass ratio m_2/m_1 such that $0 \leq q \leq 1$, and $\chi_i^z = \chi_i \cos\theta_i$ is the individual spin component along the z-axis. Our goal is to derive the distribution for χ_i^z and the probability distribution for the sum $\chi_1^z + q\chi_2^z$.

First, the distribution of the product for χ_i^z is given by the following integral

over probability distributions

$$p(\chi_i^z) = \int_0^1 f_{\chi_i}(\chi_i)\,\mathrm{d}\chi_i \int_{-1}^1 f_{\cos\theta_i}(\cos\theta_i)\,\delta(\chi_i^z - \chi_i\,\cos\theta_i)\,\mathrm{d}\cos\theta_i, \tag{C.2}$$

where the probability density functions f_{χ_i} is just the spin magnitude distribution, as given, for example, for PBH in Eq. (4.4), and where $f_{\cos\theta_i}$ is the distribution for the cosine of θ_i (θ_i is defined under Eq. (4.2)). For instance, if the angular distribution is isotropic the $p(\chi^z)$ distribution reads as

$$p(\chi_i^z) = \frac{1}{2}\int_{|\chi_i^z|}^1 f_{\chi_i}(\chi_i^z/\cos\theta_i)\frac{1}{|\cos\theta_i|}\mathrm{d}\cos\theta_i. \tag{C.3}$$

Using the probability distribution for χ_i^z, and assuming that the individual spins are independent of each other, we find that the probability distribution for $\chi_{\rm eff}$ is given by the following convolution of the distributions

$$\begin{aligned} p\left(\chi_{\rm eff}\right) &= \int_{-1}^1 \mathrm{d}\chi_1^z \int_{-1}^1 \delta\left(\chi_{\rm eff} - \frac{(\chi_1^z + q\chi_2^z)}{(1+q)}\right) p\left(\chi_1^z\right) p\left(\chi_2^z\right) \mathrm{d}\chi_2^z \\ &= (1+q)\int_a^b p\left(\chi_2^z\right) p\left((1+q)\chi_{\rm eff} - q\chi_2^z\right) \mathrm{d}\chi_2^z\,, \end{aligned} \tag{C.4}$$

where the extrema of integration read

$$\begin{aligned} a &= \max\left(-1, \frac{(1+q)\chi_{\rm eff} - 1}{q}\right) \\ b &= \min\left(1, \frac{(1+q)\chi_{\rm eff} + 1}{q}\right). \end{aligned} \tag{C.5}$$

In general, there is no analytic solution for the probability density, and we have to perform the integration numerically to solve for the distribution.

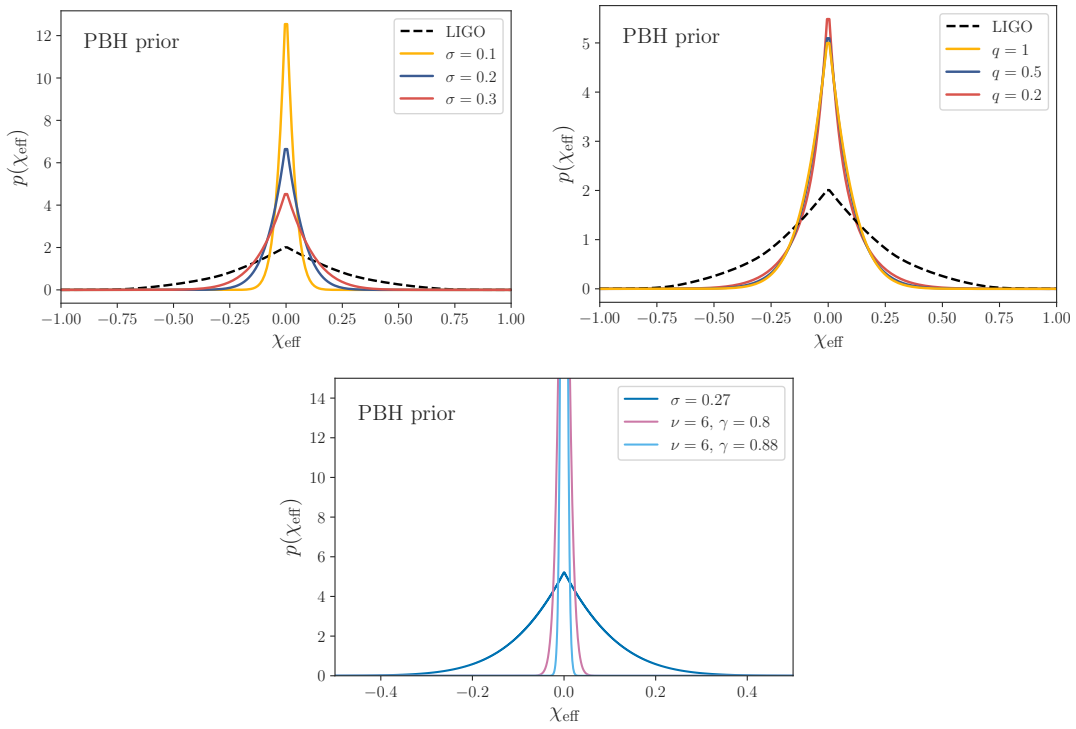

Figure C.1: *Top left*: Prior distribution for $\chi_{\rm eff}$ used in LIGO analysis and for the PBH model with various values of σ. *Top right*: Prior distribution for $\chi_{\rm eff}$ for different mass ratios $q = 1$, $q = 0.5$ and $q = 0.2$. *Bottom*: Prior distribution for $\chi_{\rm eff}$ for different PBH spin distribution (see sec. 4.2.2 for details).

C.1.1 PBH

In figure C.1, we compare the LIGO prior distribution with the results for the prior distribution for $\chi_{\rm eff}$ for our PBH models, for various values of $\sigma = 0.1$, 0.2 and 0.3 (top left) and of the mass ratio q (top right). By allowing the width to vary we get a sense of how sensitive is the PBH distribution with respect to σ is.

The top right panel, instead, illustrates how the choice of q has a very marginal impact on the functional shape of the predicted prior distribution. Notice that all events reported by LIGO have a median value of the mass ratio q larger than 0.5 and larger than 0.2 at 90% credible interval (figure 5 on ref. [2]), which is why we focus on relatively large mass ratios, $q = 0.2$, 0.5 and 1.0.

Finally, the bottom panel shows our benchmark $q = 1$ and $\sigma = 0.27$ PBH prior distribution with what is predicted in the models of Ref. [3]. Notice that as illustrated in Fig. 5 of Ref. [3], the relevant value for $\nu \simeq 6$ for masses in the 10 $M_\odot$ range, while the choice of γ reflects the prediction for a nearly flat power spectrum ($\gamma = 0.88$) and a slightly smaller value, which could result from e.g. a broader power spectrum (see e.g. their Fig. 6, left panel).

C.1.2 Benchmark spin models

Here we study the systematic dependence of the prior distribution for $\chi_{\rm eff}$ on the values of the mass ratio q (Fig. C.2, top panels) and on the assumption of perfect alignment (bottom panel).

The top left panel shows how the LI, FI and HI prior distributions change when switching to our benchmark value of $q = 1$ (equal mass ratio) to $q = 0.5$. The top right panel does the same for the aligned models LA and FA. It is clear that the changes for the isotropic models is very small, while for the aligned models there is a slight but noticeable effect near the peak of the distribution for the FA model, and a slight shift in the peak location for the LA model. For the aligned models, as the mass ratio starts to get more extreme, the distribution for $\chi_{\rm eff}$ begins to resemble the distribution for the spin magnitude.

The bottom panel of Fig. C.2 shows how the prior distributions for the LA and FA models change when the assumption of perfect BH spin-orbit is relaxed. If the BBH is formed via classical isolated binary evolution with an initial perfect alignment, large values for the misalignment angle are required to be consistent with the GW151226 event [133], but the natal kicks necessary to explain this large misalignments usually exceed the typical values for binary evolution models. Therefore, the distribution of the tilt angle is taken to be flat from 0 up to 35°,

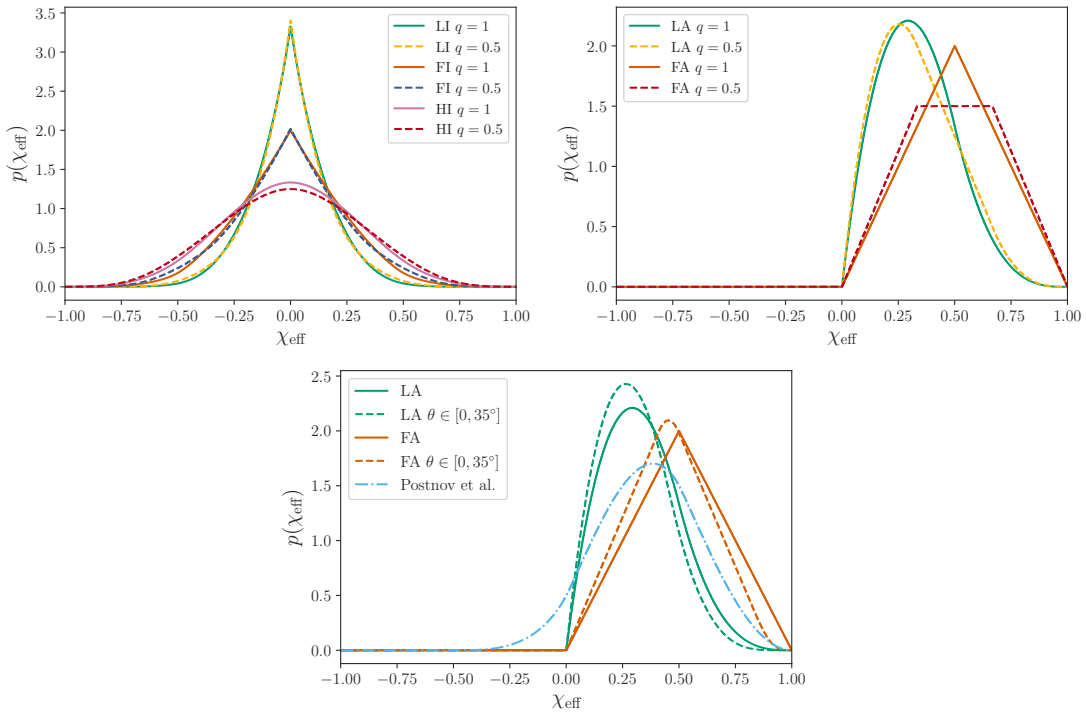

Figure C.2: Distribution of $\chi_{\rm eff}$ for different mass ratios q for the isotropic (*top left*) and aligned (*top right*) models with $q = 1$ and $q = 0.5$. *Bottom*: the distribution of $\chi_{\rm eff}$ when the assumption of perfect alignment is relaxed for the aligned models (green and orange) and BBH efrom massive isolated binaries through common envelope evolution with randomly misaligned initial spin (blue dash-dotted line) [134].

and thus the maximal angle is within the region suggested by Ref. [133]. The figure shows that the prior distribution is hardly affected at all, with the only noticeable change being a shift of the peak distribution to slightly lower values of $\chi_{\rm eff}$.

Finally, we consider the scenario of binary BH evolution from isolated massive binary systems studied in Ref. [134]; in this scenario $\chi_{\rm eff}$ can take negative values because of effects such as initially misaligned binary components spins; while other effects such as mass exchange, tidal interaction, and common envelope evolution tend to align the spins, the resulting distribution for $\chi_{\rm eff}$ was found to range between -0.2 and 0,8, thus encompassing negative values (see their Figure 11). To mimic this physical situation, here we assumed (following what shown in fig. 8 of Ref. [134]) that one black hole has a spin orientation that is isotropic compared to the orbital angular momentum, and has low intrinsic spin magnitude distribution; for the second black hole, we assumed perfect alignment, and a flat intrinsic spin magnitude distribution. The resulting $\chi_{\rm eff}$ distribution is shown in Fig. C.2 with a dot-dashed light-blue line; our results reflect qualitatively the range for $\chi_{\rm eff}$ found in Ref. [134]. We calculated the resulting odds ratio for this setup, and found that compared to the benchmark LI model, the odd ratio is of -6.04, thus comparable to what we found for the LA model.

Bibliography

[1] K. Griest and M. Kamionkowski, *Unitarity Limits on the Mass and Radius of Dark Matter Particles*, *Phys. Rev. Lett.* **64** (1990) 615.

[2] LIGO Scientific, Virgo collaboration, B. P. Abbott et al., *GWTC-1: A Gravitational-Wave Transient Catalog of Compact Binary Mergers Observed by LIGO and Virgo during the First and Second Observing Runs*, 1811.12907.

[3] V. De Luca, V. Desjacques, G. Franciolini, A. Malhotra and A. Riotto, *The Initial Spin Probability Distribution of Primordial Black Holes*, 1903.01179.

[4] LIGO Scientific, Virgo collaboration, B. P. Abbott et al., *Binary Black Hole Population Properties Inferred from the First and Second Observing Runs of Advanced LIGO and Advanced Virgo*, 1811.12940.

[5] G. Jungman, M. Kamionkowski and K. Griest, *Supersymmetric dark matter*, *Phys. Rept.* **267** (1996) 195 [hep-ph/9506380].

[6] G. Bertone, D. Hooper and J. Silk, *Particle dark matter: Evidence, candidates and constraints*, *Phys. Rept.* **405** (2005) 279 [hep-ph/0404175].

[7] J. L. Feng, *Dark Matter Candidates from Particle Physics and Methods of Detection*, *Ann. Rev. Astron. Astrophys.* **48** (2010) 495 [1003.0904].

[8] B. W. Lee and S. Weinberg, *Cosmological Lower Bound on Heavy Neutrino Masses*, *Phys. Rev. Lett.* **39** (1977) 165.

[9] R. J. Scherrer and M. S. Turner, *On the Relic, Cosmic Abundance of Stable Weakly Interacting Massive Particles*, *Phys. Rev.* **D33** (1986) 1585.

[10] M. Srednicki, R. Watkins and K. A. Olive, *Calculations of Relic Densities in the Early Universe*, *Nucl. Phys.* **B310** (1988) 693.

[11] P. Gondolo and G. Gelmini, *Cosmic abundances of stable particles: Improved analysis*, *Nucl. Phys.* **B360** (1991) 145.

[12] M. Kawasaki, K. Kohri and N. Sugiyama, *MeV scale reheating temperature and thermalization of neutrino background*, *Phys. Rev.* **D62** (2000) 023506 [astro-ph/0002127].

[13] K. Ichikawa, M. Kawasaki and F. Takahashi, *The Oscillation effects on thermalization of the neutrinos in the Universe with low reheating temperature*, *Phys. Rev.* **D72** (2005) 043522 [astro-ph/0505395].

[14] J. McDonald, *WIMP Densities in Decaying Particle Dominated Cosmology*, *Phys. Rev.* **D43** (1991) 1063.

[15] M. Kamionkowski and M. S. Turner, *THERMAL RELICS: DO WE KNOW THEIR ABUNDANCES?*, *Phys. Rev.* **D42** (1990) 3310.

[16] D. J. H. Chung, E. W. Kolb and A. Riotto, *Production of massive particles during reheating*, *Phys. Rev.* **D60** (1999) 063504 [hep-ph/9809453].

[17] G. F. Giudice, E. W. Kolb and A. Riotto, *Largest temperature of the radiation era and its cosmological implications*, *Phys. Rev.* **D64** (2001) 023508 [hep-ph/0005123].

[18] T. Moroi and L. Randall, *Wino cold dark matter from anomaly mediated SUSY breaking*, *Nucl. Phys.* **B570** (2000) 455 [hep-ph/9906527].

[19] R. Allahverdi and M. Drees, *Production of massive stable particles in inflaton decay*, *Phys. Rev. Lett.* **89** (2002) 091302 [hep-ph/0203118].

[20] R. Allahverdi and M. Drees, *Thermalization after inflation and production of massive stable particles*, *Phys. Rev.* **D66** (2002) 063513 [hep-ph/0205246].

[21] B. S. Acharya, G. Kane, S. Watson and P. Kumar, *A Non-thermal WIMP Miracle*, *Phys. Rev.* **D80** (2009) 083529 [0908.2430].

[22] A. Monteux and C. S. Shin, *Thermal Goldstino Production with Low Reheating Temperatures*, *Phys. Rev.* **D92** (2015) 035002 [1505.03149].

[23] R. T. Co, F. D'Eramo, L. J. Hall and D. Pappadopulo, *Freeze-In Dark Matter with Displaced Signatures at Colliders*, *JCAP* **1512** (2015) 024 [1506.07532].

[24] H. Davoudiasl, D. Hooper and S. D. McDermott, *Inflatable Dark Matter*, *Phys. Rev. Lett.* **116** (2016) 031303 [1507.08660].

[25] R. T. Co, F. D'Eramo and L. J. Hall, *SaxiGUTs and their Predictions*, *Phys. Rev.* **D94** (2016) 075001 [1603.04439].

[26] R. T. Co, F. D'Eramo and L. J. Hall, *Gravitino or Axino Dark Matter with Reheat Temperature as high as* 10^{16} *GeV*, *JHEP* **03** (2017) 005 [1611.05028].

[27] R. H. Cyburt, B. D. Fields, K. A. Olive and T.-H. Yeh, *Big Bang Nucleosynthesis: 2015*, *Rev. Mod. Phys.* **88** (2016) 015004 [1505.01076].

[28] Planck collaboration, P. A. R. Ade et al., *Planck 2015 results. XIII. Cosmological parameters*, *Astron. Astrophys.* **594** (2016) A13 [1502.01589].

[29] R. R. Caldwell, R. Dave and P. J. Steinhardt, *Cosmological imprint of an energy component with general equation of state*, *Phys. Rev. Lett.* **80** (1998) 1582 [astro-ph/9708069].

[30] V. Sahni and A. A. Starobinsky, *The Case for a positive cosmological Lambda term*, *Int. J. Mod. Phys.* **D9** (2000) 373 [astro-ph/9904398].

[31] P. Salati, *Quintessence and the relic density of neutralinos*, *Phys. Lett.* **B571** (2003) 121 [astro-ph/0207396].

[32] S. Profumo and P. Ullio, *SUSY dark matter and quintessence*, *JCAP* **0311** (2003) 006 [hep-ph/0309220].

[33] S. Dodelson and M. S. Turner, *Nonequilibrium neutrino statistical mechanics in the expanding universe*, *Phys. Rev.* **D46** (1992) 3372.

[34] B. Ratra and P. J. E. Peebles, *Cosmological Consequences of a Rolling Homogeneous Scalar Field*, *Phys. Rev.* **D37** (1988) 3406.

[35] C. Wetterich, *Cosmology and the Fate of Dilatation Symmetry*, *Nucl. Phys.* **B302** (1988) 668.

[36] A. Yu. Kamenshchik, U. Moschella and V. Pasquier, *An Alternative to quintessence*, *Phys. Lett.* **B511** (2001) 265 [gr-qc/0103004].

[37] P.-H. Chavanis, *Cosmology with a stiff matter era*, *Phys. Rev.* **D92** (2015) 103004 [1412.0743].

[38] J. Khoury, B. A. Ovrut, P. J. Steinhardt and N. Turok, *The Ekpyrotic universe: Colliding branes and the origin of the hot big bang*, *Phys. Rev.* **D64** (2001) 123522 [hep-th/0103239].

[39] K. Choi, *String or M theory axion as a quintessence*, *Phys. Rev.* **D62** (2000) 043509 [hep-ph/9902292].

[40] C. L. Gardner, *Quintessence and the transition to an accelerating universe*, *Nucl. Phys.* **B707** (2005) 278 [astro-ph/0407604].

[41] C. Armendariz-Picon, T. Damour and V. F. Mukhanov, *k - inflation*, *Phys. Lett.* **B458** (1999) 209 [hep-th/9904075].

[42] A. J. Christopherson and K. A. Malik, *The non-adiabatic pressure in general scalar field systems*, *Phys. Lett.* **B675** (2009) 159 [0809.3518].

[43] T. R. Slatyer, *Indirect dark matter signatures in the cosmic dark ages. I. Generalizing the bound on s-wave dark matter annihilation from Planck results*, *Phys. Rev.* **D93** (2016) 023527 [1506.03811].

[44] Fermi-LAT collaboration, M. Ackermann et al., *Searching for Dark Matter Annihilation from Milky Way Dwarf Spheroidal Galaxies with Six Years of Fermi Large Area Telescope Data*, *Phys. Rev. Lett.* **115** (2015) 231301 [1503.02641].

[45] L. J. Hall, K. Jedamzik, J. March-Russell and S. M. West, *Freeze-In Production of FIMP Dark Matter*, *JHEP* **03** (2010) 080 [0911.1120].

[46] V. S. Rychkov and A. Strumia, *Thermal production of gravitinos*, *Phys. Rev.* **D75** (2007) 075011 [hep-ph/0701104].

[47] A. Strumia, *Thermal production of axino Dark Matter*, *JHEP* **06** (2010) 036 [1003.5847].

[48] S. Hamdan and J. Unwin, *Dark Matter Freeze-out During Matter Domination*, 1710.03758.

[49] F. D'Eramo, N. Fernandez and S. Profumo, *When the Universe Expands Too Fast: Relentless Dark Matter*, *JCAP* **1705** (2017) 012 [1703.04793].

[50] B. Dutta, E. Jimenez and I. Zavala, *D-brane Disformal Coupling and Thermal Dark Matter*, 1708.07153.

[51] N. Bernal, M. Heikinheimo, T. Tenkanen, K. Tuominen and V. Vaskonen, *The Dawn of FIMP Dark Matter: A Review of Models and Constraints*, *Int. J. Mod. Phys.* **A32** (2017) 1730023 [1706.07442].

[52] R. T. Co, F. D'Eramo, L. J. Hall and K. Harigaya, *Saxion Cosmology for Thermalized Gravitino Dark Matter*, *JHEP* **07** (2017) 125 [1703.09796].

[53] K. Redmond and A. L. Erickcek, *New Constraints on Dark Matter Production during Kination*, *Phys. Rev.* **D96** (2017) 043511 [1704.01056].

[54] L. Visinelli, *(Non-)thermal production of WIMPs during kination*, 1710.11006.

[55] J. De-Santiago and J. L. Cervantes-Cota, *Generalizing a Unified Model of Dark Matter, Dark Energy, and Inflation with Non Canonical Kinetic Term*, *Phys. Rev.* **D83** (2011) 063502 [1102.1777].

[56] K. Dimopoulos and C. Owen, *Quintessential Inflation with α-attractors*, 1703.00305.

[57] K. Rajagopal, M. S. Turner and F. Wilczek, *Cosmological implications of axinos*, *Nucl. Phys.* **B358** (1991) 447.

[58] L. Covi, J. E. Kim and L. Roszkowski, *Axinos as cold dark matter*, *Phys. Rev. Lett.* **82** (1999) 4180 [hep-ph/9905212].

[59] L. Covi, H.-B. Kim, J. E. Kim and L. Roszkowski, *Axinos as dark matter*, *JHEP* **05** (2001) 033 [hep-ph/0101009].

[60] E. J. Chun, *Dark matter in the Kim-Nilles mechanism*, *Phys. Rev.* **D84** (2011) 043509 [1104.2219].

[61] K. J. Bae, K. Choi and S. H. Im, *Effective Interactions of Axion Supermultiplet and Thermal Production of Axino Dark Matter*, *JHEP* **08** (2011) 065 [1106.2452].

[62] K.-Y. Choi, J. E. Kim and L. Roszkowski, *Review of axino dark matter*, *J. Korean Phys. Soc.* **63** (2013) 1685 [1307.3330].

[63] J. E. Kim, *Weak Interaction Singlet and Strong CP Invariance*, *Phys. Rev. Lett.* **43** (1979) 103.

[64] M. A. Shifman, A. I. Vainshtein and V. I. Zakharov, *Can Confinement Ensure Natural CP Invariance of Strong Interactions?*, *Nucl. Phys.* **B166** (1980) 493.

[65] M. Dine, W. Fischler and M. Srednicki, *A Simple Solution to the Strong CP Problem with a Harmless Axion*, *Phys. Lett.* **104B** (1981) 199.

[66] A. R. Zhitnitsky, *On Possible Suppression of the Axion Hadron Interactions. (In Russian)*, *Sov. J. Nucl. Phys.* **31** (1980) 260.

[67] LIGO Scientific, Virgo collaboration, B. P. Abbott et al., *Observation of Gravitational Waves from a Binary Black Hole Merger*, *Phys. Rev. Lett.* **116** (2016) 061102 [1602.03837].

[68] S. Bird, I. Cholis, J. B. Muñoz, Y. Ali-Haïmoud, M. Kamionkowski, E. D. Kovetz et al., *Did LIGO detect dark matter?*, *Phys. Rev. Lett.* **116** (2016) 201301 [1603.00464].

[69] B. J. Carr, K. Kohri, Y. Sendouda and J. Yokoyama, *New cosmological constraints on primordial black holes*, *Phys. Rev.* **D81** (2010) 104019 [0912.5297].

[70] V. Poulin, P. D. Serpico, F. Calore, S. Clesse and K. Kohri, *CMB bounds on disk-accreting massive primordial black holes*, *Phys. Rev.* **D96** (2017) 083524 [1707.04206].

[71] T. Nakama, B. Carr and J. Silk, *Limits on primordial black holes from μ distortions in cosmic microwave background*, *Phys. Rev.* **D97** (2018) 043525 [1710.06945].

[72] Y. Ali-Haïmoud and M. Kamionkowski, *Cosmic microwave background limits on accreting primordial black holes*, *Phys. Rev.* **D95** (2017) 043534 [1612.05644].

[73] T. D. Brandt, *Constraints on MACHO Dark Matter from Compact Stellar Systems in Ultra-Faint Dwarf Galaxies*, *Astrophys. J.* **824** (2016) L31 [1605.03665].

[74] S. M. Koushiappas and A. Loeb, *Dynamics of Dwarf Galaxies Disfavor Stellar-Mass Black Holes as Dark Matter*, *Phys. Rev. Lett.* **119** (2017) 041102 [1704.01668].

[75] DES collaboration, T. S. Li et al., *Farthest Neighbor: The Distant Milky Way Satellite Eridanus II*, *Astrophys. J.* **838** (2017) 8 [1611.05052].

[76] M. Zumalacarregui and U. Seljak, *Limits on stellar-mass compact objects as dark matter from gravitational lensing of type Ia supernovae*, *Phys. Rev. Lett.* **121** (2018) 141101 [1712.02240].

[77] J. Garcia-Bellido, S. Clesse and P. Fleury, *Primordial black holes survive SN lensing constraints*, *Phys. Dark Univ.* **20** (2018) 95 [1712.06574].

[78] T. Harada, C.-M. Yoo, K. Kohri and K.-I. Nakao, *Spins of primordial black holes formed in the matter-dominated phase of the Universe*, *Phys. Rev.* **D96** (2017) 083517 [1707.03595].

[79] F. D'Eramo, N. Fernandez and S. Profumo, *Dark Matter Freeze-in Production in Fast-Expanding Universes*, *JCAP* **1802** (2018) 046 [1712.07453].

[80] VIRGO, LIGO Scientific collaboration, B. P. Abbott et al., *GW170104: Observation of a 50-Solar-Mass Binary Black Hole Coalescence at Redshift 0.2*, *Phys. Rev. Lett.* **118** (2017) 221101 [1706.01812].

[81] Virgo, LIGO Scientific collaboration, B. P. Abbott et al., *GW170608: Observation of a 19-solar-mass Binary Black Hole Coalescence*, *Astrophys. J.* **851** (2017) L35 [1711.05578].

[82] Virgo, LIGO Scientific collaboration, B. P. Abbott et al., *GW170814: A Three-Detector Observation of Gravitational Waves from a Binary Black Hole Coalescence*, *Phys. Rev. Lett.* **119** (2017) 141101 [1709.09660].

[83] Virgo, LIGO Scientific collaboration, B. P. Abbott et al., *Binary Black Hole Mergers in the first Advanced LIGO Observing Run*, *Phys. Rev.* **X6** (2016) 041015 [1606.04856].

[84] W. M. Farr, S. Stevenson, M. Coleman Miller, I. Mandel, B. Farr and A. Vecchio, *Distinguishing Spin-Aligned and Isotropic Black Hole Populations With Gravitational Waves*, *Nature* **548** (2017) 426 [1706.01385].

[85] K. Belczynski et al., *The origin of low spin of black holes in LIGO/Virgo mergers*, 1706.07053.

[86] S. Vitale, D. Gerosa, C.-J. Haster, K. Chatziioannou and A. Zimmerman, *Impact of Bayesian Priors on the Characterization of Binary Black Hole Coalescences*, *Phys. Rev. Lett.* **119** (2017) 251103 [1707.04637].

[87] B. Farr, D. E. Holz and W. M. Farr, *Using Spin to Understand the Formation of LIGO and Virgo's Black Holes*, *Astrophys. J.* **854** (2018) L9 [1709.07896].

[88] S. Stevenson, C. P. L. Berry and I. Mandel, *Hierarchical analysis of gravitational-wave measurements of binary black hole spin–orbit misalignments*, *Mon. Not. Roy. Astron. Soc.* **471** (2017) 2801 [1703.06873].

[89] D. Wysocki, J. Lange and R. O. 'shaughnessy, *Reconstructing phenomenological distributions of compact binaries via gravitational wave observations*, 1805.06442.

[90] T. Chiba and S. Yokoyama, *Spin Distribution of Primordial Black Holes*, *PTEP* **2017** (2017) 083E01 [1704.06573].

[91] LIGO Scientific, VIRGO collaboration, J. Abadie et al., *Predictions for the Rates of Compact Binary Coalescences Observable by Ground-based Gravitational-wave Detectors*, *Class. Quant. Grav.* **27** (2010) 173001 [1003.2480].

[92] I. Mandel and R. O'Shaughnessy, *Compact Binary Coalescences in the Band of Ground-based Gravitational-Wave Detectors*, *Class. Quant. Grav.* **27** (2010) 114007 [0912.1074].

[93] M. Spera and M. Mapelli, *Very massive stars, pair-instability supernovae and intermediate-mass black holes with the SEVN code*, *Mon. Not. Roy. Astron. Soc.* **470** (2017) 4739 [1706.06109].

[94] C. Kimball, C. P. L. Berry and V. Kalogera, *What GW170729's exceptional mass and spin tells us about its family tree*, 1903.07813.

[95] M. U. Kruckow, T. M. Tauris, N. Langer, M. Kramer and R. G. Izzard, *Progenitors of gravitational wave mergers: Binary evolution with the stellar grid-based code ComBinE*, 1801.05433.

[96] M. Fishbach, D. E. Holz and B. Farr, *Are LIGO's Black Holes Made From Smaller Black Holes?*, *Astrophys. J.* **840** (2017) L24 [1703.06869].

[97] S. Vitale, *Three observational differences for binary black holes detections with second and third generation gravitational-wave detectors*, *Phys. Rev.* **D94** (2016) 121501 [1610.06914].

[98] A. Heger and S. E. Woosley, *The nucleosynthetic signature of population III*, *Astrophys. J.* **567** (2002) 532 [astro-ph/0107037].

[99] K. Belczynski et al., *The Effect of Pair-Instability Mass Loss on Black Hole Mergers*, *Astron. Astrophys.* **594** (2016) A97 [1607.03116].

[100] M. Fishbach and D. E. Holz, *Where Are LIGO's Big Black Holes?*, *Astrophys. J.* **851** (2017) L25 [1709.08584].

[101] C. Talbot and E. Thrane, *Determining the population properties of spinning black holes*, *Phys. Rev.* **D96** (2017) 023012 [1704.08370].

[102] J. Roulet and M. Zaldarriaga, *Constraints on Binary Black Hole Populations from LIGO-Virgo Detections*, *Mon. Not. Roy. Astron. Soc.* **484** (2019) 4216 [1806.10610].

[103] Y. Bai, V. Barger and S. Lu, *Measuring the Black Hole Mass Spectrum from Redshifts of aLIGO Binary Merger Events*, 1802.04909.

[104] J. E. McClintock, R. Narayan and J. F. Steiner, *Black Hole Spin via Continuum Fitting and the Role of Spin in Powering Transient Jets*, *Space Sci. Rev.* **183** (2014) 295 [1303.1583].

[105] L. Gou, J. E. McClintock, M. J. Reid, J. A. Orosz, J. F. Steiner, R. Narayan et al., *The Extreme Spin of the Black Hole in Cygnus X-1*, *Astrophys. J.* **742** (2011) 85 [1106.3690].

[106] E. Thrane and C. Talbot, *An introduction to Bayesian inference in gravitational-wave astronomy: parameter estimation, model selection, and hierarchical models*, *Publ. Astron. Soc. Austral.* **36** (2019) 10 [1809.02293].

[107] K. K. Y. Ng, S. Vitale, A. Zimmerman, K. Chatziioannou, D. Gerosa and C.-J. Haster, *Gravitational-wave astrophysics with effective-spin measurements: asymmetries and selection biases*, *Phys. Rev.* **D98** (2018) 083007 [1805.03046].

[108] M. Campanelli, C. O. Lousto and Y. Zlochower, *Spinning-black-hole binaries: The orbital hang up*, *Phys. Rev.* **D74** (2006) 041501 [gr-qc/0604012].

[109] S. Clesse and J. García-Bellido, *Seven Hints for Primordial Black Hole Dark Matter*, *Phys. Dark Univ.* **22** (2018) 137 [1711.10458].

[110] V. Tiwari, S. Fairhurst and M. Hannam, *Constraining black-hole spins with gravitational wave observations*, *Astrophys. J.* **868** (2018) 140 [1809.01401].

[111] A. V. Tutukov and L. R. YungelSon, *The merger rate of neutron star and black hole binaries*, *Mon. Not. Roy. Astron. Soc.* **260** (1993) 675.

[112] M. C. Miller and J. M. Miller, *The Masses and Spins of Neutron Stars and Stellar-Mass Black Holes*, *Phys. Rept.* **548** (2014) 1 [1408.4145].

[113] D. Gerosa, E. Berti, R. O'Shaughnessy, K. Belczynski, M. Kesden, D. Wysocki et al., *Spin orientations of merging black holes formed from the evolution of stellar binaries*, *Phys. Rev.* **D98** (2018) 084036 [1808.02491].

[114] T. Fragos, M. Tremmel, E. Rantsiou and K. Belczynski, *Black Hole Spin-Orbit Misalignment in Galactic X-ray Binaries*, *Astrophys. J.* **719** (2010) L79 [1001.1107].

[115] D. Wysocki, D. Gerosa, R. O'Shaughnessy, K. Belczynski, W. Gladysz, E. Berti et al., *Explaining LIGO's observations via isolated binary evolution with natal kicks*, *Phys. Rev.* **D97** (2018) 043014 [1709.01943].

[116] LIGO Scientific, Virgo collaboration, B. P. Abbott et al., *Astrophysical Implications of the Binary Black-Hole Merger GW150914*, *Astrophys. J.* **818** (2016) L22 [1602.03846].

[117] P. Marchant, N. Langer, P. Podsiadlowski, T. M. Tauris and T. J. Moriya, *A new route towards merging massive black holes*, *Astron. Astrophys.* **588** (2016) A50 [1601.03718].

[118] S. F. Portegies Zwart and S. McMillan, *Black hole mergers in the universe*, *Astrophys. J.* **528** (2000) L17 [astro-ph/9910061].

[119] C. L. Rodriguez, M. Morscher, B. Pattabiraman, S. Chatterjee, C.-J. Haster and F. A. Rasio, *Binary Black Hole Mergers from Globular Clusters: Implications for Advanced LIGO*, *Phys. Rev. Lett.* **115** (2015) 051101 [1505.00792].

[120] N. C. Stone, B. D. Metzger and Z. Haiman, *Assisted inspirals of stellar mass black holes embedded in AGN discs: solving the 'final au problem'*, *Mon. Not. Roy. Astron. Soc.* **464** (2017) 946 [1602.04226].

[121] S. Sigurdsson and L. Hernquist, *Primordial black holes in globular clusters*, *Nature* **364** (1993) 423.

[122] K. Postnov and N. Mitichkin, *Spins of primordial binary black holes before coalescence*, 1904.00570.

[123] B. Zackay, T. Venumadhav, L. Dai, J. Roulet and M. Zaldarriaga, *A Highly Spinning and Aligned Binary Black Hole Merger in the Advanced LIGO First Observing Run*, 1902.10331.

[124] T. Venumadhav, B. Zackay, J. Roulet, L. Dai and M. Zaldarriaga, *New Binary Black Hole Mergers in the Second Observing Run of Advanced LIGO and Advanced Virgo*, 1904.07214.

[125] D. Buttazzo, G. Degrassi, P. P. Giardino, G. F. Giudice, F. Sala, A. Salvio et al., *Investigating the near-criticality of the Higgs boson*, *JHEP* **12** (2013) 089 [1307.3536].

[126] L. J. Hall and Y. Nomura, *Grand Unification and Intermediate Scale Supersymmetry*, *JHEP* **02** (2014) 129 [1312.6695].

[127] L. J. Hall, Y. Nomura and S. Shirai, *Grand Unification, Axion, and Inflation in Intermediate Scale Supersymmetry*, *JHEP* **06** (2014) 137 [1403.8138].

[128] P. J. Fox, G. D. Kribs and A. Martin, *Split Dirac Supersymmetry: An Ultraviolet Completion of Higgsino Dark Matter*, *Phys. Rev.* **D90** (2014) 075006 [1405.3692].

[129] F. D'Eramo, L. J. Hall and D. Pappadopulo, *Radiative PQ Breaking and the Higgs Boson Mass*, *JHEP* **06** (2015) 117 [1502.06963].

[130] V. F. Mukhanov, *Nucleosynthesis without a computer*, *Int. J. Theor. Phys.* **43** (2004) 669 [astro-ph/0303073].

[131] E. W. Kolb and M. S. Turner, *The Early Universe*, *Front. Phys.* **69** (1990) 1.

[132] M. E. Peskin and D. V. Schroeder, *An Introduction to quantum field theory*. Addison-Wesley, Reading, USA, 1995.

[133] R. O'Shaughnessy, D. Gerosa and D. Wysocki, *Inferences about supernova physics from gravitational-wave measurements: GW151226 spin misalignment as an indicator of strong black-hole natal kicks*, *Phys. Rev. Lett.* **119** (2017) 011101 [1704.03879].

[134] K. Postnov and A. Kuranov, *Black hole spins in coalescing binary black holes*, *Mon. Not. Roy. Astron. Soc.* **483** (2019) 3288 [1706.00369].

[135] F. Elahi, C. Kolda and J. Unwin, *UltraViolet Freeze-in*, *JHEP* **03** (2015) 048 [1410.6157].

[136] R. R. Caldwell, *A Phantom menace?*, *Phys. Lett.* **B545** (2002) 23 [astro-ph/9908168].

[137] J. Sola and H. Stefancic, *Effective equation of state for dark energy: Mimicking quintessence and phantom energy through a variable lambda*, *Phys. Lett.* **B624** (2005) 147 [astro-ph/0505133].

[138] E. J. Copeland, M. Sami and S. Tsujikawa, *Dynamics of dark energy*, *Int. J. Mod. Phys.* **D15** (2006) 1753 [hep-th/0603057].

[139] Y.-F. Cai, E. N. Saridakis, M. R. Setare and J.-Q. Xia, *Quintom Cosmology: Theoretical implications and observations*, *Phys. Rept.* **493** (2010) 1 [0909.2776].

[140] L. P. Chimento, *Extended tachyon field, Chaplygin gas and solvable k-essence cosmologies*, *Phys. Rev.* **D69** (2004) 123517 [astro-ph/0311613].

[141] P. Creminelli, K. Hinterbichler, J. Khoury, A. Nicolis and E. Trincherini, *Subluminal Galilean Genesis*, *JHEP* **02** (2013) 006 [1209.3768].

[142] J.-L. Lehners, *New Ekpyrotic Quantum Cosmology*, *Phys. Lett.* **B750** (2015) 242 [1504.02467].

[143] T. Piran and K. Hotokezaka, *Who Ordered That? On The Origin of LIGO's Merging Binary Black Holes*, 1807.01336.

[144] D. Gerosa, A. Lima, E. Berti, U. Sperhake, M. Kesden and R. O'Shaughnessy, *Wide nutation: binary black-hole spins repeatedly oscillating from full alignment to full anti-alignment*, *Class. Quant. Grav.* **36** (2018) 10 [1811.05979].

[145] T. W. Baumgarte and C. Gundlach, *Critical collapse of rotating radiation fluids*, *Phys. Rev. Lett.* **116** (2016) 221103 [1603.04373].

[146] C. Gundlach and T. W. Baumgarte, *Critical gravitational collapse with angular momentum*, *Phys. Rev.* **D94** (2016) 084012 [1608.00491].

[147] C. Gundlach and J. M. Martin-Garcia, *Critical phenomena in gravitational collapse*, *Living Rev. Rel.* **10** (2007) 5 [0711.4620].

[148] K. Hotekezaka and T. Piran, *Are the observed black hole mergers spins consistent with field binary progenitors?*, 1707.08978.

[149] M. Sasaki, T. Suyama, T. Tanaka and S. Yokoyama, *Primordial Black Hole Scenario for the Gravitational-Wave Event GW150914*, *Phys. Rev. Lett.* **117** (2016) 061101 [1603.08338].

[150] L. Barack et al., *Black holes, gravitational waves and fundamental physics: a roadmap*, 1806.05195.

[151] M. Sasaki, T. Suyama, T. Tanaka and S. Yokoyama, *Primordial black holes—perspectives in gravitational wave astronomy*, *Class. Quant. Grav.* **35** (2018) 063001 [1801.05235].

[152] E. Payne, C. Talbot and E. Thrane, *Higher order gravitational-wave modes with likelihood reweighting*, 1905.05477.